FABRICATION OF ELECTROCHEMICAL SENSORS USING MANGANESE OXIDE NANOSTRUCTURE- AND COBALT OXIDE NANOSTRUCTURE-DECORATED YTTERBIUM NANORODS AS ELECTROCATALYSTS FOR THE DETECTION OF FLUTAMIDE, BICALUTAMIDE AND HYDROXYFLUTAMIDE IN SPIKED SAMPLES

---

by

THOMPHO RAVELE

Submitted in accordance with the requirements for the degree of

MASTER OF SCIENCE

in the subject

CHEMISTRY

at the

UNIVERSITY OF SOUTH AFRICA

SUPERVISOR : Dr KUTLOANO E. SEKHOSANA

CO-SUPERVISOR : Dr NOZIPHO N. GUMBI

: Dr NTUTHUKO W. HLONGWA

: PROF. THABO T.I. NKAMBULE

February 2023

DECLARATION

Name: Thompho Ravele

Student number: 11743751

Degree: Master of Science: Chemistry

Exact wording of the title of the dissertation as appearing on the electronic copy submitted for examination:

FABRICATION OF ELECTROCHEMICAL SENSORS USING MANGANESE OXIDE NANOSTRUCTURE- AND COBALT OXIDE NANOSTRUCTURE-DECORATED YTTERBIUM NANORODS AS ELECTROCATALYSTS FOR THE DETECTION OF FLUTAMIDE, BICALUTAMIDE AND HYDROXYFLUTAMIDE IN SPIKED SAMPLES

I declare that the above dissertation is my own work and that all the sources that I have used or quoted have been indicated and acknowledged by means of complete references.

I further declare that I submitted the dissertation to originality checking software and that it falls within the accepted requirements for originality.

I further declare that I have not previously submitted this work, or part of it, for examination at Unisa for another qualification or at any other higher education institution.

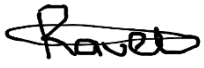

22-02-2023

_____ _____

SIGNATURE DATE

ACKNOWLEDGEMENTS

- First and foremost, I would like to thank God Almighty and the sweet fellowship of the Holy Spirit for making it possible for me to complete my studies.
- I wish to extend my deepest gratitude and sincere appreciation to my supervisor, Dr Edward Sekhosana, for your continued support. Your patience in teaching me most of the things I know now and directing the research work has made completing this work possible. I would also like to thank my co-supervisors, Dr Nozipho Gumbi, Dr Nthutuko Hlongwa, and Prof. Thabo Nkambule, for all the guidance and support.
- Many thanks to the iNanoWS students and staff members for contributing to our Thursday meetings. Special thanks to the technical team at iNanoWS. To the Applied Electrochemistry Thematic Area, I appreciate all the students and staff members for your various inputs through our AEC meetings, with special thanks to Prof. Feleni for being my pillar since I got here. Special thanks to my friends Fungai Chibaya, Mpho Khorae, Ginny Tito, and Simbongile Gumbi for making the lab work period experience more fun. I would also like to thank the council for Scientific and Industrial Research (CSIR) and iNanoWS for their financial support.
- I am sincerely grateful to the Love of My Life, Mr Collen Nepfumbada. Thank you so much for your continued support of my dreams, proofreading my work, being a shoulder to lean on, and being my pillar and number one supporter throughout this journey. To my son, Dakalo Nepfumbada, thank you so much for being patient and understanding that I needed to spend time away from you. I know it was not fair, baby, I love you.
- To my mother and best friend, Mrs Ravele, and my mother-in-law, Ms Khosa, thank you so much for all the prayers, blessings, love, friendship, and support. Special thanks to my siblings, Dakalo and Tshifhiwa Ravele; your love made me strong throughout my studies; I love you so much.
- Finally, I would like to express my profound gratitude to all members of the Woman After God's Heart (WAGH), with Special thanks to Pastor Lungile Divine Marhungane for all the love, support and prayers.

DEDICATION

This work is dedicated to my late father, Mr Amos Ravele and my mother, Mrs Marcia Ravele. They raised me with principles and implanted a sense of direction, dedication, discipline and focus on doing my work diligently and pursuing my passions. They both sacrificed a lot for me to be where I am today.

I also dedicate this work to my siblings,

Dakalo and Tshifhiwa Ravele.

These people believe in me so much; they make me want to always do better.

This work is also dedicated to my son,

Dakalo Nepfumbada

This boy is my inspiration, and he keeps me going every day.

And to the Love of My Life,

Mr Collen Nepfumbada

He has been my pillar of strength throughout this study

PUBLICATIONS

Thompho Ravele, Xolile G. Fuku, Ntuthuko W. Hlongwa, Thabo T.I. Nkambule, Nozipho N. Gumbi, Kutloano E. Sekhosana, Advances in Electrochemical Systems for Detection of Anti-Androgens in Water Bodies, **submitted to chemistrySelect Journal**.

Thompho Ravele, Ntuthuko W. Hlongwa, Thabo T.I. Nkambule, Nozipho N. Gumbi, Kutloano E. Sekhosana, Electrochemical sensors based on manganese and cobalt oxide nanostructures for the detection of flutamide and its derivatives in real water samples, **submitted to michrochemical Journal**.

PRESENTATIONS

Thompho Ravele, Ntuthuko W. Hlongwa, Thabo T.I. Nkambule, Nozipho N. Gumbi, Kutloano E. Sekhosana, Development of Ytterbium-based Nanorods and Nanowires Decorated with Nanoflowers as Efficient Electrocatalysts for Flutamide Derivatives in Water, Proposal defense preparations, AEC thematic area, 2021.

Thompho Ravele, Ntuthuko W. Hlongwa, Thabo T.I. Nkambule, Nozipho N. Gumbi, Kutloano E. Sekhosana, Development of Ytterbium-based Nanorods and Nanowires Decorated with Nanoflowers as Efficient Electrocatalysts for Flutamide Derivatives in Water, Proposal defense, panel of evaluators, 2021.

Thompho Ravele, Ntuthuko W. Hlongwa, Thabo T.I. Nkambule, Nozipho N. Gumbi, Kutloano E. Sekhosana, Development of Ytterbium-based Nanorods and Nanowires Decorated with Nanoflowers as Efficient Electrocatalysts for Flutamide Derivatives in Water, Proposal presentation, iNanoWS Thursday meeting, 2021.

Thompho Ravele, Ntuthuko W. Hlongwa, Thabo T.I. Nkambule, Nozipho N. Gumbi, Kutloano E. Sekhosana, Development of ytterbium-based nanorods decorated with manganese and cobalt oxide nanoflowers as electrocatalysts for the detection of flutamide and its derivatives, Progress report, AEC thematic area, 2021.

ABSTRACT

Anti-androgens (AAs) are a class of pharmaceutical drugs used to treat prostate cancer. Over the years, prostate cancer has been reported as the most frequent cancer diagnosis in men and the leading cause of mortality worldwide. However, recent studies show that deaths related to prostate cancer have reduced due to new cancer therapies, including AAs. Consequently, the number of patients using AAs is increasing exponentially. The unremitting use of these AAs may lead to regular excretion in the urine and faeces, thus entering wastewater treatment plants (WWTPs). Since some of these compounds are not entirely eliminated by wastewater treatment plant processes, trace levels remain in inadequately treated sewage effluents and are discharged into surface waters. The discharge might cause continued consumption by people who use surface water for survival, thus causing problems such as drug resistance.

Consequently, there is a need to develop methods to determine and control AAs in water. Several analytical methods have been employed. However, the employed methods suffer drawbacks such as high-cost, time consumption and tedious protocols. It is, therefore, of uttermost importance to develop alternative methods to monitor and quantify AAs in water bodies. The AAs of interest in this study are flutamide (FLU), bicalutamide (BIC) and hydroxyflutamide (OHF). In this work, I have developed five electrochemical sensors based on manganese oxide (MnO) and cobalt oxide (CoO) nanostructures (NSs); ytterbium nanorods (YbNRs); as well as YbNRs decorated with MnONSs and CoONSs (YbNRs/MnONSs and YbNRs/CoONSs) as electrocatalysts. This study was conducted in compliance with the University's Policy on Research Ethics and within the confines of the conditions stipulated in the acquired ethical clearance certificate. The electrocatalysts were synthesised using the hydrothermal and precipitation methods. The as-prepared materials were characterised using Scanning Electron Microscopy (SEM), Fourier Transform Infrared (FTIR) spectroscopy, Ultraviolet-Visible spectroscopy (UV-Vis), Transmission Electron microscopy (TEM), Energy-dispersive X-ray spectroscopy (EDX), and X-ray powder diffraction (XRD). The electrochemical techniques employed in this study are Cyclic Voltammetry (CV) and Square Wave Voltammetry (SWV). The electrochemical responses of the fabricated sensors were examined at a linear range from 32.01 –

50.00 µM. The limit of detections (LODs) and quantifications (LOQs) of the fabricated sensors were comparable to the literature. Both fabricated sensors showed good percentage recoveries. The fabricated electrochemical sensors showed good selectivity, stability, reliability, repeatability and reproducibility. Thus, it can be concluded that the fabricated sensors may represent a simple, low-cost and comfortable electrochemical tool for routine analysis in pharmaceutical and environmental monitoring of contaminants.

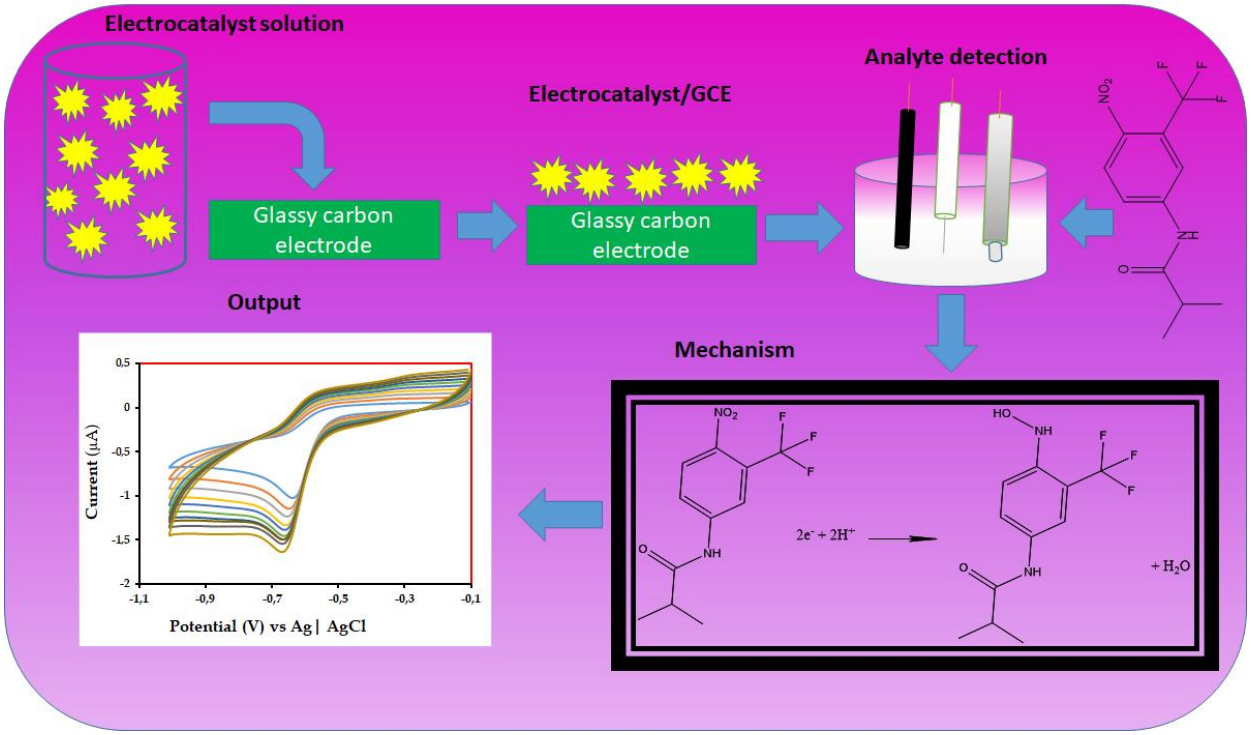

A: Graphical abstract

KEY TERMS: Anti-androgens, Electrochemical sensor, Metal oxide nanostructures, Manganese oxide, Cobalt oxide, Ytterbium nanorods, Nanocomposite, Electrocatalysts, Detection, Flutamide, Bicalutamide, Hydroxyflutamide, Glassy carbon electrode, Pharmaceuticals.

LIST OF ABBREVIATIONS

AAs	Anti-androgens
AEC	Applied electrochemistry
ATR	Attenuated total reflectance
BIC	Bicalutamide
CE	Counter electrode
CoO	Cobalt oxide
CoO/GCE	Cobalt oxide nanostructures/glassy carbon electrode
CoONP	Cobalt Oxide Nanoparticle
CoONSs	Cobalt oxide nanostructures
CSIR	Council for Scientific and Industrial Research
CV	Cyclic Voltammetry
DI	Deionized water
DMF	Dimethylformamide
EDS	Energy-Dispersive X-ray spectroscopy
EDX	Energy-dispersive X-ray spectroscopy
FLU	Flutamide
FTIR	Fourier Transform Infrared spectroscopy
GCE	Glassy carbon electrode
HPLC	High-performance liquid chromatography
HPTLC	High-performance thin-layer chromatography
JCPDS	Joint Committee on Powder Diffraction Standards
$K_3Fe_3(CN)_6$	Potassium ferricyanide(III)

$K_4Fe(CN)_6$	Potassium hexacyanoferrate(II)
KCl	Potassium chloride boixtra
LODs	Limit of detections
LOQs	Limit of quantifications
MnO	Manganese oxide
MnO/GCE	Manganese oxide nanostructures/glassy carbon electrode
MnONP	manganese oxide nanoparticle
MnONSs	Manganese oxide nanostructures
MnOOH	Manganese oxide-hydroxide
MO	Metal oxide
MONMs	Metal oxide nanomaterials
MONPs	Metal oxide nanoparticles
Na_2HPO_4	Sodium phosphate dibasic
NAAs	Non-steroidal anti-androgens
NaH_2PO_4	Sodium phosphate monobasic
NC	Nanocomposite
NMs	Nanomaterials
NPs	Nanoparticles
NRs	Nanorods
NSs	Nanostructures
OHF	Hydroxyflutamide
PBS	Phosphate buffer solution
PCs	Pharmaceuticals
RE	Reference electrode

RSD	Relative standard deviation
SD	standard Deviation
SEM	Scanning Electron Microscopy
STPs	Sewage treatment plants
SWV	Square Wave Voltammetry
TEM	Transmission Electron microscopy
UV-Vis	Ultraviolet-Visible spectroscopy
WE	Working electrode
WWTPs	Wastewater treatment plants
XRD	X-ray powder diffraction
YbNRs	Ytterbium nanorods
YbNRs/GCE	Ytterbium nanorods/glassy carbon electrode
YbNRs/CoONSs nanostructures	Ytterbium nanorods decorated with cobalt oxide
YbNRs/CoONSs/GCE	Ytterbium nanorods Ytterbium nanorods decorated with cobalt oxide nanostructures/glassy carbon electrode
YbNRs/MnONSs	Ytterbium nanorods decorated with manganese oxide nanostructures
YbNRs/MnONSs/GCE	Ytterbium nanorods decorated with manganese oxide nanostructures/glassy carbon electrode
ZnO	Zinc Oxide
ZnONS	Zinc oxide nanostructure

LIST OF SYMBOLS

μM	Micromolar
E_{pa}	Anodic peak potential
E_{pc}	Cathodic peak potential
I_{pa}	Anodic peak current
Γ	Surface roughness factors
ΔE_p	Peak-to-peak separation

TABLE OF CONTENTS

LIST OF FIGURES

LIST OF TABLES

CHAPTER 1

INTRODUCTION

1.1 Background

Water contamination by pharmaceuticals (PCs) is a significant concern that has attracted a large amount of attention from researchers globally [1,2]. PCs have, as a consequence, been characterised as emerging contaminants, now defined as new chemicals without regulatory status whose effect on the environment and human health is inadequately understood [3,4]. PCs are characterised as emerging pollutants because they cause severe health effects on humans, cause deterioration of water quality and threaten terrestrial life [5]. Despite their adverse side effects, PCs have immense benefits to humanity, including healthier and longer lives. Consequently, they are continuously prescribed in increasing amounts daily. This is another reason they are considered environmental contaminants of emerging concern [6].

As a result of the daily and continuous prescription of PCs, portions of PCs are excreted into sewage treatment plants (STPs) and wastewater treatment plants (WWTPs) by their intended consumers either as metabolites, unmetabolized or as conjugates that may be reactivated [7]. As it has been scientifically proven that some, if not all WWTPs are unable to completely degrade PCs during treatment, these compounds end up in surface water [8,9].

Other factors, such as lack of sewage treatment in rural areas, contribute to water contamination by PCs. For example, the direct disposal of human waste into the ground and surface water also contributes to water contamination. Another factor contributing to water contamination is the direct discharge of untreated wastewater to the environment caused by the leakages of septic tanks, landfill leachates, animal waste and treatment drugs, and the application of manure or WWTP sludge as fertilizer in agricultural fields[8,10].

Environmental pollution, which includes water and soil pollution, is among the significant causes of the increase in the incidence of human cancers worldwide. Even though cancer is the world's biggest problem, with an estimated 29.5 million new cancer cases anticipated by 2040 globally[11], there is still significantly less attention paid to cytostatic drugs. The anticipated number might be due to common factors

increasing cancer. The factors include unhealthy lifestyles, tobacco and alcohol consumption, nutritional habits and increasing longevity in humans[12,13]. Among the different types of cancer, prostate cancer is said to be the second most common cancer worldwide and the fifth principal cause of death in men[14]. The unceasing incidence of prostate cancer results in the continuous consumption of AAs. AAs are a class of cytostatic drugs used therapeutically in treating prostate cancer patients [15]. Antiandrogen drugs approved by the Food and Drug Administration (FDA) include BIC, enzalutamide, and FLU[16].

Flutamide (FLU) and bicalutamide (BIC) work by blocking testosterone (a male hormone that stimulates the growth of prostate cancer cells) from mediating its biological effects in the body. They do so by competing with testosterone for binding to androgen receptors in the prostate gland, thereby decreasing the growth of the tumour[17]. Hydroxyflutamide (OHF), an active metabolite of FLU, also works by competing with testosterone to bind to androgen receptors and results in the impairment of testosterone signalling[18]. Although AAs cannot cure prostate cancer, they can extend the lifetime of patients for many months or years [19]. However, the efficacy of these AAs seems to be overshadowed by their adverse side effects.

These side effects, resulting from continuous consumption of FLU and OHF, include inflamed prostate, blood in urine, rectal bleeding, hot flashes, loss of sexual interest/ability, diarrhoea, nausea, and vomiting, enlarged growth of male breasts, drowsiness, liver malfunction and methemoglobinemia[20,21]. The most frequent side effect of BIC is acute kidney injury[22]. Consequently, there is a need for new, advanced and perspective analytical methods with high sensitivity and selectivity for the continual control of antiandrogen drugs in water samples.

To date, several methods have been reported in the literature, including spectrophotometry[23,24], high-performance liquid chromatography[25,26], mass spectrometry [27], liquid chromatography[28], spectrofluorometry[29], photochemistry[30] and electrochemistry[31]. Most of these methods are sensitive, offer good selectivity and have the possibility for the simultaneous determination of several drugs. However, these methods have limitations such as the high price of the equipment, complicated sample preparation, laboratory based and not portable, requires skilled analyst to handle, use of toxic precursors or materials, and are tedious and time-consuming [32–

[34]. Electrochemistry is the most reliable method among the aforementioned methods because of its speed, high sensitivity, good precision, good selectivity, and uncomplicated instruments [35,36].

As a result, this study explored electrochemical means by developing separate electrochemical sensors based on ytterbium nanorods (YbNRs), manganese oxide nanostructures (MnONSs) and cobalt oxide nanostructures CoONSs and YbNRs decorated with metal (manganese and cobalt) oxide nanostructures MONSs as electrocatalysts. These electrochemical sensors were used to determine FLU and its derivatives in water for control of associated side effects. To our knowledge, YbNRs decorated with MONSs have not been used to monitor FLU, BIC or OHF in water electrochemically. Thus, such nanohybrids will be used in this study for the first time.

1.2 Anti-androgens as water contaminants

PCs, including AAs, are among the primary contaminants of water, with up to 90% of oral drugs ingested by humans ending up in water systems. These compounds, therefore, pose a global water quality challenge and may cause severe effects on human health and ecosystems[37]. Although AAs are associated with acute side effects such as pulmonary, renal, hair follicle, oral and bone marrow toxicity [38], there is still little research for the determination and quantification of AAs carried out in African countries. Consequently, there is a strong need to monitor and control the occurrence of AAs in African water bodies. Although electrochemistry has been widely explored for the detection of AAs, there are limitations associated with some of the materials that have been used as electrocatalysts. Some limitations include low sensitivity, high-cost of precursor, and complicated synthesis[39]. As a result, electrocatalysts still need to be explored to detect AAs.

1.3 Materials used in the study and their advantages

Several studies highlight that the continuous consumption of FLU, BIC and OHF may result in severe side effects on human health. Therefore, the increasing cancer incidence and continuous use of these AAs are cause for concern. Although electrochemistry is considered the most reliable method among all the analytical methods employed to detect AAs, some drawbacks are associated with the materials used. The drawbacks include expensive precursor, complicated synthesis methods, the toxicity of precursors, and the use of toxic electrodes (e.g. dropping mercury

electrode) [40]. Subsequently, there is still a need for materials with fewer to no drawbacks to be employed as electrocatalysts.

This study does not focus on toxicity experiments but on simple, one-step preparation of YbNRs, MnONSs and CoONSs, as well as the development of sensing platforms. Ytterbium has advantages such as good thermal and electrical conductivity, which are advantageous over transition metals for stable electrochemical sensors, and excellent electrical, mechanical, and chemical stability[41,42]. Hence the fabrication of ytterbium-based NRs and the corresponding electrochemical sensors.

Manganese and cobalt oxide nanomaterials have advantages such as low-cost, environmental benignity, excellent conductivity, chemical stability, high specific surface area, good electrocatalytic activity, good stability, and excellent catalytic and selective ability[43,44]. As a result, MnONSs and CoONSs were employed in the study to decorate NRs to enhance their electrocatalytic activity for determining FLU and its derivatives in water samples.

1.3.1 Novelty of the study

To the best of my knowledge:

(i) Ytterbium-based NRs on their own have not been used in electrochemical sensing to detect FLU or its derivatives.

(ii) MnONSs and CoONSs have not been used in electrochemical sensors to detect FLU and its derivatives.

(iii) Nanostructure-decorated ytterbium-based electrochemical sensors for monitoring FLU and its derivatives are developed for the first time in this study.

1.4 Aim and objectives

1.4.1 Aim

This study aims to develop simple, electrocatalytically active, highly stable and reusable ytterbium-based NRs decorated with MnONSs and CoONSs to detect and quantify FLU, BIC and OHF in water samples.

1.4.2 Objectives

To achieve the aim of the study, the following objectives were pursued:

- To synthesise new ytterbium-based NRs.

- To synthesise MnONSs and CoONSs.
- To coat ytterbium-based NRs with MnONSs and CoONSs to form efficient electrocatalysts.
- To perform extensive characterisation of the synthesised nanomaterials as electrocatalysts.
- To apply the synthesised electrocatalysts as sensors in aqueous media to determine the amounts of FLU, BIC and OHF.

1.5 Key research questions

While looking at the quality control of FLU and its derivatives, as broadly alluded to in sections 1.1 and 1.2, the study sought to answer the following research questions:

- If proved viable for identifying and quantifying FLU in water, will the fabricated NRs be reusable as electrocatalysts in sensor systems?
- How does the efficiency of NRs in electrocatalysis compare to that of other electrocatalysts?
- How do MONSs manipulate and influence the chemical and electrochemical properties of NRs for enhanced electrochemical detection of FLU, BIC and OHF?

1.6 Thesis outline

A summary of each chapter discussed in this dissertation is as follows:

Chapter 1 introduces the purpose of the study by stressing the problems associated with pharmaceutical, in particular antiandrogens in water. The problem, justifications, aims, objectives, novelty, and research questions are also discussed.

Chapter 2 gives a comprehensive literature review on the mechanistic pathways of antiandrogens in water and the effects of antiandrogens on human health and aquatic ecosystem. The methods previously employed to detect antiandrogens and their drawbacks are also discussed, with electrochemistry being a reliable method. Furthermore, the electrocatalyts that have been used as electrocatalyts in the electrochemical detection of antiandrogens have been explored with their disadvantages. Metal oxide and rare-earth nanostructures as advantageous electrocatalyts have also been disussed together with their synthesis methods. Lastly, flutamide, bicalutamide and hydroxyflutamide as antiandrogens of choice have also been discussed.

Chapter 3 focuses on the methodologies that were used in the study. The materials, equations and equipments used in the study are detailed. Methods used in the preparation, decoration and characterization of the as-prepared materials are provided in detail. In addition to this, preparation of solution and detection procedures are outlined in detail.

Chapter 4 presents the data obtained on the characterisation of as-prepared materials using Scanning Electron Microscopy (SEM), Fourier Transform Infrared (FTIR) spectroscopy, Ultraviolet-Visible spectroscopy (UV-Vis), Transmission Electron microscopy (TEM), Energy-dispersive X-ray spectroscopy (EDX), and X-ray powder diffraction (XRD).

Chapter 5 reports on results on the electrochemical detection of flutamide, bicalutamide and hydroxyflutamide.

Chapter 6 outlines a comprehensive conclusion of the results produced in the study. The implications of the results are discussed and recommendations for future studies are put forward.

References

1. Azuma, T. Distribution of anti-cancer drugs in River Waters and Sediments of the Yodo River Basin, Japan. *Appl. Sci.* **8**, (2018).

2. Azuma, T., Arima, N., Tsukada, A., Hirami, S., Matsuoka, R., Moriwake, R., Ishiuchi, H., Inoyama, T., Teranishi, Y., Yamaoka, M. and Mino, Y. Detection of PCs and phytochemicals together with their metabolites in hospital effluents in Japan, and their contribution to sewage treatment plant influents. *Sci. Total Environ.* **548**–**549**, 189–197 (2016).

3. Rabii, F. W., Segura, P. A., Fayad, P. B. and Sauvé, S. Determination of six chemotherapeutic agents in municipal wastewater using online solid-phase extraction coupled to liquid chromatography-tandem mass spectrometry. *Sci. Total Environ.* **487**, 792–800 (2014).

4. Mendoza, A., Zonja, B., Mastroianni, N., Negreira, N., De Alda, M.L., Pérez, S., Barceló, D., Gil, A. and Valcárcel, Y. Drugs of abuse, cytostatic drugs and iodinated contrast media in tap water from the Madrid region (central Spain): A case study to analyse their occurrence and human health risk characterisation. *Environ. Int.* **86**, 107–118 (2016).

5. Ashfaq, M., Li, Y., Wang, Y., Chen, W., Wang, H., Chen, X., Wu, W., Huang, Z., Yu, C.P. and Sun, Q. Occurrence, fate, and mass balance of different classes of PCs and personal care products in an anaerobic-anoxic-oxic wastewater treatment plant in Xiamen, China. *Water Res.* **123**, 655–667 (2017).

6. Khan, A.H., Aziz, H.A., Khan, N.A., Hasan, M.A., Ahmed, S., Farooqi, I.H., Dhingra, A., Vambol, V., Changani, F., Yousefi, M. and Islam, S. Impact, disease outbreak and the eco-hazards associated with pharmaceutical residues: a Critical review. *Int. J. Environ. Sci. Technol.* **19**, 677– 688 (2022).

7. Rowney, N. C., Johnson, A. C. and Williams, R. J. Erratum: Cytotoxic drugs in drinking water: A prediction and risk assessment exercise for the Thames catchment in the United Kingdom. *Environ. Toxicol. Chem.* **30**, 1729–1729 (2011).

8. Vumazonke, S., Khamanga, S. M. and Ngqwala, N. P. Detection of Pharmaceutical Residues in Surface Waters of the Eastern Cape Province. **17**, 4067 (2020).

9. Balakrishna, K., Rath, A., Praveenkumarreddy, Y., Guruge, K. S. and Subedi, B. A review of the occurrence of PCs and personal care products in Indian water bodies. *Ecotoxicol. Environ. Saf.* **137**, 113–120 (2017).

10. 10. Madikizela, L. M., Tavengwa, N. T. and Chimuka, L. Status of PCs in African water bodies: Occurrence, removal and analytical methods. *J. Environ. Manage.* **193**, 211–220 (2017).

11. Li, D., Chen, H., Liu, H., Schlenk, D., Mu, J., Lacorte, S., Ying, G.G. and Xie, L. Anti-cancer drugs in the aquatic ecosystem: Environmental occurrence, ecotoxicological effect and risk assessment. *Environ. Int.* **153**, 106543 (2021).

12. Parrella, A., Lavorgna, M., Criscuolo, E., Russo, C. and Isidori, M. Estrogenic activity and cytotoxicity of six anti-cancer drugs detected in water systems. *Sci. Total Environ.* **485**–**486**, 216–222 (2014).

13. Jureczko, M. and Kalka, J. Cytostatic PCs as water contaminants Cytostatic PCs as water contaminants. *Eur. J. Pharmacol.* **866**, 172816 (2019).

14. Saka, C. Chromatographic Methods for Determination of Drugs Used in Prostate Cancer in Biological and Pharmacological Samples Chromatographic Methods for Determination of Drugs Used in Prostate Cancer in Biological and Phar. *Crit. Rev. Anal. Chem.* **49**, 78–99 (2019).

15. Ibrahim, H. and Temerk, Y. A novel disposable electrochemical sensor based on modifying graphite pencil lead electrode surface with nanoacetylene black for simultaneous determination of anti-androgens flutamide and cyproterone acetate. *J. Electroanal. Chem.* **859**, 113836 (2020).

16. Saka, C. Electroanalytical Approaches for Determination of Prostate Cancer Drugs in Biological Samples and Dosage Forms. *Crit. Rev. Anal. Chem.* **49**, 403–414 (2019).

17. Ahmadi, F., Raoof, J.B., Ojani, R., Baghayeri, M., Lakouraj, M.M. and Tashakkorian, H. Synthesis of Ag nanoparticles for the electrochemical detection of anti-cancer drug flutamide. *Cuihua Xuebao/Chinese J. Catal.* **36**, 439–445 (2015).

18. Farias, J.S., Zanin, H., Caldas, A.S., Dos Santos, C.C., Damos, F.S. and de Cássia Silva Luz, R. Functionalized Multi-walled Carbon Nanotube Electrochemical Sensor

for Determination of Anti-cancer Drug Flutamide. **46**, 5619–5628 (2017).

19. Manjula, N., Vinothkumar, V. and Chen, S. M. Synthesis and characterisation of iron-cobalt oxide/polypyrrole nanocomposite: An electrochemical sensing platform of anti-prostate cancer drug flutamide in human urine and serum samples. *Colloids Surfaces A Physicochem. Eng. Asp.* **628**, 127367 (2021).

20. Urbanová, V., Bakandritsos, A., Jakubec, P., Szambó, T. and Zbořil, R. A facile graphene oxide-based sensor for electrochemical detection of neonicotinoids. *Biosens. Bioelectron.* **89**, 532–537 (2017).

21. Kesavan, G. and Chen, S. Diamond and Related Materials Sonochemically exfoliated graphitic-carbon nitride for the electrochemical detection of flutamide in environmental samples. *Diam. Relat. Mater.* **108**, 107975 (2020).

22. Kogularasu, S., Akilarasan, M., Chen, S. M. and Sheu, J. K. Scalable and sustainable synthetic assessment between solid-state metathesis and sonochemically derived electrocatalysts (strontium molybdate) for the precise anti-androgen bicalutamide (CasodexTM) detection. *Microchem. J.* **168**, 106465 (2021).

23. Farid, N. F. and Abdelwahab, N. S. Two different spectrophotometric determinations of potential anti-cancer drug and its toxic metabolite. *Spectrochim. Acta - Part A Mol. Biomol. Spectrosc.* **145**, 360–367 (2015).

24. Deepakumari, H. N. and Revanasiddappa, H. D. Spectrophotometric Estimation of Flutamide in Pure and in Pharmaceutical Preparations. *ISRN Spectrosc.* **2012**, 1–7 (2012).

25. Matějíček, D. and Kubáň, V. High-performance liquid chromatography/ion-trap mass spectrometry for separation and simultaneous determination of ethynylestradiol, gestodene, levonorgestrel, cyproterone acetate and desogestrel. *Anal. Chim. Acta* **588**, 304–315 (2007).

26. de Hassonville, S.H., Chiap, P., Liégeois, J.F., Evrard, B., Delattre, L., Crommen, J., Piel, G. and Hubert, P. Development and validation of a high- performance liquid chromatographic method for the determination of cyproterone acetate in human skin. *J. Pharm. Biomed. Anal.* **36**, 133–143 (2004).

27. Khan, N., Abdelhamid, H. N., Yan, J. Y., Chung, F. T. and Wu, H. F. Detection of

flutamide in pharmaceutical dosage using higher electrospray ionization mass spectrometry (ESI-MS) tandem mass coupled with Soxhlet apparatus. *Anal. Chem. Res.* **3**, 89–97 (2015).

28. Christiaens, B., Chiap, P., Rbeida, O., Cello, D., Crommen, J. and Hubert, P. Fully automated method for the liquid chromatographic determination of cyproterone acetate in plasma using restricted access material for sample pre-treatment. *J. Chromatogr. B Anal. Technol. Biomed. Life Sci.* **795**, 73–82 (2003).

29. Ray, S., Ghosh (Ray), S. and Mandal, S. Development of bicalutamide-loaded PLGA nanoparticles: preparation, characterisation and in-vitro evaluation for the treatment of prostate cancer. *Artif. Cells, Nanomedicine Biotechnol.* **45**, 944– 954 (2017).

30. Sortino, S., Giuffrida, S., De Guidi, G., Chillemi, R., Petralia, S., Marconi, G., Condorelli, G. and Sciuto, S. The Photochemistry of Flutamide and its Inclusion Complex with β-Cyclodextrin. Dramatic Effect of the Microenvironment on the Nature and on the Efficiency of the Photodegradation Pathways¶. *Photochem. Photobiol.* **73**, 6 (2001).

31. Umesh, N.M., Jesila, J.A., Wang, S.F., Govindasamy, M., Alshgari, R.A., Ouladsmane, M. and Asharani, I.V. Fabrication of highly sensitive anti-cancer drug sensor based on heterostructured ZnO-Co_3O_4 capped on carbon nitride nanomaterials. *Microchem. J.* **167**, 106244 (2021).

32. Bonfilio, R., de Araújo, M. B. and Salgado, H. R. N. Recent applications of analytical techniques for quantitative pharmaceutical analysis: A review. *WSEAS Trans. Biol. Biomed.* **7**, 316–338 (2010).

33. Balcerzak, W. and Rezka, P. Occurrence of Anti-Cancer Drugs in the Aquatic Environment and Efficiency of Their Removal – the Selected Issues Występowanie Leków Przeciwnowotworowych W Środowisku Wodnym Oraz Skutechność Ich Usuwania – Wybrane Zagadnienia. 1–8 (2014).

34. Govindasamy, M., Mani, V., Chen, S.M., Maiyalagan, T., Selvaraj, S., Chen, T.W., Lee, S.Y. and Chang, W.H. Highly sensitive determination of non-steroidal anti-inflammatory drug nimesulide using electrochemically reduced graphene oxide nanoribbons. *RSC Adv.* **7**, 33043–33051 (2017).

35. Halali, V.V., Sanjayan, C.G., Suvina, V., Sakar, M. and Balakrishna, R.G. Perovskite

nanomaterials as optical and electrochemical sensors. *Inorg. Chem. Front.* **7**, 2702–2725 (2020).

CHAPTER 2

LITERATURE REVIEW

2.1 Introduction

The presence of anti-androgens (AAs) in the aquatic environment has stimulated much interest due to their potential adverse effects on human health and the aquatic ecosystem. Although the amounts detected in water systems are too low to cause an immediate threat, AA residues can potentially cause long-term effects on aquatic organisms if they interfere with DNA[1]. AAs may also cause severe effects on humans upon continuous consumption. Despite the wide use of AAs, very few studies have been conducted to investigate these compounds' behaviour, fate and effects in African water bodies, including South Africa. Herein, I discuss the pathways of AAs in water and their effects on human health and the aquatic ecosystem.

2.2 Mechanistic pathways of anti-androgens in water

Prostate cancer, acne, seborrhoea, hirsutism, and androgenic alopecia are all treated by AAs[2]. These illnesses are common and may result in the continuous consumption of AAs. After human administration, AAs are excreted mainly in urine and in low amounts in faeces (4.2%) as unchanged drugs and hydroxylated metabolites[3]. After excretion, these compounds end up in sewage and septic systems due to household use. Consequently, AAs are detected in wastewater treatment plants (WWTPs). Due to incomplete degradation during treatment, AAs may be released into the aquatic environment. AAs can also come into the environment through sewage leakages, pharmaceutical industry leakages and effluents or the disposal of unused or unfinished medication [4,5]. **Fig. 2.1** shows the AA mechanistic pathways into the aquatic environment cycle.

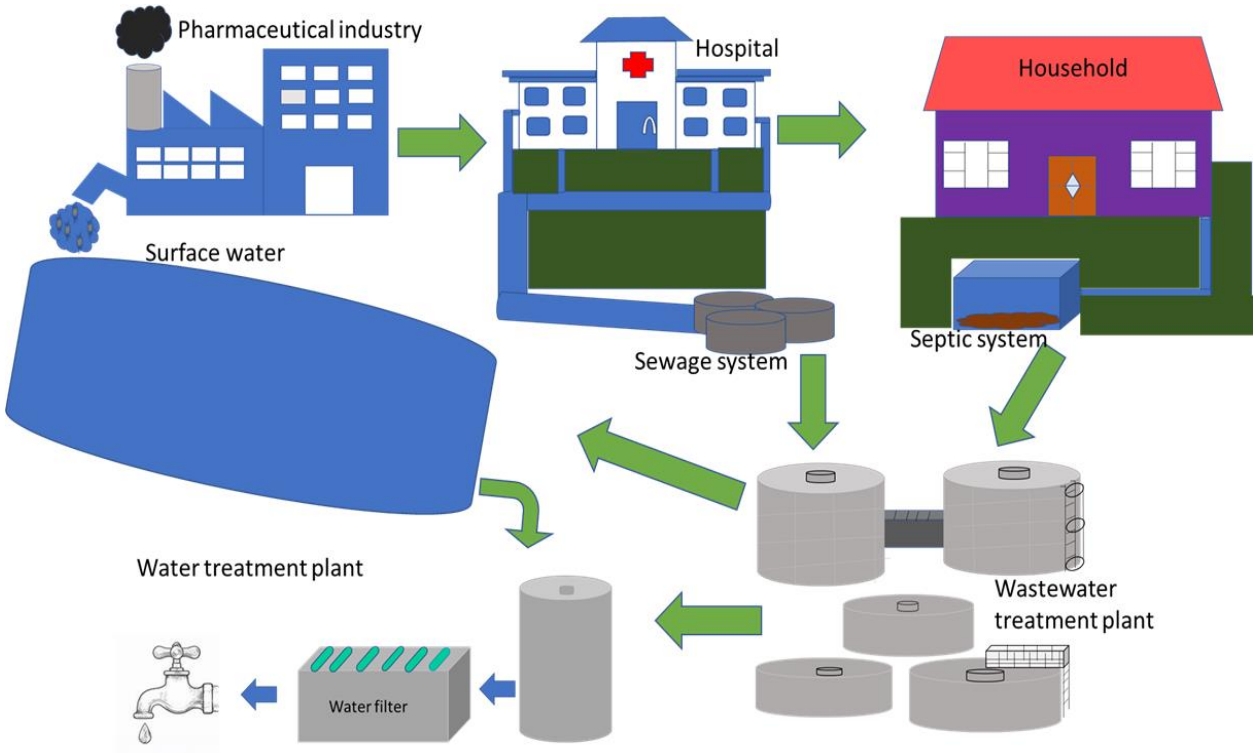

Fig. 2.1: Mechanistic pathways of anti-androgens into the aquatic environment.

2.3 Human health risks associated with the presence of anti-androgens in water

AAs are highly effective in treating cancer and other hyperandrogenism conditions and, thus, are crucial for saving lives. However, their efficacy is overshadowed by their many adverse side effects, such as alopecia, anaemia, nausea and vomiting. Moreover, their efficacy is also eclipsed by the fact that they are not cancer-specific and can be harmful to other rapidly dividing cells, such as hair and mucous membranes or bone marrow. AAs are more dangerous to foetuses than adults. The latter is because almost, if not all, cells of foetuses grow faster, and there are only a few rapidly growing cells in adults. As a result, unborn babies and children are the most affected individuals by these compounds[6].

Despite being micropollutants, AAs are naturally toxic. Their poor environmental biodegradability generally classifies them as a consequence of them not being completely degraded by conventional WWTPs [7]. Humans not diagnosed with cancer can be exposed to AAs via drinking water, consumption of aquatic organisms and food pyramid (after the soil has been exposed to AAs). This leads to human exposure to these AAs being a subject of concern, especially in countries such as South Africa and other African countries that still

use surface water as their primary source of drinking water [8]. Some of the significant toxicities associated with AAs on human health are discussed in **Table 2.1.**

Table 2.1. Major toxicities associated with anti-androgens on human health and their effects and symptoms.

Major toxicities of anti-androgens on human	**Symptoms and effects**	**Reference**
Pulmonary toxicity: used to describe side effects on the lungs	Acute lung injury	9
	Pulmonary hypertension	10
	Alveolar haemorrhage	11
	Bronchospasm	12
	Capillary leak syndrome	13
	Eosinophilic pneumonia	14
Renal toxicity: used to describe side effects on the kidney	Acute renal failure	15
	Chronic renal failure	16
	Glomerulone phritis	17
	Tubulopathies	18
Hair follicle toxicity: used to describe the effect on hair	Alopecia	19
	Pigmentary hair changes	20
	Textual hair changes	21
	Eyelash hair changes	22
Oral toxicity: used to describe the oral complication	Mucositis	23
	Saliva changes	24
	Taste alterations	25
	Infection and bleeding	26
	Mucosal atrophy	27
	Xerostomia	28
Bone marrow depression: used to describe effects on blood cell count	Blood in urine	29
	Diarrhoea	30
	Bleeding	31
	Pale Skin	32

	Easy tiring with exertion	[33]
	Mouth sores	[34]
	Easy bruising	[35]

2.4 Effects of anti-androgens in water on the aquatic ecosystem

The continuous release of pharmaceuticals PCs) into aquatic environments has led to the assessment of the environmental risks caused by these PCs and their metabolites being a major focus recently. Because South Africa is categorized as a water-scarce country, it is even more critical to assess the risks as there are few water resources. Although it is reported that PCs are present in relatively low concentrations in the aquatic environment, their wide use, high reactivity with biological systems, incessant release and relatively low degradation make them pseudo-persistent in aquatic environments [36,37].

In terms of numbers, prostate cancer is the sixth most common cancer worldwide. Its occurrence is increasing steadily in almost all countries. Since AAs play a vital role in developing a healthy prostate and treating prostate cancer, this implies that even the number of AA consumption is steadily increasing [38]. Consequently, even the rate of discharge of these AAs in aquatic ecosystems is increasing.

The frequent use and eventual discharge of AAs lead to their presence in pharmaceutical factory wastewater, hospital wastewater, domestic wastewater, and surface waters. Some of these AAs and their metabolites from wastewater end up in the aquatic ecosystem. Li *et al.* [39] detected 58% of these AAs in hospital wastewater, 52% in wastewater treatment plant effluents (78% in influents) and 59% in surface water. The occurrence of AAs in aquatic ecosystems results in unpleasant effects on aquatic organisms. They affect the reproductive function of Murray rainbowfish, medaka, guppies, and stickleback. The presence of anti-androgens in aquatic ecosystems also affects numerous processes and traits in these different fish species, as shown in **Table 2.2**.

Table 2.2. Effects of anti-androgens in water on various species of fish

Fish type	Antiandrogen affecting fish	Effects done by androgens on fish	Reference

Murray rainbowfish	-FLU	-Affect spermatogenesis in males - Affect oogenesis in females - Causes intersex -Impair the reproductive endocrine system	39–41
Male medaka	-Cyproterone acetate -FLU	-Affect gonadal development -Causes testicular fibroids -Affect spermatogenesis	39,42,43
Guppies	-FLU	-Impair normal development of male guppy's sexual phenotype -Disrupt the development of secondary sex characters -Affect spermatogenesis -Causes demasculinization	39,44,45
Male stickleback	-FLU -Cyproterone acetate	-Affects nest building -Affects courtship behaviour -Affects displacement fanning	39,46

In light of the above sections (2.1 – 2.4), the presence, persistence and toxicity of FLU and other AAs in the aquatic environment is an important subject that requires extensive investigation to help prevent the effects of these AAs on the environment and human health. The high burden of a high cancer diagnosis challenges the world. This points to a high use of anti-androgenic drugs, which results in relatively high concentrations of these AAs being released into aquatic environments. Consequently, there is a requirement to quantify and determine the fate of these AAs. There is also a need to extrapolate the possible long-term effects of these AAs on the environment and public health. There are only a few studies piloted on anti-androgenic drugs in water and their biodegradation profile. Due to the world having a lot of cancer diagnoses and more people surviving with treatment, it is anticipated that the concentration of anti-androgenic drugs will be significantly high in wastewater and surface water. This can be resolved by inclusive quantitative AA risk assessments that are unique. These analyses will assist in analysing different aspects of AA exposure to the environment and humans (the toxicity and associated health risks).

Removal of PCs such as AAs by WWTPs significantly reduces disposal to the aquatic environment. However, the treatment processes available in South Africa currently cannot completely remove PCs. This is because they are not designed to treat PCs. Consequently, this results in the discharge of these PCs into water bodies. The latter results in the need for constant monitoring of the concentrations of AAs as water contaminants. The continual monitoring will be essential in protecting public health, aquatic biodiversity and the quality of river water, wastewater and drinking water. However, as discussed in this thesis, a simple, selective, low-cost and rapid method is needed to develop a simple, selective, and rapid method for detecting these AAs in water. Structures of some non-steroidal anti-androgens (NAAs) are depicted in **Fig. 2.2**. FLU and BIC were chosen in this study because they are the most prescribed for cancer patients in South Africa, hence they may be present in water bodies. OHF was chosen because it is an active metabolite of FLU that is mostly excreted after consumption of FLU, hence it might also be available in water bodies.

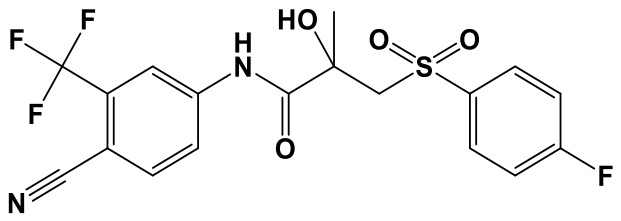

Bicalutamide

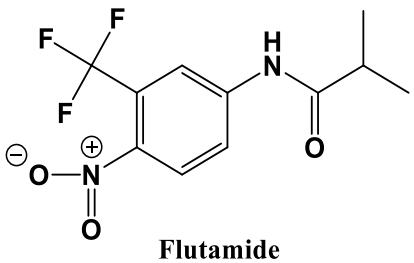

Flutamide

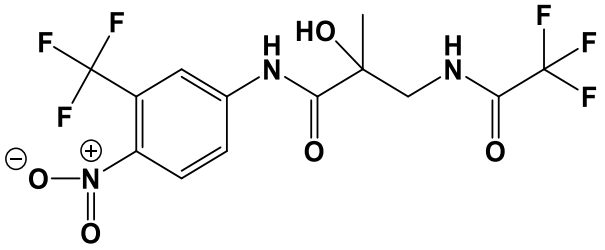

Topilutamide

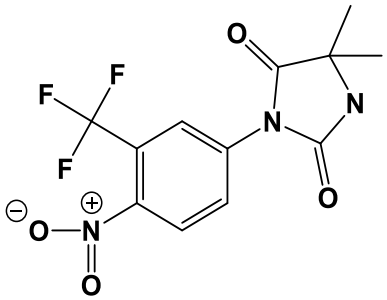

Nilutamide

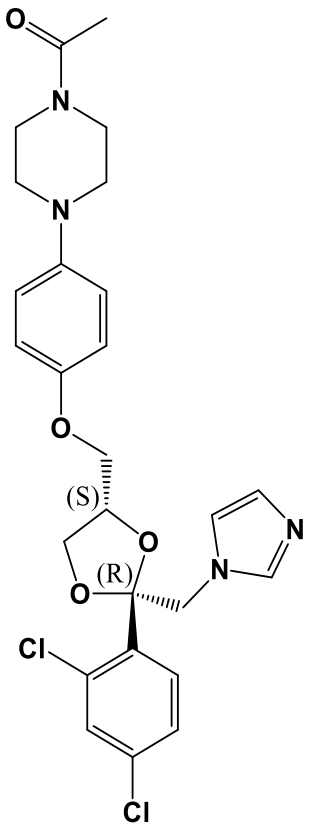

(2R,4S)-(+)-ketoconazole

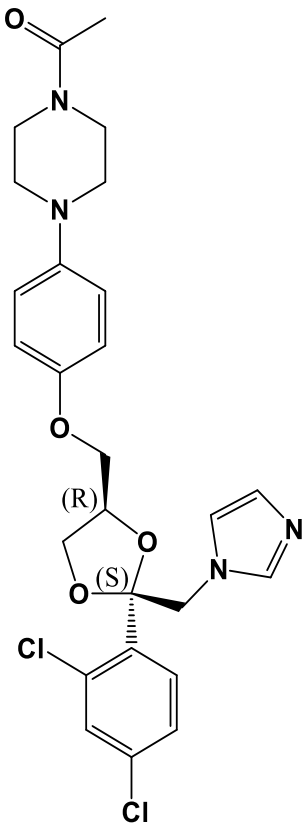

(2S,4R)-(-)-ketoconazole

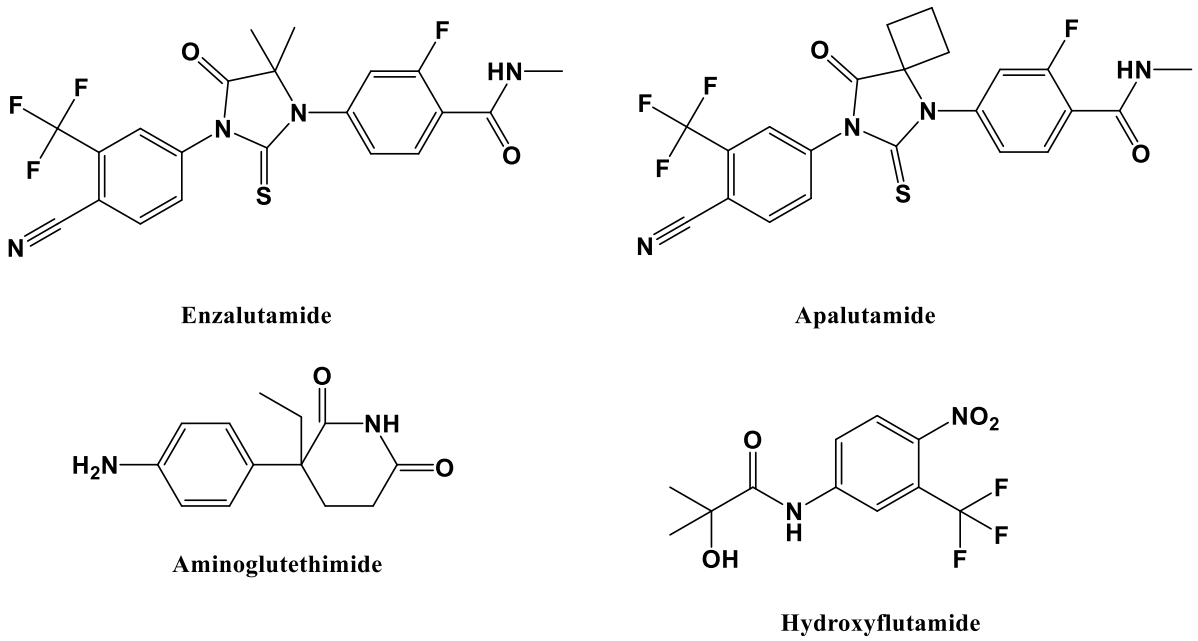

Fig. 2.2: Structural representation of non-steroidal anti-androgens.

2.5 Drawbacks of methods that have been used to detect anti-androgens

Various methods for detecting and quantifying anti-androgens, including FLU and its derivatives, are present in the literature. Methods such as spectrophotometry[47], chromatography[48] , polarography[49], mass spectroscopy[50], electrochemistry[51]. Most of the aforementioned and discussed methods are very powerful and accurate. In fact, some of these methods are considered standard techniques for determining a single drug molecule. However, they have some serious drawbacks associated with them. The detailed drawbacks are discussed below.

Even though spectrophotometry is still a sensitive, low-cost and rapid analysis method, it is highly susceptible to several parameters. The technique is restricted to a specific system and has limited applications due to its less reproducibility. The method is less accurate in measuring zero-crossing spectra. As a result of the likeness in the shape of derivative spectra and zero-order spectra, using this method results in small variations in a basic spectrum that can strongly modify the derivative spectrum. Poor reproducibility may alter results when different spectrophotometers used for zero-order spectra give similar results, but derivatization displays different results. This technique often does not allow the analysis of related substances, which makes it disadvantageous [52,53].

Photochemistry is mostly studied because the required energy in this technique is not as expensive as the energy required for methods using high-temperature and pressures or radiolytic processes. However, in this method, there may be rapid termination of photoreactions if products with competing absorptions are formed. In industry, photochemical production plants may acquire high unit capital costs. Photochemistry is a high-cost technique because the light is more expensive than heat. Due to the use of light, considerable losses occur during the electrical energy production process and the conversion thereof into usable light energy [54,55].

Spectrofluorimetry is known for its high sensitivity advantage compared to spectrophotometric methods and chromatographic techniques. Additionally, this method allows quantitation of some drugs in biological matrices because only a few molecules present luminescence native. However, spectrofluorimetry also has drawbacks, such as the likelihood of only analysing luminescent compounds. Not all compounds can be converted to fluorescent. The requirement of derivatization reactions that results in the more complex and time-consuming analysis is another drawback of the method. Spectrofluorimetry usually does not allow the analysis of related substances, limiting this technique in quality control applications [52].

Different chromatographic techniques have different advantages associated with them. Some of the advantages are simplicity, sensitivity, accuracy, and reproducibility. However, they also have drawbacks. Some chromatographic techniques require high-cost equipment, and highly trained technicians and must be handled with care and generate a lot of waste [52,56].

Despite its advantages, mass spectrometry has various side effects. The main advantage of this technique is that it is costly. Mass spectrometry also requires a highly trained technician, and it is not portable. While using this technique, it is difficult to differentiate among isomers of the molecule with the same charge-to-mass ratio. Also, chiral columns may be required to separate enantiomers [57]. Methods that have been used to detect and quantify FLU, BIC and OHF are summarised in **Table 2.3**.

Table 2.3. Summary of various techniques used to detect different anti-androgens.

Antiandrogen detected	Technique	Reference

FLU	Spectrophotometry	[58–60]
FLU	Photochemistry	[61–63]
FLU	Electrochemistry	[64–66]
FLU	Polarography	[67,68]
BIC	Spectrofluorimetry	[69,70]
BIC	Photochemistry	[71]
BIC	Chromatography	[72]
BIC	Electrochemistry	[51,73]
OHF	Chromatography	[74,75]
OHF	Mass spectrometry	[76]

2.6 Electrochemistry as a method for detection of anti-androgens

Electrochemical methods have shown great effectiveness in the detection and quantification of anti-androgens. However, despite their advantages and interesting properties, there is still a lack of information concerning the use of electrochemical sensors for quantifying AAs in WWTPs and STPs. The effectiveness of electrochemical sensors makes them promising candidates for use in WWTPs and STPs.

According to the literature, there are various electrochemical methods for the determination of AAs that have been reported and are effective. Methods such as LNW/CPE[77], CuO/GO/PANI[78], ZnO-Co_3O_4@C_3N_4 NC[79], $ZnMn_2O_4$-PGO nanocomposite[80] and s$Cu_2V_2O_7$/S-rGO nanocomposite[81]. However, the materials used in these methods have some limitations. The limitations include low sensitivity, high-cost of the precursor, as well as the use of separate instruments for synthesis [82]. This may be the reason for the lack of use of electrochemical sensors in WWTPs. Consequently, there is still a need for suitable materials to use as electrocatalysts for the detection of AAs. Metal oxide (MO) and rare-earth-based nanomaterials (NMs) have interesting properties that might come in handy if they are used as electrocatalysts.

2.7 Metal oxide nanomaterials (MONMs)

Recently, metal oxide nanomaterials (MONMs) have gained a lot of interest in research due to their distinctive properties. Properties include electrical, magnetic, mechanical, optical and chemical properties. Their properties are a result of their structural diversity. As a result, they have properties that are way better than those of their bulk materials[83–85]. Consequently, MONMs have been employed in a wide range of applications in various fields as catalysts [86,87], energy storage [88,89], water treatment [90,91], food packaging [92,93], wettability [94,95], optoelectronic devices [96,97], Li-ion batteries [98,99], semiconductor devices [100,101] and sensing [102].

Among (MOs), manganese oxide nanostructures (MnONSs) are loved for their low-cost, environmental benignity, high specific surface area, good electrocatalytic activity, good stability, excellent catalytic as well as selective ability[103,104]. Another interesting property of MNOs is their existence in different forms of stable oxide and crystal structures such as MnO, MnO_2, Mn_2O_3, and Mn_3O_4. MnOs also display a wide range of electrochemical properties along with the crystal structure, defect chemistry, morphology, and textures [82].

On the other hand, cobalt oxide nanostructures (CoONSs) are gaining attention because of their electrocatalytic properties, low-cost, environmental friendliness, excellent conductivity and chemical stability [105–108]. The transformation of Co^{2+} or Co^{3+} brings about high absorption of oxygen contents as well as distinctive surface reactivity on the surface of the material. Consequently, CoONSs provide excellent performance in many fields, such as pigments, electrochemistry and catalysis[109] . Various methods for the synthesis of MONMs have been reported in literature. These methods include co-precipitation[110], sol–gel[111], reverse micelle[112], thermal decomposition[113], hydrothermal synthesis [114] and microwave-assiste [115]. The various synthesis methods are discussed below.

2.7.1 Methods reported for the synthesis of MONMs

2.7.1.1 Precipitation method

Precipitation is a chemical method used in the synthesis of MONMs. According to literature, precipitation method is used because it does not require high-pressure and temperature[116]. In this method, impurities are eliminated during the filtration and

washing processes. This method is considered efficient and economical because it is simple, requires low-costs and is non-toxic [117,118].

Various metal oxide nanoparticles (MONPs) have been synthesised using the precipitation method. For instance, Zinc oxide NSs were synthesised by co-precipitation method by Hussain *et al* [119]. In a typical procedure, a zinc precursor was dissolved in distilled water. The solution was then added to a base solution drop by drop under stirring. Then the resultant solution was transferred into a beaker and maintained at room temperature for hours. A cleaned piece of Zn substrate was then immersed into the beaker to get the product. After the completion of the reaction, the substrate was washed and dried for several hours.

Kandpal *et al*[120] reported a co-precipitation method for synthesising iron-oxide NPs. In this method, a round bottom flask on a heating mantle set up was used in connection with a burette fitted on a burette stand. Firstly, deionised water was heated until equilibrium temperature was reached. Thereafter, the intended mass of the iron precursor was added to the water and stirred. A drop-wise addition of a weak base to the solution via a burette followed under stirring. After the system reached the precipitation stage, the precipitate was filtered, centrifuged, washed and dried.

Luna and Bangladesh Atomic Energy Commission [121] also reported a method for precipitation of copper oxide NPs. In this method, a copper precursor was dissolved in ethanol followed by a drop-wise addition of a base under stirring in room temperature. After precipitation, the precipitate was centrifuged, washed, dried and annealed.

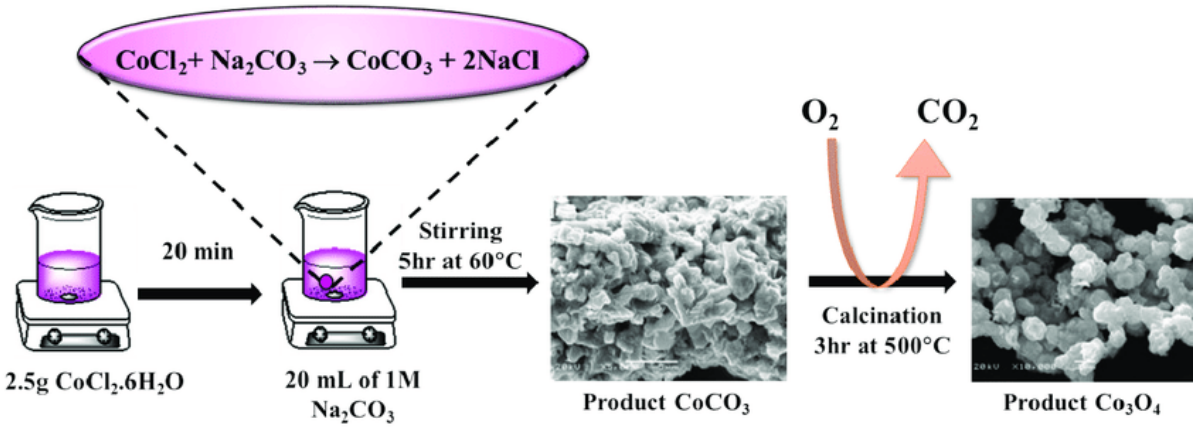

Fig. 2.3: Reaction scheme of the preparation of MONPs (adapted from *ref* [122]).

2.7.1.2 Sol-gel method

According to literature, the sol-gel method is the most promising method for the synthesis of NPs of controlled size and morphology[123]. Literature also credits the development of sol-gel synthesis methods for transition of metal oxides for a growing interest in the use of MONMs as catalysts for alcohol and sugar oxidation, medical applications, wastewater treatment and food industry [124]. According to literature[125], the Sol-gel method is advantageous because it offers homogenous, high purity, and high quality nanomaterials. One of the sol-gel synthesis was reported by Wahab *et al* [126]. Here, magnesium oxide NPs were synthesised by dissolving a magnesium precursor in deionised water followed by the drop-wise addition of a base under continuous stirring. After which the solution of the solution was measured while still stirring. The resulting precipitate was then filtered, washed, centrifuged and dried.

Kayani et al [127] also synthesised an iron-oxide sol. In this method, an iron precursor was gelated by adding its solution to a mixed solvent of acid and water under stirring. The sol was then heated under stirring and the water was evaporated. The resulting gel was then dried and annealed. Zinc Oxide NPs sol-gel synthesis method was reported by Alwan *et al* [128]. The zinc precursor was dissolved in double distilled water under continuous stirring until the precursor fully dissolved. Alcohol was then added to the solution under heating while still stirring. Under continuous stirring, a drop-wise addition of weak acid was performed. The solution was then incubated and dried. After drying, the product was washed and dried in a hot air oven.

Mousavi *et al* [129] also synthesised metal oxide NSs using the sol-gel method. In this method, a zinc precursor and a surfactant were dissolved in distilled water. An acid in different volumes was also dissolved in distilled water and added into the solution under magnetic stirring. The mixed solution stirred with a magnetic stirrer at a particular temperature for 1 h to obtain the gel. The as-obtained gel was dried and ground into a fine powder.

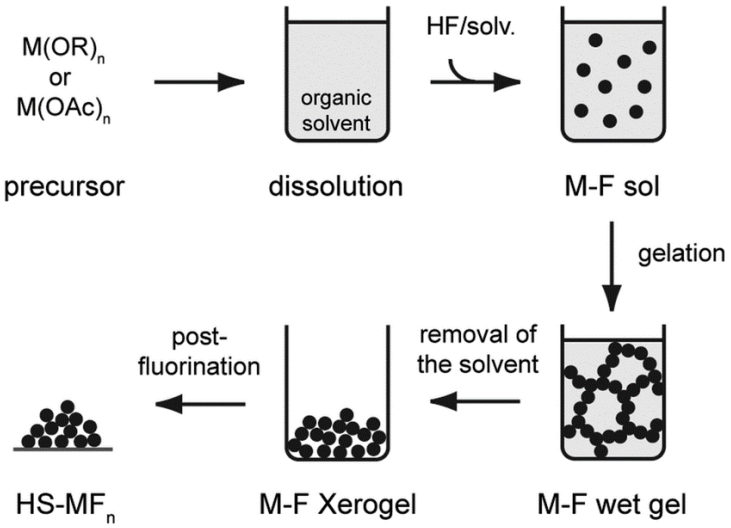

Fig. 2.4: The fluorolytic sol-gel synthesis scheme (adapted from *ref.* [130]).

2.7.1.3 Reverse micelle method

According to Noh *et al* [131], a reverse micelle method provides a simple route for producing various MONPs. The authors reported that a typical reverse micelle synthesis for MONPs involves the three steps. The first one being dissolving surfactants in an organic solvent. Followed by adding an aqueous solution containing metal precursor to the surfactant solution to produce reverse micelles acting as nanoreactors. The third one is the growth of NPs inside the micelles through the reaction of the metal precursor through the addition of a reactant.

Copper oxide NPs were synthesised by reverse micelle method by Rani *et al* [132]. In this method, a stable reverse micelle microemulsion was prepared by mixing a non-ionic surfactant, a polymer and a 1:9 ratio of an organic solvent and triple distilled water. The microemulsion was stirred rapidly in order to obtain a nice mixture. A copper solution was added to the microemulsion drop by drop with continuous stirring. A hydrazine hydrate solution was also added drop by drop to the microemulsion solution with continuous stirring at room temperature. The products were then washed and dried. Another reverse micelle method for metal oxide synthesis was reported by Lida *et al* [133]. In this method, iron-oxide NPs were synthesised using two reverse micelle solutions. The first one contained an iron aqueous solution, while the other contained that of a mixed solvent of two organic compound and an acid as a reducing agent. A surfactant was dissolved in heptane as an organic solvent under stirring. The

reverse micellar solution was allowed to stir for 24 hrs under ambient atmosphere. A chemical oxidant was then added to control the oxidation process. Furthermore, the resultant NPs were stabilized by the addition of a modifier molecule. Finally, iron-oxide NPs were filtered and washed.

Nickel oxide NPs were reported by Ahmad *et al* [134]. The micelle reaction was carried out by first synthesising nickel oxalate NPs from two micro-emulsions. Followed by subjecting the nickel oxalate NPs to a careful thermal decomposition to yield nanoparticulate nickel oxide. The micro-emulsions were composed of a surfactant, a co-surfactant, an organic compound, a nickel solution as the aqueous phase for the first microemulsion and ammonium oxalate as the aqueous phase for the second microemulsion. The two micro-emulsions were mixed slowly and stirred overnight. The resulting precipitate was separated from the apolar solvent and surfactant by centrifuging and washing. Finally, the precipitate was dried.

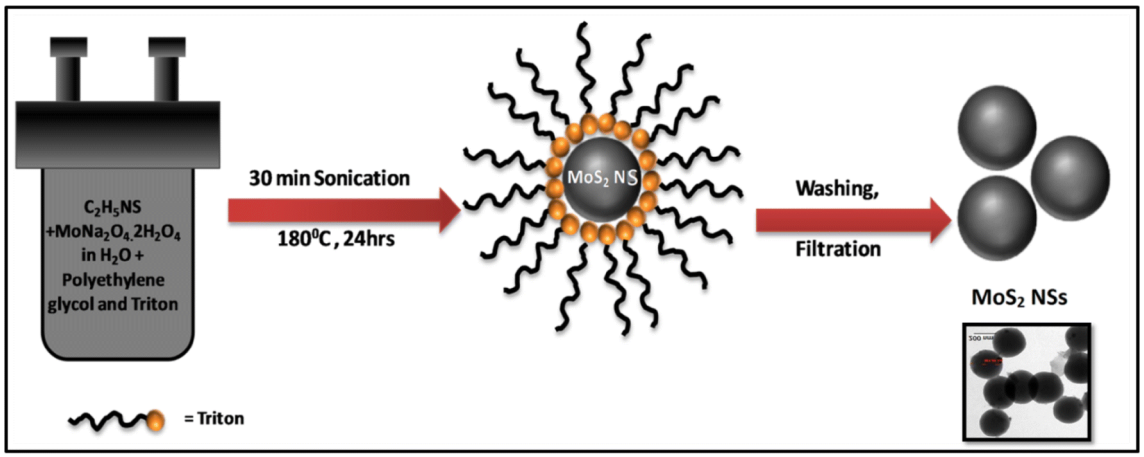

Fig. 2.5: Synthesis and formation scheme of MONPs by reverse micelle assisted hydrothermal route (Adapted from *ref* [135]).

2.7.1.4 Thermal decomposition method

Daengsakul *et al* [136] reported that thermal decomposition method is fast, simple, and cost-effective. According to the authors, thermal decomposition is a promising synthesis method for preparing MONPs. Salavati-Niasari et al [137] also agree that thermal decomposition is a simple process, requires low-costs and makes obtaining high purity products simple. Furthermore, the authors reported that this method is promising and a simplistic route for industrial applications. A method for synthesis of mercury oxide NPs has been reported by Mohadesi *et al* [138]. In this method, the NPs

were synthesised by transferring a mercury precursor to an external pipe in a vacuum set. The system was then vacuumed by a pump. Later, water entered the inner pipe from one side and exited from the other side. The water circulation was done in order to solidify the product vapours. The resulting product was then heated. After heating, the precipitations were collected. The as-obtained $Hg(OAc)_2$ nanostructures was loaded into a silicon boat. The boat was then put in a high-temperature tube furnace. After the thermal treatment of the sample, the system was cooled to room temperature naturally, followed by the collection of the obtained precipitates.

Hosseinpour-Mashkani and Ramezani [139] reported a thermal decomposition method for synthesising silver oxide NPs. Here, a silver precursor was dissolved in distilled water. An acid was then added to the solution drop by drop while stirring. Finally, the resulting precipitate was obtained, washed and then dried in vacuum. The as-obtained [Ag(Hsal)] was then loaded into a silicon boat and put in a high-temperature tube furnace in an argon and air atmosphere to synthesise. The set was heated and the products were collected after hours.

Salavati-Niasari and Davar [140] also synthesised copper oxide NPs using a thermal decomposition method. In this method, a solution containing a copper precursor and a surfactant was slowly heated under nitrogen. The solution was continuously heated slow for 45 min and then quickly heated to a higher temperature. The high heating was carried out for an hour before it could be cooled to room temperature. After precipitation, the synthesised Cu NPs were exposed to air.

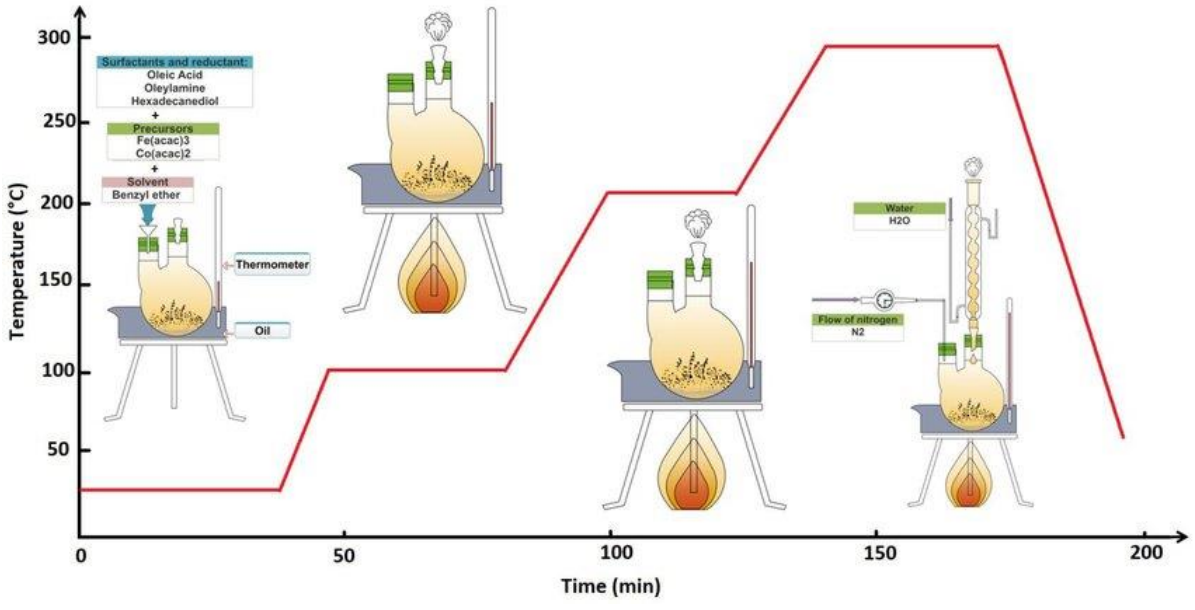

Fig. 2.6: Synthesis scheme of thermal decomposition method (adapted from *ref* [141]).

2.7.1.5 Hydrothermal synthesis method

According to Zulkifli *et al* [142], the hydrothermal synthesis method is a powerful method for the synthesis of MONPs at a considerably low temperature, energy saving and cost-effective benefits. Furthermore, the authors reported that the method is advantageous because it brings about controllable particle size, morphology and a good degree of crystallinity. In addition, Sundrarajan et al[143] reported that hydrothermal synthesis method is green, environmentally friendly, and cost-effective. They also reported that the method promotes self-aggregation, well-defined morphology as well as controlled shape and size of the NPs. Babu and Narayanan[144] reported a hydrothermal synthesis method of zinc oxide NPs. Here, a zinc precursor and a base salt were dissolved in distilled water. Thereafter, the mixture was magnetically stirred, and the obtained solution was transferred into a 50 mL Teflon-lined stainless-steel autoclave. The mixture was then heated at a regulated temperature. After cooling, the obtained powders were collected, centrifuged, and washed. The powders were then dried.

Another hydrothermal synthesis method was reported by Arun *et al* [145]. Copper oxide NPs were prepared dissolving a copper precursor in double distilled water. This was followed by an addition of a base under continuous stirring in order to get the desired pH value. The solution was then transferred into a Teflon-lined sealed stainless-steel autoclaves and heated in an oven for several hours at a regulated temperature. After cooling, the precipitate obtained was annealed in air. Tin oxide NPs were synthesised hydrothermally by Viet *et al*[146]. The tin NPs were prepared by dissolving a tin precursor in a mixed solution of deionised water and hydrazine hydrate. After that, solution was adjusted to the desired pH by adding a base. The solution was then transferred into a stainless autoclave and heated at a regulated temperature for hours. After cooling, the product was centrifuged, filtered out, rinsed and dried.

Zinc oxide NSs, consisting of nanopencils were synthesised by Akhoon *et al* [147] using hydrothermal synthesis. In this method, a zinc powder was dissolved in distilled water in a stainless-steel chamber with 60 ml capacity. The stainless-steel chamber was then heated in an oven at a high-temperature for hours. After reaction, the system was

allowed to cool down under normal conditions. The products were retrieved and centrifuged twice before drying in open air conditions at a certain temperature.

Ohara *et al* [148] also used hydrothermal synthesis to synthesisze zinc oxide nanorods (NRs). Here, a zinc precursor was dissolved in DI water. The resultant solution was then transferred into a reactor using a high-pressure pump at a certain flow rate and mixed with supercritical water at a certain temperature and flow rate. At the exit end of the reactor, the solution was quickly quenched by addition of a base solution by an external water jacket. Then, the resultant particles were collected using an upstream in-line filter. The pressure of the experiment was controlled by using a back pressure. Several organic reagents were used to modify the surface of the particles under supercritical conditions for the in-situ surface treatment experiments.

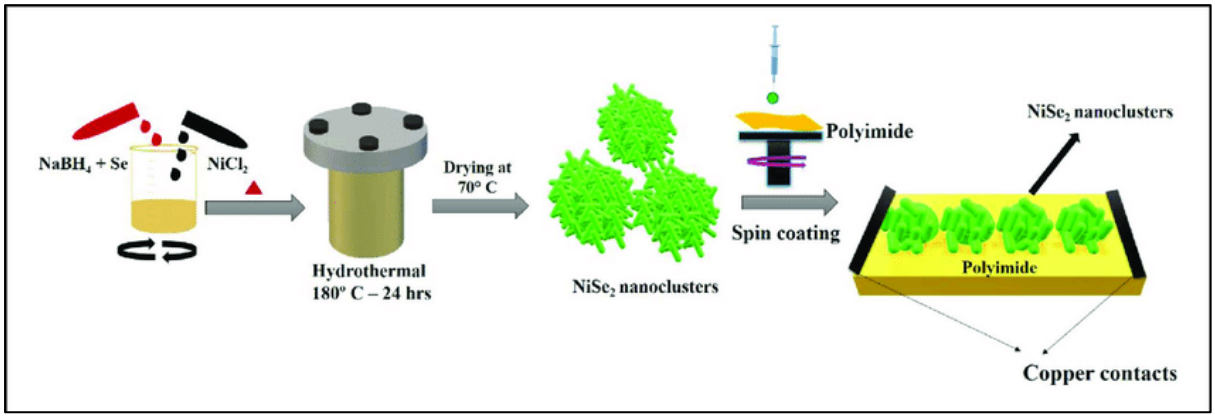

Fig. 2.7: Schematic diagram of the hydrothermal synthesis of nanoclusters (adapted from *ref* [149]).

2.7.1.6 Microwave-assisted method

Hasanpoor *et al* [150] reported that microwave-assisted synthesis methods have been used and explored widely to synthesise oxide, hydroxide and sulfide NPs. Furthermore, the report specified that the method is simple, clean, and does not have thermal gradient effects problems. The authors reported the advantages of the method, as compared to convenient hydrothermal methods, are quick reaction, short period of suitable temperature reach, simple medium and morphology particle control. According to Palchik *et al* [151], the microwave-assisted method has been employed for the acceleration of organic chemical reactions for a long time due to its speed, simplicity and high energy efficiency. Even though the exact nature of the interaction of the microwaves with the reactants during the synthesis of materials is somewhat

unclear and speculative, the authors say that it is well known that the interaction of microwaves with dielectric materials, solids or liquids lead to dielectric heating. Tin oxide NPs have been synthesised via the microwave, assisted by Krishnakumar *et al* [152]. A tin precursor was dissolved in deionised water. Then pH adjusted to the desired value using liquid ammonia diluted with water. The resulting precipitate was washed until no chlorine ions were detected. The precipitate was further washed with ethanol to remove NH_4^+ ions. The resulting precipitate was irradiated with a household microwave oven at the radiation frequency of 2.45 GHz and its power up to 1 kW.

Bhatt *et al* [153] synthesised cobalt oxide NPs using a microwave-assisted method. Typically, a cobalt precursor was dissolved in ethylene glycol. A surfactant was added to the solution and sonicated to attain homogeneity. The solution was then transferred to a Teflon-lined vessel and subjected to microwave irradiation (QWave 1000) at high power. The obtained solution was centrifuged and washed. The precursor was finally dried.

Mohammadyan et al. [154] also synthesised nickel oxide NPs using the microwave synthesis method. The synthesis was conducted in three stages: (i) formation of $Ni(OH)_2$ precursor, (ii) microwave irradiation of the precursor and (iii) heat treatment of the precursor to convert it into nickel oxide. The first stage was done by the drop-wise slow addition of a base to a nickel precursor while stirring until the desired pH was reached. The mixture was then irradiated by a microwave (2.45GHz, 900W, SAMSUNG). Simultaneous thermal analysis was conducted to determine the precursor to nickel oxide conversion temperature under air. Thermal analysis measurement followed according to the following procedure: (i) holding the material at 30°C for 1min, (ii) heating up from 30 to 600°C at a temperature rate of 10°C min, and (iii) holding the product at 600°C for 10min. After determining the temperature of nickel hydroxide to nickel oxide conversion by thermal analysis, the oven-dried cake was heated. The powder was finally washed and filtered.

Lin and Yeh [155] used the microwave-assisted method to synthesise zinc oxide NRs. In this method, the NRs were prepared from solutions of two zinc precursors on the Whatman No. 93 chromatography paper with a seed layer prepared from immersed-in-zinc solution followed by heating at a certain temperature for an hour. The chromatography paper with a seeding layer was immersed in the solution containing

a base, a zinc precursor, a hardening component, and a polymer. Synthesis was performed using conventional and microwave-assisted hydrothermal methods. For the hydrothermal synthesis, the resultant solution was transferred into a teflon-lined stainless-steel autoclave and heated in a furnace for hours. The resulting solution was heated using a microwave digesting system for the microwave-assisted hydrothermal synthesis.

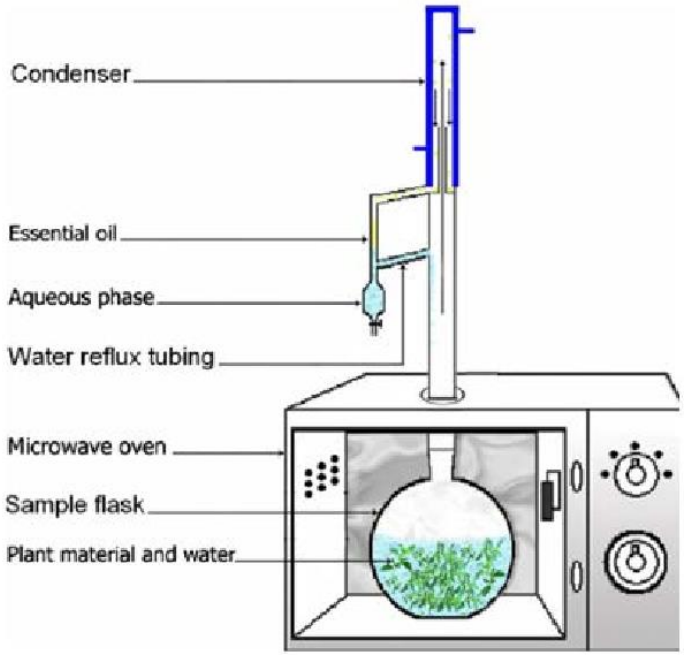

Fig. 2.8: Schematic diagram of the microwave-assisted hydro-distillation apparatus (adapted from *ref* [156]).

2.7.1.7 Electrodeposition method

Electrodeposition has been reported as a unique, simple, fast, inexpensive, and binder-free technique that produces nanoparticles with controlled characteristics. The characteristics include size, the composition and morphology. The method has advantages which include the nanoparticle being directly attached to the substrate. Furthermore, in comparison to other techniques, the crystallographic orientation, particle size, thickness, mass, and morphology of the nanostructured materials can be controlled by adjusting the operating conditions and bath chemistry[157].

Babaei-Sati et al [158] synthesised Pure PPy and PPy/ metal oxide nanocomposites electrochemically by the potentiostatic method with an electrochemical workstation (electroanalyzer system SAMA 500, Iran) in a conventional three-electrode undivided

cell. Here metal oxide NPs were dispersed in an acid by using ultrasonic bath for 60 min. A monomer was dissolved in electrolyte solution under stirring. The prepared solutions were deaerated by bubbling purified nitrogen prior to electrodeposition. The working electrode in this case was Mild steel (St37) electrode. The rod form of MS electrode was then insulated with polyester resin and thus only its cross section (1 cm^2) was allowed to contact the electrolyte. A graphite rod and saturated calomel electrode (SCE) were used as counter and reference electrodes, respectively. The working electrode was polished and then washed before electrodeposition. For electrodeposition, a cyclic potential from –0.5 to 1.2 V vs. SCE at a scan rate of 10 mVs^{-1} was applied. Thereafter, electropolymerization was continued at a constant potential of +0.95 V vs. SCE for 200 s. During the polymerization, the electrolyte solution was kept under slow speed magnetic stirring.

Chou et al[159] synthesised γ-MnO2 nanostructured thin films via electrodeposition under room temperature with three electrode system. Before to electrodeposition, the nickel sheets as working electrodes were polished to a smooth surface finish. The reference electrode was a saturated calomel electrode (SCE), and the counter electrode was a graphite rod with high density and high surface area. The electrolyte was composed of 0.1 M Na_2SO_4 and 0.1 M $Mn(CH_3COO)_2$ at pH 6.0. The use of a potentiostatic method under 0.6 V (SCE) resulted in the preparation of MnO_2 thin films. The MnO_2 nanoflakes were synthesized by cycling for 15 min in combination of cyclic voltammetric technique in the potential range +0.60 V and +0.30 V (SCE) under the speed of 250 mV s^{-1} for 30 s and PS technique in the potential of 0.6 V (SCE) for 1.5 min. The MnO_2 naoflakes were obtained through combination of CV and PS techniques for 5 min, 15 min, 30 min, respectively.

In light of the above, all these have been used due to certain advantages related to them. For some, it is because they require low-costs and are non-toxic; for some it is because they offer high purity results and promote energy saving. However. Some of these methods have drawbacks despite their advantages.

2.7.2 Disadvantages of the synthesis methods for MONMs

Some of the aforementioned methods for the synthesis of MONPs are very good. Moreover, some of these methods are considered standard synthesis methods. However, they have some serious drawbacks associated with them. The precipitation

has the main disadvantage of generating unwanted by-products and waste disposal issues [160]. The sol-gel method has a variety of severe disadvantages. Some of them include a large shrinkage caused by the gelation process and the drying of gels; huge concentrations of pores; high-cost of raw materials; long processing times; lack of scientific understanding of the many complexities associated with the process; moisture sensitivity that causes short shelf life of the solutions [161,162].

The disadvantages of reverse micelle methods are the generation of widely agglomerated NPs, poor crystallinity because of the relatively low temperature, and very low yield of NPs from a large amount of solvent [163]. The disadvantages of the microwave-assisted method are briefer crystallization time and homogeneous nucleation due to the microwave oven uniform heat. The disadvantages of hydrothermal synthesis methods are challenges to control and limitations of reliability and reproducibility [164].

Among all the methods, hydrothermal synthesis methods are the most reliable because their drawbacks are not related to environmental toxicity, high-costs or lack of good crystallinity. Hydrothermal synthesis methods are further advantageous because they produce size-controlled nanomaterials with defined structural properties, desired size and shape nanoparticles, well-crystallized powder, and nanocrystals with high crystallinity[165]. Using a hydrothermal method to synthesise metal oxide electrocatalysts will be an advantage.

2.8 Advantages of nanomaterials as electrocatalysts

Nanomaterials are impactful in every sphere of human life. They are employed in as little as cosmetics to drug research. The use of nanosized materials is thought to be a factor that could benefit the performance of sensors. Nanomaterials have a variety of innovative and remarkable physical and chemical properties. Low-dimensional nanomaterials and structures have defined new scientific research areas within the past decades [166].

2.8.1 Nanostructures (NSs)

NSs have attracted quite a lot of attention from scientists. The larger surface area in a small structure of these materials is beneficial when it comes to enhancing the efficacy of surface reactions together with strong adsorption capacity, efficient loading capability and excellent catalytic ability[167]. Consequently, many NSs have mainly been

developed and employed in many fields such as sensors[168], catalysis[169], energy storage[170], cancer therapy[171], and healthcare[172]. The use of NSs as electrocatalysts will increase the sensor's surface area, increase the sensor's porosity and accelerate electron transfer between the electrode and the detection species.

2.8.2 Nanorods (NRs)

NRs structures have drawn a lot of interest in solar energy conversion. Among the different geometries of NRs, radial p-n junction geometry is said to have the potential to enhance cell efficiency due to the normality between carrier transport and light absorption directions. Furthermore, NRs are said to be more advantageous than other NPs. This is because NRs have the capability of making charge carrier transfer to the electrodes through their optimal arrangement without loss. NRs also have large inner surface areas that can easily be filled with liquid, allowing intimate contact with electrolyte [173]. NRs have been used in various applications such as biomedicine [174], Lithium-ion batteries [175], biosensors [176], drug delivery [177], and cancer therapies [178].

Using NRs as electrocatalysts is an advantage because they will bring about enhanced efficiency, good charge carrier transfer and large surface area. However, the NRs will be decorated with NSs to enhance their electrocatalytic behaviour towards detecting FLU and its derivatives, BIC and OHF.

2.8.3 Advantages of decorating NRs with NSs

Decorating NRs with NSs will be advantageous because it will bring about extremely large surface area, high porosity, improved reactivity and good mechanical properties [179]. Using NRs and NSs in sensors has advantages such as increased sensor surface area, chemical accessibility, electrocatalysis, electrical conductivity, and connectivity[180]. These nanomaterials enlarge the electrochemically active areas, accelerate electron transfer amongst electrodes and detection species and behave as biocompatible frameworks for biomolecule control in electrochemical biosensors [181].

Using NRs and NSs as electrocatalysts will be advantageous because it will result in excellent catalytic ability towards detecting FLU, BIC and OHF. These remarkable advantages will lead to a novel electrochemical sensor with better performance, stability, selectivity and sensitivity. This study will allow the detection and quantification of the amounts of FLU and its derivatives in actual samples. Using a glassy carbon

electrode modified with NRs and nanostructures as electrocatalysts will be advantageous as the nanomaterials have interesting advantages.

2.9 Anti-androgens

The study focused on the AAs FLU (**1**), BIC (**2**) and OHF (**3**), as shown in **Fig. 2**. FLU and its derivatives were chosen in this study to develop a model that covers a wide scope for the detection of AAs. All the AAs in the study have FLU as a parent compound, as depicted in structures **1-3** in **Fig. 2**.

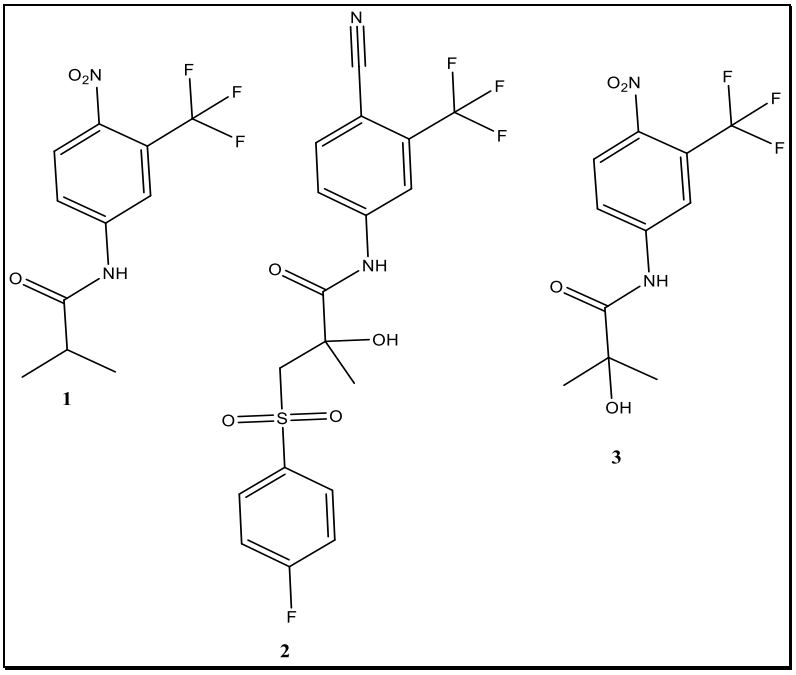

Fig. 2.9: Chemical structures of FLU (**1**), BIC (**2**) and OHF (**3**) to be employed as analytes in this study

Flutamide

FLU is defined as a synthetic, non-steroidal, pure antiandrogen drug. It is a widely used drug for the treatment of men who are diagnosed with prostate cancer. FLU also treats excess androgen levels in women with polycystic ovarian syndrome [182]. It has a wide application in the treatment of hirsutism and acne [183]. Its mechanism of action involves blocking the effect of testosterone (a natural hormone responsible for the growth and spread of prostate cancer cells in humans) from mediating its biological effects [184]. After human consumption, FLU is mainly excreted in urine and in low amounts in faeces as an unchanged drug and hydroxylated metabolites, mainly OHF

[185]. When overdosed, FLU may cause some severe side effects such as inflamed prostate, blood in urine, rectal bleeding, hot flashes, loss of sexual interest/ability, diarrhoea, nausea, vomiting, enlarged growth of male breasts, drowsiness, liver malfunction as well as methemoglobinemia [186,187].

Bicalutamide

BIC (also known as Casodex®) is a non-steroidal pure antiandrogen drug used for the early treatment of nonmetastatic prostate cancer. Its anti-androgenic activity dwells almost exclusively in the (R) - enantiomer, with very little activity dwelling in the (S)-enantiomer. BIC works by binding to cytosolic androgen receptors in prostate cells. It inactivates androgen-regulated prostate cell growth and function. Consequently, this results in cell apoptosis and inhibition of prostate cancer growth. Contrasting steroidal AAOs, BIC does not have progestogenic activity and does not suppress gonadotropin secretion or sex hormone production. When consumed by humans, BIC metabolites are excreted more or less equally in urine and faeces with little or no unchanged drug excreted in the urine. Contrariwise, unchanged drug predominates in plasma [188,189].

The continuous consumption and overdose of BIC may cause some severe side effects such as a change in weight (loss or gain), loss of appetite, dizziness, pain, burning, or tingling in the hands or feet, difficulty sleeping, the feeling of uneasiness or dread, rash, sweating, inability to get or keep an erection, need to urinate frequently during the night, bloody urine, painful or difficult urination, frequent and urgent need to urinate, difficulty emptying the bladder as well as sore or swollen breasts [190,191].

Hydroxyflutamide

OHF is an active metabolite of FLU. When FLU is consumed, it is then excreted either as an unchanged compound or as its metabolite, OHF. OHF works by binding to the androgen receptor, inhibiting androgen receptor-mediated transcriptional activity. Consequently, causing a disturbance to the actions of endogenous androgens, thus blocking them from mediating their biological effects [192,193]. **Table 2.4** shows AAs of interest, their band names, and the manufacturers.

Table 2.4. AAs of interest and their brand names

Non-steroidal AAs

Genetic name	Brand name	Manufacturer
BIC	Ablu	Neon laboratories limited
	Caludec	Samarth Pharma Pvt. Ltd.
	Caluran	Ranboxy Laboratories Ltd.
	Casodex	AstraZeneca
FLU	Proscan	Renata limited
	Eulixin	Schering
	Cytomid	Cipla limited.
	Flutacare	Criticare Labotories Pvt. Ltd.
OHF	OHF	Fox Chemicals GmbH
	OHF	CM Fine Chemicals
	OHF	Xingrui Industry Co., Limited
	OHF	Ambeed, Inc.

In light of the above, the AAs in the study are necessary and effective in treating prostate cancer. However, they have severe effects when continuously consumed and are not cancer specific. In that, they can affect organs which are not their target. Which is why it is essential to detect, quantify and control them. Hence this study detects and quantifies these AAs in actual samples.

References

1. Isidori, M., Lavorgna, M., Russo, C., Kundi, M., Žegura, B., Novak, M., Filipič, M., Mišík, M., Knasmueller, S., de Alda, M.L. and Barceló, D. Chemical and toxicological characterisation of anti-cancer drugs in hospital and municipal wastewaters from Slovenia and Spain. *Environ. Pollut*. **219**, 275-287 (2016).

2. Singh, S. M., Gauthier, S. and Labrie, F. Androgen Receptor Antagonists Activity Relationships. *Curr. Med. Chem*. **7**, 211–247 (2000).

3. Ganjali, M.R., Habibi-Kool-Gheshlaghi, M., Nasri, F. and Larijani, B. Electrochemical Determination of Flutamide, a Non-steroidal Antiandrogen Prescribed in Prostate Cancer. *Anal. Bioanal. Electrochem*. **14**, 348–361 (2022).

4. Trautwein, C. and Kümmerer, K. Chemosphere Incomplete aerobic degradation of the antidiabetic drug Metformin and identification of the bacterial dead-end transformation product Guanylurea. *Chemosphere* **85**, 765–773 (2011).

5. Vumazonke, S., Khamanga, S. M. and Ngqwala, N. P. Detection of pharmaceutical residues in surface waters of the Eastern Cape Province. *Int. J. Environ. Res. Public Health.* **17**, 1–13 (2020).

6. Rowney, N.C., Johnson, A.C. and Williams, R.J. Cytotoxic drugs in drinking water: a prediction and risk assessment exercise for the Thames catchment in the United Kingdom. *Environ. Toxicol. Chem*. **28**, 2733-2743 (2009).

7. Jureczko, M. and Kalka, J. Cytostatic Phamaceuticals as water contaminants Cytostatic Pharmaceuticals as water contaminants. *Eur. J. Pharmacol.* **866**, 172816 (2019).

8. Remesh, A. Toxicities of anti-cancer drugs and its management. *Int. J. Basic Clin. Pharmacol.* **1**, 2 (2012).

9. Nawa, H., Niimura, T., Hamano, H., Yagi, K. and Goda, M. Evaluation of Potential Complications of Interstitial Lung Disease Associated With Anti-androgens Using Data From Databases Reporting Spontaneous Adverse Effects. *Front. Pharmacol*. **12**, 1–6 (2021).

10. Montani, D., Bertoletti, L., Chaumais, M.C., Perrin, S., Fabre, D., Chaouat, A., Jaïs, X., Simonneau, G. and Humbert, M. Chronic thromboembolic pulmonary hypertension complicating long-term cyproterone acetate therapy. *Eur. Respir. Rev*. **23**, 260–263 (2014)

11. Hamzah, A.B.A., Choo, Y.M., Hassali, M.A., Saleem, F. and Verma, A.K. Disseminated Intravascular Coagulation and Excessive Fibrinolysis (DIC XFL) Syndrome in Prostate Cancer: A Rare Complicated Disorder. *J. Clin. Diagnostic Res.* **11**, 10– 12 (2017).

12. Barber, N. A. and Ganti, A. K. Pulmonary toxicities from targeted therapies: a review. *Target. Oncol*. **6**, 235–243 (2011.

13. de Bono, J.S., Fleming, M.T., Wang, J.S., Cathomas, R., Miralles, M.S., Bothos, J., Hinrichs, M.J., Zhang, Q., He, P., Williams, M. and Rosenbaum, A.I hase I Study of MEDI3726: A Prostate-Specific Membrane Antigen-Targeted Antibody–Drug Conjugate, in Patients with mCRPC after Failure of Abiraterone or Enzalutamide Safety, Efficacy, and Pharmacokinetics of MEDI3726 in mCRPC. *Clin. Cancer Res*. **3**, 3602–3609 (2021).

14. Umeojiako, W. I., James, M., Hospital, D. V. and Road, D. W. Bicalutamide-induced Eosinophilic Pneumonitis - A Serendipitous Diagnosis. *J. Med. Case. Rep.* **8**, 4–9 (2019).

15. Cardwell, C. R., Sullivan, J. M. O. and Mcmenamin, Ú. C. Hormone therapy use and the risk of acute kidney injury in patients with prostate cancer: a population- based cohort study. *Prostate Cancer Prostatic Dis*. **24**, 1055–1062 (2021).

16. Chen, K.C., Chen, C.R., Chen, C.Y., Tzou, K.Y., Peng, C.C. and Peng, R.Y. Bicalutamide elicits renal damage by causing mitochondrial dysfunction via ROS damage and upregulation of HIF-1α*. Int. J. Mol. Sci*. **21**, 3400 (2020).

17. Malyszko, J., Tesarova, P., Capasso, G. and Capasso, A. Review The link between kidney disease and cancer: complications and treatment. *Lancet.* **396**, 277–287 (2020).

18. Verzicco, I., Regolisti, G., Quaini, F., Bocchi, P., Brusasco, I., Ferrari, M., Passeri, G., Cannone, V., Coghi, P., Fiaccadori, E. and Vignali, A. Electrolyte Disorders Induced by Antineoplastic Drugs. *Front. Oncol.* **10**, 1– 16 (2020).

19. Katzer, T., Leite, A., Ruy, J. and Cristiane, B. Physiopathology and current treatments of androgenetic alopecia: Going beyond androgens and anti-androgens. *Dermatol. Ther*. **32**, 1–10 (2019).

20. Park, A. M., Khan, S. and Rawnsley, J. Hair Biology Growth and Pigmentation. *Facial Plast. Surg. Clin. North Am.* **26**, 93105 (2018).

21. Subbaiah, V. and Rao, P. Malatyadya Kera Taila in the Management of Indralupta : A Case Report. Int. J. Ayurveda Pharma. Res. **6640**, (2017).

22. Alessandrini, A. and Piraccini, B. M. Common causes of hair loss – clinical manifestations, trichoscopy and therapy*. J. Eur. Acad. Dermatol*. **35**, 629–640 (2021).

23. Akbari, S., Kariznavi, E., Jannati, M., Elyasi, S. and Tayarani-najaran, Z. Curcumin as a preventive or therapeutic measure for chemotherapy and radiotherapy induced adverse reaction : A comprehensive review. *Food Chem. Toxicol*. **145**, 111699 (2020).

24. Monaco, S., Mehrad, M. and Dacic, S. Recent advances in the diagnosis of malignant mesothelioma: focus on approach in challenging cases and in limited tissue and cytologic samples. *Adv. Anat. Pathol*. **25**, 24-30 (2018).

25. Moradi, F., Enjezab, B. and Ghadiri-anari, A. Diabetes and Metabolic Syndrome : Clinical Research and Reviews The role of androgens in COVID-19. *Diabetes Metab. Syndr. Clin. Res. Rev.* **14**, 2003–2006 (2020).

26. Starace, M., Orlando, G., Alessandrini, A. and Maria, B. Female Androgenetic Alopecia : An Update on Diagnosis and Management. *Am. J. Clin. Dermatol.* **21**, 69–84 (2020).

27. Murina, F., Barbieri, S., Lubrano, C. and Cetin, I. Vestibular Mucosa Thickness Measured by Ultrasound in Patients Affected by Vestibulodynia : A Case-Control Study. *Sex. Med.* **9**, 100320 (2021).

28. Pereira, J. R. Cancer treatment with hormone therapy and its relationship with xerostomia and hyposalivation. *Care Cancer*. **23**, 1–10 (2020).

29. Newman, N. B. *et al.* Long-Term Bone Marrow Suppression During Postoperative Chemotherapy in Rectal Cancer Patients After Preoperative Chemoradiation Therapy. *Radiat. Oncol. Biol.* **94**, 1052–1060 (2016).

30. Aksoy, D.Y., Tanriover, M.D., Uzun, O., Zarakolu, P., Ercis, S., Ergüven, S., Oto, A. Diarrhea in neutropenic patients: a prospective cohort study with emphasis on neutropenic enterocolitis. *Ann. Oncol*. **18**, 183–189 (2007).

31. Stasi, R. How to approach thrombocytopenia. *Hematology Am. Soc. Hematol. Educ. Program Book.* **2012**, 191–197 (2012).

32. Yang, Y., Zhang, W., Li, Y., Fang, G. and Zhang, K. Scalded Skin of Rat Treated by Using Fibrin Glue Combined with Allogeneic Bone Marrow Mesenchymal Stem Cells. *Ann Dermatol*. **26**, 289–295 (2014).

33. Galloway, R., Dusch, E., Elder, L., Achadi, E., Grajeda, R., Hurtado, E., Favin, M., Kanani, S., Marsaban, J., Meda, N. and Moore, K.M. Women's perceptions of iron deficiency and anemia prevention and control in eight developing countries. *Soc. Sci. Med*. **55**, 529–544 (2002).

34. Haurie, C., Dale, D.C. and Mackey, M.C. Cyclical neutropenia and other periodic hematological disorders: a review of mechanisms and mathematical models. Blood. *Am. J. Hematol.* **92**, 2629-2640 (1998).

35. Izak, M. and Bussel, J. B. Management of thrombocytopenia. F1000prime reports.**10**, 1-5 (2014).

36. Ngqwala, N. P. and Muchesa, P. Occurrence of PCs in aquatic environments: A review and potential impacts in South Africa. *S. Afr. J. Sci.* **116**, 1–12 (2020).

37. Coscia, I. and Kaiser, M.J. The impact of the human activities on aquatic ecosystems. *J. Fish Biol*. **101**, 408–413 (2022).

38. Grönberg, H. Prostate cancer I Prostate cancer epidemiology. *The Lancet.* **361**, 859–864 (2003).

39. Li, D., Chen, H., Liu, H., Schlenk, D., Mu, J., Lacorte, S., Ying, G.G. and Xie, L. Anti-cancer drugs in the aquatic ecosystem : Environmental occurrence, ecotoxicological effect and risk assessment. *Environ. Int.* **153**, 106543 (2021).

40. Bhatia, H. and Kumar, A. Does anti-androgen , flutamide cancel out the in vivo effects of the androgen , dihydrotestosterone on sexual development in juvenile Murray rainbowfish (Melanotaenia fluviatilis)? *Aquat. Toxicol*. **170**, 72–80 (2016).

41. Bhatia, H., Kumar, A., Chapman, J. C. and Mclaughlin, M. J. Ecotoxicology and Environmental Safety Effects of short-term exposure to the model anti-androgen, flutamide on reproductive function based endpoints in female Murray rainbow fish (Melanotaenia fl uviatilis). *Ecotoxicol. Environ. Saf.* **109**, 143–151 (2014).

42. Kiparissis, Y., Metcalfe, T. L., Balch, G. C. and Metcalfe, C. D. Effects of the anti- androgens , v inclozolin and cyproterone acetate on gonadal de v elopment in the Japanese medaka (Oryzias latipes). *Aquat. Toxicol.* **63**, 391–403 (2003).

43. Li, Y., Kang, Q., Chen, R., He, J., Liu, L., Wang, L. and Hu, J. 2 - Ethylhexyl Diphenyl Phosphate and Its Hydroxylated Metabolites are Anti-androgenic and Cause Adverse Reproductive Outcomes in Male Japanese Medaka (Oryzias latipes). *Environ. Sci. amp; Technol.* **54**, 8919-8925 (2020).

44. Bayley, M., Junge, M. and Baatrup, E. Exposure of juvenile guppies to three anti- androgens causes demasculinization and a reduced sperm count in adult males. *Aquat. Toxicol*. **56**, 227–239 (2002).

45. Kinnberg, K. and Toft, G. Effects of estrogenic and anti-androgenic compounds on the testis structure of the adult guppy (Poecilia reticulata). *Ecotoxicol. Environ. Saf*. **54**, 16–24 (2003).

46. Rouse, E. F., Coppenger, C. J. and Barnes, P. R. The Effect of an Androgen Inhibitor on Behavior and Testicular Morphology in the Stickleback Gasterosteus aculeatus. *Horm. Behav.* **18**, 8–18 (1977).

47. Swamivelmanickam, M., Gomes, A. R., Manavalan, R., Satyanarayana, D. and Reddy, P. G. Determination and validation of UV spectrophotometric method for estimation of BIC tablet. *Int. J. ChemTech Res.* **1**, 1189–1193 (2009).

48. Saka, C. Critical Reviews in Analytical Chemistry Chromatographic Methods for Determination of Drugs Used in Prostate Cancer in Biological and Pharmacological Samples Chromatographic Methods for Determination of Drugs Used in Prostate Cancer in Biological and Phar. *Crit. Rev. Anal. Chem.* **49**, 78–99 (2019).

49. Niknam, P., Jamehbozorgi, S., Rezvani, M. and Izadkhah, V. Understanding delivery and adsorption of FLU drug with ZnONS based on: Dispersion-corrected DFT calculations and MD simulations. *Phys. E Low-Dimensional Syst. Nanostructures.* **135**, 114937 (2022).

50. Suresh, P. S., Srinivas, N. R. and Mullangi, R. Review of HPLC and LC–MS/MS assays for the determination of various non-steroidal anti-androgens used in the treatment of prostate cancer. *Biomed. Chromatogr.* **32**, 4034 (2018).

51. Kogularasu, S., Akilarasan, M., Chen, S. M. and Sheu, J. K. Scalable and sustainable synthetic assessment between solid-state metathesis and sonochemically derived electrocatalysts (strontium molybdate) for the precise anti-androgen BIC (CasodexTM) detection. *Microchem. J.* **168**, 106465 (2021).

52. Bonfilio, R., de Araújo, M. B. and Salgado, H. R. N. Recent applications of analytical techniques for quantitative pharmaceutical analysis: A review. *WSEAS Trans. Biol. Biomed.* **7**, 316–338 (2010).

53. Redasani, V.K., Patel, P.R., Marathe, D.Y., Chaudhari, S.R., Shirkhedkar, A.A. and Surana, S.J. A review on derivative uv-spectrophotometry analysis of drugs in pharmaceutical formulations and biological samples review. *J. Chil. Chem. Soc.* **63**, 4126–4134 (2018).

54. Lucas, M. S., Peres, J. A. and Li Puma, G. Advanced oxidation processes for water and wastewater treatment. *Water (Switzerland)* **13**, 1–24 (2021).

55. Pape, M. Industrial applications of photochemistry. *Pure Appl. Chem.* **41**, 535–558 (1975).

56. Hatrík Š. Extraction methodology and chromatography for the determination of residual pesticides in water. *J. Chromatogr. A.* **733**, 217-33 (1996).

57. Fuchs, B., Schiller, J., Süß, R., Nimptsch, A., Schürenberg, M. and Suckau, D. Capabilities and disadvantages of combined matrix-assisted laser-desorption/ionization time-of-flight mass spectrometry (MALDI-TOF MS) and high-performance thin-layer chromatography (HPTLC): Analysis of egg yolk lipids. *J. Planar Chromatogr. - Mod. TLC.* **22**, 35–42 (2009).

58. Farid, N. F. and Abdelwahab, N. S. Two different spectrophotometric determinations of potential anti-cancer drug and its toxic metabolite. *Spectrochim. Acta - Part A Mol. Biomol. Spectrosc.* **145**, 360–367 (2015).

59. Deepakumari, H. N. and Revanasiddappa, H. D. Spectrophotometric Estimation of FLU in Pure and in Pharmaceutical Preparations. *ISRN Spectrosc.* **2012**, 1– 7 (2012).

60. Smith, A. A., Manavalan, R., Kannan, K. and Rajendiran, N. Spectrofluorimetric determination of FLU in pharmaceutical preparations. *Orient. J. Chem.* **24**, 189– 194 (2008).

61. Vargas, F., Rivas, C., Méndez, H., Fuentes, A., Fraile, G. and Velásquez, M. Photochemistry and phototoxicity studies of FLU, a phototoxic anti-cancer drug. *J. Photochem. Photobiol. B Biol.* **58**, 108–114 (2000).

62. Sortino, S., Giuffrida, S., De Guidi, G., Chillemi, R., Petralia, S., Marconi, G., Condorelli, G. and Sciuto, S. The Photochemistry of FLU and its Inclusion Complex with β- Cyclodextrin. Dramatic Effect of the Microenvironment on the Nature and on the Efficiency of the Photodegradation Pathways¶. *Photochem. Photobiol.* **73**, 6 (2001).

63. Udagawa, C., Fukuyoshi, S., Morimoto, S., Tanimoto, Y. and Nakagaki, R. Photochemistry of FLU in various media: Investigation of the reaction mechanism as revealed by external magnetic field effects on product yields. *J. Photochem. Photobiol. A Chem.* **226**, 57–63 (2011).

64. Ensafi, A. A., Farfani, N. K., Amini, M. and Rezaei, B. Developing a sensitive DNA biosensor for the detection of FLU using electrochemical method. *J. Iran. Chem. Soc.* **14**, 1325–1334 (2017).

65. Suvina, V., Kokulnathan, T., Wang, T. J. and Balakrishna, R. G. Unraveling thelectrochemical properties of lanthanum cobaltite decorated halloysite nanotube nanocomposite: An advanced electrocatalyst for determination of FLU in environmental samples. *Ecotoxicol. Environ. Saf.* **190**, 110098 (2020).

66. Kubendhiran, S., Sakthivel, R., Chen, S. M., Mutharani, B. and Chen, T. W. Innovative Strategy Based on a Novel Carbon-Black-β-Cyclodextrin Nanocomposite for the Simultaneous Determination of the Anti-cancer Drug FLU and the Environmental Pollutant 4-Nitrophenol. *Anal. Chem.* **90**, 6283–6291 (2018).

67. Snycerski A. Polarographic determination of flutamide. *J. Pharm. Biomed.* **7,** 1513-1589 (1989).

68. Álvarez-Lueje, A., Peña, C., Núñez-Vergara, L. J. and Squella, J. A. Electrochemical Study of FLU, an Anti-cancer Drug, and Its Polarographic, UV Spectrophotometric and HPLC Determination in Tablets. *Electroanalysis* **10**, 1043–1051 (1998).

69. Smith, A. A., Manavalan, R., Kannan, K. and Rajendiran, N. Spectrofluorimetric determination of BIC in formulation and biological fluids. *Asian J. Chem.* **21**, 459–466 (2009).

70. Ray, S., Ghosh (Ray), S. and Mandal, S. Development of BIC-loaded PLGA NPs: preparation, characterisation and in-vitro evaluation for the treatment of prostate cancer. *Artif. Cells, Nanomedicine Biotechnol.* **45**, 944–954 (2017).

71. SAVCI, S. Photochemistry of Three Selected PCs in Seawater and River Water. *Int. J. Nat. Sci. Res.* **3**, 1–8 (2015).

72. Gomes, F. P. and Garcia, P. L. Development and validation of a simple and sensitive high-performance liquid chromatographic method for the simultaneous determination of anastrozole, Bicalutamide, tamoxifen, and their synthetic impurities. *Talanta.* **101**, 495–503 (2012).

73. Pandit, U. J., Khan, I., Wankar, S., Raj, K. K. and Limaye, S. N. Development of an electrochemical method for the determination of BIC at the SWCNT/CPE in pharmaceutical preparations and human biological fluids. *Anal. Methods* **7**, 10192–10198 (2015).

74. Niopas, I. and Daftsios, A. C. Determination of 2-OHF in human plasma by high- performance liquid chromatography and its application to pharmacokinetic studies. *J. Chromatogr. B Biomed. Sci. Appl.* **759**, 179–183 (2001).

75. Leibinger, J. and Kapás, M. New and validated high-performance liquid chromatographic method for determination of OHF in human plasma. *J. Pharm. Biomed. Anal.* **14**, 1377–1381 (1996).

76. Zheng, H., Wu, D., Qian, Z. yu and Xiang, Y. Determination of 2-OHF in human plasma by liquid chromatography-tandem mass spectrometry (LC-MS/MS): Application to a bioequivalence study on Chinese volunteers. *J. Chromatogr. B Anal. Technol. Biomed. Life Sci.* **878**, 1611–1615 (2010).

77. Liu, L., Song, J. feng, Yu, P. fei and Cui, B. A novel electrochemical sensing system for inosine and its application for inosine determination in PCs and human serum. *Electrochem. commun.* **8**, 1521–1526 (2006).

78. Afzali, M., Mostafavi, A. and Shamspur, T. Square wave voltammetric determination of anti-cancer drug FLU using carbon paste electrode modified by CuO/GO/PANI nanocomposite. *Arab. J. Chem.* **13**, 3255–3265 (2020).

79. Umesh, N.M., Jesila, J.A., Wang, S.F., Govindasamy, M., Alshgari, R.A., Ouladsmane, M. and Asharani, I.V. Fabrication of highly sensitive anti-cancer drug sensor based on heterostructured ZnO-Co3O4 capped on carbon nitride nanomaterials. *Microchem. J.* **167**, 106244 (2021).

80. Venkatesh, K. *et al.* Nanomolar level detection of non-steroidal antiandrogen drug FLU based on ZnMn2O4 NPs decorated porous reduced graphene oxide nanocomposite electrode. *J. Hazard. Mater.* **405**, 124096 (2021).

81. Sharma, T. S. K. and Hwa, K. Y. Rational design and preparation of copper vanadate anchored on sulfur doped reduced graphene oxide nanocomposite

for electrochemical sensing of antiandrogen drug nilutamide using flexible electrodes. *J. Hazard. Mater.* **410**, 124659 (2021).

82. Kesavan, G. and Chen, S. M. Highly sensitive manganese oxide/hexagonal boron nitride nanocomposite: An efficient electrocatalyst for the detection of anti- cancer drug FLU. *Microchem. J.* **163**, 105906 (2021).

83. Sundar, S., Venkatachalam, G. and Kwon, S. J. Biosynthesis of copper oxide(Cuo) nanowires and their use for the electrochemical sensing of dopamine. *Nanomaterials.* **8**, 1–19 (2018).

84. Kuang, Q., Wang, X., Jiang, Z., Xie, Z. and Zheng, L. High-energy-surface engineered metal oxide micro- and nanocrystallites and their applications. *Acc. Chem. Res.* **47**, 308–318 (2014).

85. Mallakpour, S. and Madani, M. A review of current coupling agents for modification of MONPs. *Prog. Org. Coatings.* **86**, 194–207 (2015).

86. Oelerich, W., Klassen, T. and Bormann, R. Metal oxides as catalysts for improved hydrogen sorption in nanocrystalline Mg-based materials. *J. Alloys Compd.* **315**, 237–242 (2001).

87. Lin, X., Zhang, Z., Zhang, Z., Sun, J., Wang, Q. and Pittman, C.U. Catalytic fast pyrolysis of a wood-plastic composite with metal oxides as catalysts. *Waste Manag.* **79**, 38–47 (2018).

88. Jiang, J., Li, Y., Liu, J., Huang, X., Yuan, C. and Lou, X.W. Recent advances in metal oxide-based electrode architecture design for electrochemical energy storage. *Adv. Mater.* **24**, 5166–5180 (2012).

89. Wu, Z.S., Zhou, G., Yin, L.C., Ren, W., Li, F. and Cheng, H.M. Graphene/metal oxide composite electrode materials for energy storage. *Nano Energy* **1**, 107–131 (2012).

90. Raizada, P., Soni, V., Kumar, A., Singh, P., Khan, A.A.P., Asiri, A.M., Thakur, V.K. and Nguyen, V.H. *Surface defect engineering of metal oxides photocatalyst for energy application and water treatment*. *J. Materiomics.* **7**, 388-3418 (2021).

91. Yang, S. Y., Vecitis, C. D. and Park, H. Electrocatalytic water treatment using carbon nanotube filters modified with metal oxides. *Environ. Sci. Pollut. Res.* **26**, 1036–1043 (2019).

92. Garcia, C. V., Shin, G. H. and Kim, J. T. Metal oxide-based nanocomposites in food packaging: Applications, migration, and regulations. *Trends Food Sci. Technol.* **82**, 21–31 (2018).

93. Nikolic, M. V., Vasiljevic, Z. Z., Auger, S. and Vidic, J. MONPs for safe active and intelligent food packaging. *Trends Food Sci. Technol.* **116**, 655–668 (2021).

94. Hendraningrat, L. and Torsæter, O. Metal oxide-based NPs: revealing their potential to enhance oil recovery in different wettability systems. *Appl. Nanosci.* **5**, 181–199 (2015).

95. Vittoz, C., Mantel, M. and Joud, J. C. Wettability of Metallic Oxides - Application to Stainless Stell Acid-Base Properties. *J. Adhes.* **67**, 347–358 (1998).

96. Liu, S., Ho, S., Chen, Y. and So, F. Passivation of metal oxide surfaces for high- performance organic and hybrid optoelectronic devices. *Chem. Mater.* **27**, 2532–2539 (2015).

97. Zhang, Y., Liu, Z., Ji, C., Chen, X., Hou, G., Li, Y., Zhou, X., Cui, X., Yang, X., Ren, C. and Liu, D. Low-Temperature Oxide/Metal/Oxide Multilayer Films as Highly Transparent Conductive Electrodes for Optoelectronic Devices. *ACS Appl. Energy Mater.* **4**, 6553–6561 (2021).

98. Flores, E., Novák, P. and Berg, E. J. In-situ and Operando Raman spectroscopy of layered transition metal oxides for Li-ion battery cathodes. *Front. Energy Res.* **6**, 1–16 (2018).

99. Charles, N., Yu, Y., Giordano, L., Jung, R., Maglia, F. and Shao-Horn, Y. Toward Establishing Electronic and Phononic Signatures of Reversible Lattice Oxygen Oxidation in Lithium Transition Metal Oxides for Li- Ion Batteries. *Chem. Mater.* **32**, 5502–5514 (2020).

100. Greiner, M. T. and Lu, Z. H. Thin-film metal oxides in organic semiconductor devices: Their electronic structures, work functions and interfaces. *NPG Asia Mater.* **5**, 1–16 (2013).

101. Jo, J. W., Kang, S. H., Heo, J. S., Kim, Y. H. and Park, S. K. Flexible Metal Oxide Semiconductor Devices Made by Solution Methods. *Chem. - A Eur. J.* **26**, 9126– 9156 (2020).

102. Iravani, S. and Varma, R.S. Sustainable synthesis of cobalt and cobalt oxide nanoparticles and their catalytic and biomedical applications. *Green Chem*, **22**, 2643-2661 (2020).

103. Wang, Y., Wang, L. and Zhuang, Q. A ratiometric electrochemical sensor for dopamine detection based on hierarchical manganese dioxide nanoflower/multi- walled carbon nanotube nanocomposite modified glassy carbon electrode. *J. Alloys Compd.* **802**, 326–334 (2019).

104. Wang, M.Y., Zhu, W., Ma, L., Ma, J.J., Zhang, D.E., Tong, Z.W. and Chen, J. Enhanced simultaneous detection of ractopamine and salbutamol - Via electrochemical-facial deposition of MnO2 nanoflowers onto 3D RGO/Ni foam templates. *Biosens. Bioelectron.* **78**, 259–266 (2016).

105. Kung, C. W., Lin, C. Y., Lai, Y. H., Vittal, R. and Ho, K. C. Cobalt oxide acicular nanorods with high sensitivity for the non-enzymatic detection of glucose. *Biosens. Bioelectron.* **27**, 125–131 (2011).

106. Wang, T., Xi, L. and Wang, J. In-situ fabrication of cobalt nanoflowers on sulfonated and fluorinated poly (arylene ether ketone-benzimidazole) template film for the electrocatalytic oxidation of glucose. *Talanta* **178**, 481–490 (2018).

107. Han, D., Ji, Y., Gu, F. and Wang, Z. Cobalt oxide nanorods with special pore structure for enhanced ethanol sensing performance. *J. Colloid Interface Sci.* **531**, 320–330 (2018).

108. Mehrabi, A., Rahimnejad, M., Mohammadi, M. and Pourali, M. Electrochemical detection of FLU with gold electrode as an anti-cancer drug. *Biocatal. Agric. Biotechnol.* **22**, 101375 (2019).

109. Tseng, T.W., Rajaji, U., Chen, T.W., Chen, S.M., Huang, Y.C., Mani, V. and Jothi, A.I.Sonochemical synthesis and fabrication of perovskite type calcium titanate interfacial nanostructure supported on graphene oxide sheets as a highly efficient electrocatalyst for electrochemical detection of chemotherapeutic drug. *Ultrason. Sonochem.* **69**, 105242 (2020).

110. Al-Alawy, A.F., Al-Abodi, E.E. and Kadhim, R.M. Synthesis and characterization of magnetic iron oxide nanoparticles by co-precipitation method at different conditions. J. Eng. 24, 60-72 (2018).

111. Parashar, M., Shukla, V. K. and Singh, R. Metal oxides NPs via sol-gel method: a review on synthesis, characterisation and applications. *J. Mater. Sci. Mater. Electron.* **31**, 3729–3749 (2020).

112. Narita, A., Naka, K. and Chujo, Y. Facile control of silica shell layer thickness on hydrophilic iron-oxide NPs via reverse micelle method. *Colloids Surfaces A Physicochem. Eng. Asp.* **336**, 46–56 (2009).

113. Hufschmid, R., Arami, H., Ferguson, R.M., Gonzales, M., Teeman, E., Brush, L.N., Browning, N.D. and Krishnan, K.M. Synthesis of phase-pure and monodisperse iron-oxide NPs by thermal decomposition. *Nanoscale.* **7**, 11142–11154 (2015).

114. Ge, S., Shi, X., Sun, K., Li, C., Uher, C., Baker Jr, J.R., Banaszak Holl, M.M. and Orr, B.G. Facile hydrothermal synthesis of iron-oxide NPs with tunable magnetic properties. *J. Phys. Chem. C.* **113**, 13593–13599 (2009).

115. Wang, S., Jiang, S. P. and Wang, X. Microwave-assisted one-pot synthesis of metal/MONPs on graphene and their electrochemical applications. *Electrochim. Acta* **56**, 3338–3344 (2011).

116. Tazikeh, S., Akbari, A., Talebi, A. and Talebi, E. Synthesis and characterisation of tin oxide NPs via the Co-precipitation method. *Mater. Sci. Pol.* **32**, 98–101 (2014).

117. Nabiyouni, Masoumi, S., Nabiyouni, G. and Ghanbari, D. Photo-degradation of Congored, acid brown and acid violet: photo catalyst and magnetic

investigation of $CuFe_2O_4$–TiO_2–Ag nanocomposites. *J. Mater. Sci. Mater. Electron.* **27**, 11017-11033 (2016).

118. Ramadoss, A., Krishnamoorthy, K. and Kim, S. J. Novel synthesis of hafnium oxide NPs by precipitation method and its characterisation. *Mater. Res. Bull.* **47**, 2680–2684 (2012).

119. Hussain, M., Sun, H., Karim, S., Nisar, A., Khan, M., Ul Haq, A., Iqbal, M. and Ahmad, M. Noble metal nanoparticle-functionalized ZnO nanoflowers for photocatalytic degradation of RhB dye and electrochemical sensing of hydrogen peroxide. *J. Nanoparticle Res.* **18**, 1–14 (2016).

120. Kandpal, N. D., Sah, N., Loshali, R., Joshi, R. and Prasad, J. Co-precipitation method of synthesis and characterisation of iron-oxide NPs. *J. Sci. Ind. Res. (India).* **73**, 87–90 (2014).

121. Luna, I.Z. and Bangladesh Atomic Energy Commission. Preparation and Characterisation of Copper Oxide NPs Synthesised via Chemical Precipitation Method. *OALib.* **02**, 1–8 (2015).

122. Janjua, M. R. S. A. Synthesis of Co3O4 Nano Aggregates by Co-precipitation Method and its Catalytic and Fuel Additive Applications. *Open Chem.* **17**, 865–873 (2019).

123. Senthilkumar, V., Vickraman, P. and Ravikumar, R. Synthesis of fluorine doped tin oxide NPs by sol-gel technique and their characterisation. *J. Sol-Gel Sci. Technol.* **53**, 316–321 (2010).

124. Danial, A. S., Saleh, M. M., Salih, S. A. and Awad, M. I. On the synthesis of nickel oxide NPs by sol-gel technique and its electrocatalytic oxidation of glucose. *J. Power Sources* **293**, 101–108 (2015).

125. Ismail, A.M., Menazea, A.A., Kabary, H.A., El-Sherbiny, A.E. and Samy, A. The influence of calcination temperature on structural and antimicrobial characteristics of zinc oxide nanoparticles synthesized by Sol–Gel method. *J. Mol. Struct.* **1196**, 332-337 (2019).

126. Wahab, R., Ansari, S. G., Dar, M. A., Kim, Y. S. and Shin, H. S. Synthesis of Magnesium Oxide NPs by Sol-Gel Process. *Mater. Sci. Forum* **558**–**559**, 983–986 (2007).

127. Kayani, Z. N., Arshad, S., Riaz, S. and Naseem, S. Synthesis of Iron-Oxide NPs by Sol-Gel Technique and Their Characterisation. *IEEE Trans. Magn.* **50**, 9–12 (2014).

128. Paper, Alwan, R.M., Kadhim, Q.A., Sahan, K.M., Ali, R.A., Mahdi, R.J., Kassim, N.A. and Jassim, A.N. Synthesis of zinc oxide nanoparticles via sol–gel route and their characterization. *J. Nanosci. Nanotechnol*. 5, 1-6 (2015).

129. Mousavi, S. F., Davar, F. and Loghman-Estarki, M. R. Controllable synthesis of ZnO nanoflowers by the modified sol-gel method. *J. Mater. Sci. Mater. Electron.* **27**, 12985–12995 (2016).

130. Kemnitz, E. and Noack, J. The non-aqueous fluorolytic sol-gel synthesis of nanoscaled metal fluorides. *Dalt. Trans.* **44**, 19411–19431 (2015).

131. Noh, J., Yi, M., Hwang, S., Im, K.M., Yu, T. and Kim, J. A facile synthesis of rutile-rich titanium oxide NPs using reverse micelle method and their photocatalytic applications. *J. Ind. Eng. Chem.* **33**, 369–373 (2016).

132. Rani, R. Antibacterial Activity of Copper Oxide NPs Against Gram-Negative Bacterial Strain Synthesised By Reverse Micelle Technique. *Int. J. Pharm. Res. Dev.* **6**, 72–78 (2014).

133. Iida, H., Nakanishi, T., Takada, H. and Osaka, T. Preparation of magnetic iron-oxide NPs by successive reduction-oxidation in reverse micelles: Effects of reducing agent and atmosphere. *Electrochim. Acta* **52**, 292–296 (2006).

134. Ahmad, T., Ramanujachary, K. V., Lofland, S. E. and Ganguli, A. K. Magnetic and electrochemical properties of nickel oxide NPs obtained by the reverse-micellar route. *Solid State Sci.* **8**, 425–430 (2006).

135. Nair, J. S. A., Aswathi, R. and Sandhya, K. Y. Reverse micelle assisted hydrothermal reaction route for the synthesis of homogenous MoS2 nanospheres. *SN Appl. Sci.* **1**, 1–7 (2019).

136. Daengsakul, S., Mongkolkachit, C., Thomas, C., Siri, S., Thomas, I., Amornkitbamrung, V. and Maensiri, S. A simple thermal decomposition synthesis, magnetic properties, and cytotoxicity of La0.7Sr0.3MnO3 NPs. *Appl. Phys. A Mater. Sci. Process.* **96**, 691–699 (2009).

137. Salavati-Niasari, M., Mir, N. and Davar, F. A novel precursor in preparation and characterisation of nickel oxide NPs via thermal decomposition approach. *J. Alloys Compd.* **493**, 163–168 (2010).

138. Mohadesi, A., Ranjbar, M. and Hosseinpour-Mashkani, S. M. Solvent-free synthesis of mercury oxide NPs by a simple thermal decomposition method. *Superlattices Microstruct.* **66**, 48–53 (2014).

139. Hosseinpour-Mashkani, S. M. and Ramezani, M. 150. S.M. Hosseinpour-Mashkani, M. Ramezani, Silver and silver oxide NPs: Synthesis and characterisation by thermal decomposition, Materials Letters. 2014, 130, 259-262. *Mater. Lett.* **130**, 259–262 (2014).

140. Salavati-Niasari, M. and Davar, F. Synthesis of copper and copper(I) oxide NPs by thermal decomposition of a new precursor. *Mater. Lett.* **63**, 441–443 (2009).

141. Mahhouti, Z., El Moussaoui, H., Mahfoud, T., Hamedoun, M., El Marssi, M., Lahmar, A., El Kenz, A. and Benyoussef, A. Chemical synthesis and magnetic properties of monodisperse cobalt ferrite NPs. *J. Mater. Sci. Mater. Electron.* **30**, 14913–14922 (2019).

142. Zulkifli, Z. A., Razak, K. A., Rahman, W. N. W. A. and Abidin, S. Z. Synthesis and Characterisation of Bismuth Oxide NPs using Hydrothermal Method: The Effect of Reactant Concentrations and application in radiotherapy. *J. Phys. Conf. Ser.* **1082**, 1–7 (2018).

143. Sundrarajan, M., Bama, K., Bhavani, M., Jegatheeswaran, S., Ambika, S., Sangili, A., Nithya, P. and Sumathi, R. Obtaining titanium dioxide NPs with spherical shape and antimicrobial properties using M. citrifolia leaves extract by hydrothermal method. *J. Photochem. Photobiol. B Biol.* **171**, 117–124 (2017).

144. Transactions, C. S., Babu, K. S., Narayanan, V. and Campus, G. Hydrothermal Synthesis of Hydrated Zinc Oxide NPs and its Characterisation†. *Chem. Sci. Trans.* **2**, 33–36 (2013).

145. Arun, K.J., Batra, A.K., Krishna, A., Bhat, K., Aggarwal, M.D. and Francis, P.J.Surfactant Free Hydrothermal Synthesis of Copper Oxide NPs. *Am. J. Mater. Sci.* **5**, 36–38 (2015).

146. Viet, P. Van, Thi, C. M. and Hieu, L. Van. The High Photocatalytic Activity of SnO2 NPs Synthesised by Hydrothermal Method. *J. Nanomater.* **2016**, (2016).

147. Akhoon, S. A., Rubab, S. and Shah, M. A. A benign hydrothermal synthesis of nanopencils-like zinc oxide nanoflowers. *Int. Nano Lett.* **5**, 9–13 (2015).

148. Ohara, S., Mousavand, T., Sasaki, T., Umetsu, M., Naka, T. and Adschiri, T. Continuous production of fine zinc oxide nanorods by hydrothermal synthesis in supercritical water. *J. Mater. Sci.* **43**, 2393–2396 (2008).

149. Veeralingam, S. and Badhulika, S. Two-Dimensional Metallic NiSe2 Nanoclusters–Based Low-Cost, Flexible, Amperometric Sensor for Detection of Neurological Drug Carbamazepine in Human Sweat Samples. *Front. Chem.* **8**, 337 (2020).

150. Thamima, M. and Karuppuchamy, S. Microwave-assisted synthesis of Zinc oxide NPs. *Int. J. ChemTech Res.* **8**, 250–256 (2015).

151. Palchik, O., Zhu, J. and Gedanken, A. Microwave-assisted preparation of binary oxide NPs. *J. Mater. Chem.* **10**, 1251–1254 (2000).

152. Krishnakumar, T., Pinna, N., Kumari, K. P., Perumal, K. and Jayaprakash, R. Microwave-assisted synthesis and characterisation of tin oxide NPs. *Mater. Lett.* **62**, 3437–3440 (2008).

153. Bhatt, A. S., Bhat, D. K., Tai, C. W. and Santosh, M. S. Microwave-assisted synthesis and magnetic studies of cobalt oxide NPs. *Mater. Chem. Phys.* **125**, 347–350 (2011).

154. Mohammadyani, D., Hosseini, S. A. and Sadrnezhaad, S. K. Characterisation of Nickel Oxide NPs Synthesised Via Rapid Microwave-Assisted Route. *Int. J. Mod. Phys. Conf. Ser.* **05**, 270–276 (2012).

155. Lin, Y. H. and Yeh, Y. C. Rapid synthesis of microwave-assisted zinc oxide nanorods on a paper-based analytical device for fluorometric detection of L-dopa. *Colloids Surfaces B Biointerfaces* **207**, 111995 (2021).

156. Fazlali, A., Moradi, S. and Hamedi, H. Studying of optimisation condition of rosemary essence extraction with microwave-assisted hydro-distillation method. *Am. J. Essent. Oils Nat. Prod.* **46**, 46–50 (2015).

157. Mohanty, U. S. Electrodeposition: A versatile and inexpensive tool for the synthesis of nanoparticles, nanorods, nanowires, and nanoclusters of metals. *J. Appl. Electrochem.* **41**, 257–270 (2011).

158. 158. Babaei-Sati, R., Basiri Parsa, J. and Vakili-Azghandi, M. Electrodeposition of polypyrrole/ metal oxide nanocomposites for corrosion protection of mild steel—A comparative study. *Synth. Met.* **247**, 183–190 (2019).

159. 159. Chou, S., Cheng, F. and Chen, J. Electrodeposition synthesis and electrochemical properties of nanostructured γ-MnO2 films. *J. Power Sources* **162**, 727–734 (2006).

160. Camacho, L. M., Torres, A., Saha, D. and Deng, S. Journal of Colloid and Interface Science Adsorption equilibrium and kinetics of fluoride on sol – gel-derived activated alumina adsorbents. *J. Colloid Interface Sci.* **349**, 307–313 (2010).

161. Mackenzie, J. D. Applications of the sol-gel process. *J. Non. Cryst. Solids* **100**, 162–168 (1988).

162. Muromachi, T., Tsujino, T., Kamitani, K. and Maeda, K. Application of functional coatings by sol-gel method. *J. Sol-Gel Sci. Technol.* **40**, 267–272 (2006).

163. Lee, Y., Lee, J., Bae, C.J., Park, J.G., Noh, H.J., Park, J.H. and Hyeon, T. Large-scale synthesis of uniform and crystalline magnetite NPs using reverse micelles as nanoreactors under reflux conditions. *Adv. Funct. Mater.* **15**, 503–509 (2005).

164. Jamkhande, P. G., Ghule, N. W., Bamer, A. H. and Kalaskar, M. G. Metal NPs synthesis: An overview on methods of preparation, advantages and disadvantages, and applications. *J. Drug Deliv. Sci. Technol.* **53**, 101174 (2019).

165. Gan, Y. X., Jayatissa, A. H., Yu, Z., Chen, X. and Li, M. Hydrothermal Synthesis of Nanomaterials. *J. Nanomater.* **2020**, 1 (2020).

166. Kurbanoglu, S. and Ozkan, S. A. Electrochemical carbon based nanosensors: A promising tool in pharmaceutical and biomedical analysis. *J. Pharm. Biomed. Anal.* **147**, 439–457 (2018).

167. Liu, Y., Ji, X. and He, Z. Organic-inorganic nanoflowers: From design strategy to biomedical applications. *Nanoscale* **11**, 17179–17194 (2019).

168. Manno, D., Filippo, E., Di Giulio, M. and Serra, A. Synthesis and characterisation of starch-stabilized Ag nanostructures for sensors applications. *J. Non. Cryst. Solids* **354**, 5515–5520 (2008).

169. Calabrese, C., Aprile, C., Gruttadauria, M. and Giacalone, F. POSS nanostructures in catalysis. *Catal. Sci. Technol.* **10**, 7415–7447 (2020).

170. Reddy, A. L. M., Gowda, S. R., Shaijumon, M. M. and Ajayan, P. M. Hybrid nanostructures for energy storage applications. *Adv. Mater.* **24**, 5045–5064 (2012).

171. Wang, J., Li, Y. and Nie, G. Multi-functional biomolecule nanostructures for cancer therapy. *Nat. Rev. Mater.* **6**, 766–783 (2021).

172. Mathur, D. and Medintz, I. L. The Growing Development of DNA Nanostructures for Potential Healthcare-Related Applications. *Adv. Healthc. Mater.* **8**, 1801546 (2019).

173. Ali, N. M. and Rafat, N. H. Modeling and simulation of nanorods photovoltaic solar cells_ A review. *Renew. Sustain. Energy Rev.* **68**, 212–220 (2017).

174. Marangoni, V. S., Cancino-bernardi, J. and Zucolotto, V. Biomedical Applications of Gold Nanorods — A Review. **12**, 1136-1158 (2016).

175. Cao, A.M., Hu, J.S., Liang, H.P. and Wan, L.J. Self-assembled vanadium pentoxide (V_2O_5) hollow microspheres from nanorods and their application in lithium-Ion batteries. *Angew. Chem. Int. Ed*, **44**, 4391-4395 (2005).

176. Alekseeva, Anna V., Vladimir A. Bogatyrev, Lev A. Dykman, Boris N. Khlebtsov, Lyubov A. Trachuk, Andrei G. Melnikov, and Nikolai G. Khlebtsov. Preparation and optical scattering characterization of gold nanorods and their application to a dot-immunogold assay. *Applied optics*. **44**, 6285-6295 (2005).

177. Rahmani, S., Durand, J., Charnay, C. and Lichon, L. Synthesis of mesoporous silica NPs and nanorods: Application to doxorubicin delivery. Solid State Sci **68**, 25–31 (2017).

178. Rodrigues, C.F., Jacinto, T.A., Moreira, A.F., Costa, E.C., Miguel, S.P. and Correia, I.J. Functionalization of AuMSS nanorods towards more effective cancer therapies. *Nano Research.* **12**, 719–732 (2019).

179. Qie, L., Chen, W., Xu, H., Xiong, X., Jiang, Y., Zou, F., Hu, X., Xin, Y., Zhang, Z. and Huang, Y. Synthesis of functionalized 3D hierarchical porous carbon for high-performance supercapacitors. *Energy Environ. Sci.* **6**, 2497–2504 (2013).

180. Suni, I. I. Impedance methods for electrochemical sensors using nanomaterials. Trends Analyt. Chem. **27**, 604-611 (2008).

181. Jia, X., Dong, S. and Wang, E. Biosensors and Bioelectronics Engineering the bioelectrochemical interface using functional nanomaterials and microchip technique toward sensitive and portable electrochemical biosensors. *Biosens. Bioelectron.* **76**, 80–90 (2016).

182. Khan, F.S.A., Mubarak, N.M., Khalid, M., Walvekar, R., Abdullah, E.C., Ahmad, A., Karri, R.R. and Pakalapati, H. Functionalized Multi-walled Carbon Nanotube Electrochemical Sensor for Determination of Anti-cancer Drug Flutamide. *Scientific reports.* **46**, 5619– 5628 (2017).

183. Ding, Y., Ma, H., Xu, Y., Yang, F., Li, Y., Shi, F. and Lu, Y. Potentiation of Flutamide-induced hepatotoxicity in mice by Xian-Ling- Gu-Bao through induction of CYP1A2. *J. Ethnopharmacol.* **278**, 114299 (2021).

184. Brahman, P.K., Suresh, L., Reddy, K.R. and Bondili, J.S. An electrochemical sensing platform for trace recognition and detection of an anti-prostate cancer drug flutamide in biological samples. *RSC advances*. 7, 37898-37907 (2017).

185. Trinadh, T., Khuntia, H., Anusha, T., Bhavani, K.S., Kumar, J.S. and Brahman, P.K. Diamond and Related Materials Synthesis and characterisation of nanocomposite material based on graphene quantum dots and lanthanum doped zirconia NPs : An electrochemical sensing application towards FLU in urine samples. *Diam. Relat. Mater.* **110**, 108143 (2020).

186. Karthik, R., Govindasamy, M., Chen, S.M., Chen, T.W., Elangovan, A., Muthuraj, V. and Yu, M.C. A facile graphene oxide-based sensor for electrochemical detection of prostate anti-cancer (anti-testosterone) drug FLU in biological samples. *RSC Adv.* **7**, 25702–25709 (2017).

187. Ensafi, A. A., Talkhooncheh, M., Zandi-atashbar, N. and Rezaei, B. Electrochemical Sensing of FLU Contained in Plasma and Urine Matrices Using NiFe 2 O 4 / rGO Nanocomposite, as an Efficient and Selective Electrocatalyst *electrocatalyst.* **32**, 1717-1724 (2020).

188. Wellington, K. and Keam, S. J. Bicalutamide 150mg Prostate Cancer*. J. Ethnopharmacol.* **66**, 837–850 (2006).-

189. Cockshott, I. D. Clinical Pharmacokinetics and Metabolism. *Expert Opin. Drug Metab. Toxicol.* **43**, 855–878 (2004).

190. Nguyen, P.L., Alibhai, S.M., Basaria, S., D'Amico, A.V., Kantoff, P.W., Keating, N.L., Penson, D.F., Rosario, D.J., Tombal, B. and Smith, M.R. Adverse effects of androgen deprivation therapy and strategies to mitigate them. *Eur. Urol.* **67**, 825-836 (2015).

191. Gretarsdottir, H. M., Bjornsdottir, E. and Bjornsson, E. S. BIC-Associated Acute Liver Injury and Migratory Arthralgia: A Rare but Clinically Important Adverse Effect. *Case Reports in Gastroenterology.* **12**, 266–270 (2018).

192. Chojnacka, K., Zarzycka, M., Hejmej, A., Mruk, D.D., Gorowska, E., Kotula-Balak, M., Klimek, M. and Bilinska, B. Toxicology in-Vitro Hydroxyflutamide affects connexin 43 via the activation of PI3K / Akt-dependent pathway but has

no effect on the crosstalk between PI3K / Akt and ERK1 / 2 pathways at the Raf-1 kinase level in primary rat Sertoli cells. *TIV.* **31**, 146–157 (2016).

193. Khan, N., Abdelhamid, H. N., Yan, J. Y., Chung, F. T. and Wu, H. F. Detection of FLU in pharmaceutical dosage using higher electrospray ionization mass spectrometry (ESI-MS) tandem mass coupled with Soxhlet apparatus. *Anal. Chem. Res.* **3**, 89–97 (2015).

CHAPTER 3

METHODOLOGY

3. Experimental

3.1. Materials

3.1.1. Solvents and chemicals

Phosphate buffer solution (PBS) was prepared using sodium phosphate dibasic (Na_2HPO_4) and sodium phosphate monobasic (NaH_2PO_4) solutions and was used as a pH buffering agent. Sodium hydroxide and hydrochloric acid were purchased from Merck. Milli-Q water was obtained from Milli-Q® Reference Water Purification System from Merck.Manganese(II) chloride, cobaltous chloride anhydrous, aluminium dihydrogen phosphate, ytterbium(III) nitrate hydrate, and 6-aminocaproic acid were purchased from Merck. FLU, OHF and BIC were purchased from Sigma-Aldrich. Potassium ferricyanide(III) ($K_3Fe_3(CN)_6$), potassium hexacyanoferrate(II) ($K_4Fe(CN)_6$) and potassium chloride boixtra (KCl) were purchased from Merck.

All chemicals used in this study were of analytical grade, and all solutions were prepared with milliQ Water.

3.2. Equipment

3.2.1. Ultraviolet-Visible absorption spectrometer

The optical properties of the as-prepared nanomaterials were studied using Ultraviolet-Visible absorption (UV-Vis) spectroscopy. The properties were determined using a PerkinElmer Lambda 650 UV-Vis spectrophotometer. For analysis, 1 mg of the as-prepared powders were dissolved in 2000 µL DMF to form solutions. The solutions were then transferred to a quartz cuvette and analysed at a wavelength range of 250 to 800 nm starting with the background run. The samples were analysed at room temperature. The setup used for these experiments is shown in Fig. **3.1**.

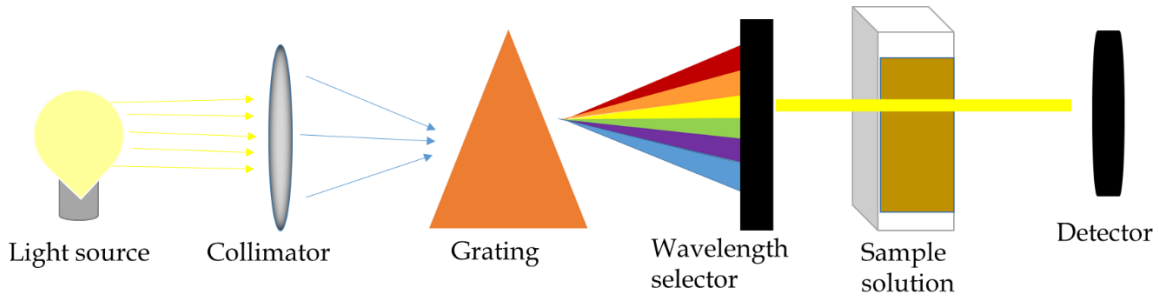

Fig. 3.1: Set up scheme of UV-Vis measurement

3.2.2. Fourier transform infrared spectrometer

The functional groups of the bonding entities on the as-prepared materials were determined in powder form using a Perkin Elmer Fourier transform infrared (FTIR) spectrometer frontier equipped with a universal attenuated total reflectance (ATR) accessory. At room temperature, the spectra were acquired at a wavelength range between 500 to 4000 cm^{-1}. During analysis, the background scan was performed first, followed by placing the dry samples on the instrument. The samples were then scanned 500 to 4000 cm^{-1} wavenumbers at a resolution of 4 cm^{-1}. The layout used for these experiments is shown in Fig. **3.2**.

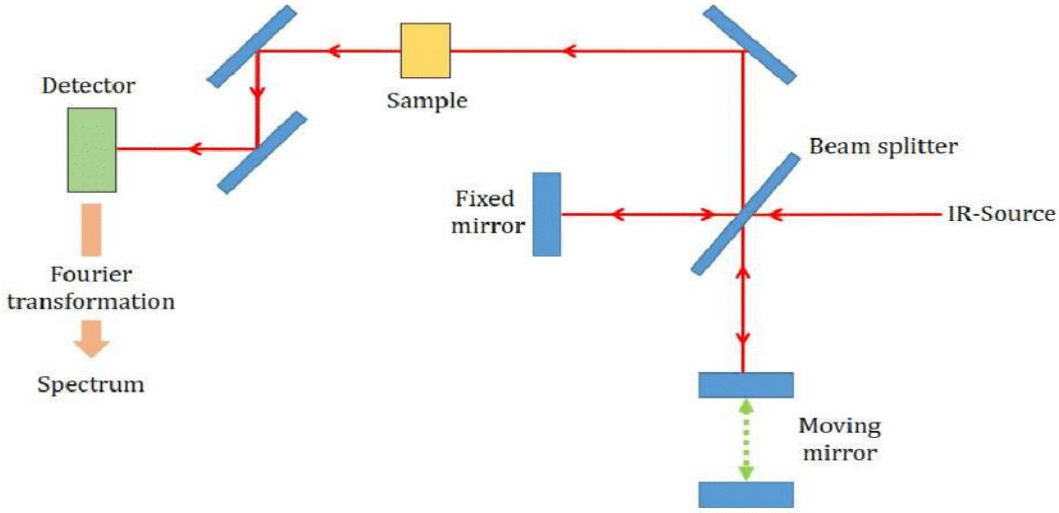

Fig. 3.2: FTIR spectrometer schematic diagram (adapted from *ref* [1])

3.2.3. X-Ray Diffraction (XRD)

The phases present in the crystalline composition of the as-prepared materials were established on a Rigaku SmartLab X-ray diffractometer with Cu Kα (λ = 0.154059 nm) radiation at 2°/min. A glass substrate sample holder was filled with powders of the as-prepared materials to analyse the samples and placed in the instrument. The samples

were then analysed from 10 - 80 2Θ. The set up used for these experiments is depicted in **Fig. 3.3**

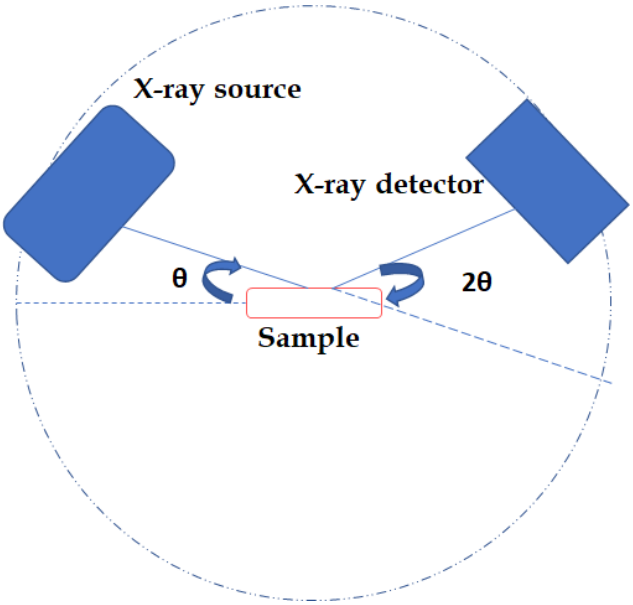

Fig. 3.3: XRD analysis schematic diagram

3.2.4. Scanning electron microscope

The surface morphologies of the synthesised materials were examined using SEM-JEOL (Japan) equipped with Oxford (UK) EDS. To analyse the samples, portions of the as-prepared powders were dissolved in DMF and dropped on a glass substrate. The glass substrate was then coated with gold and placed in the sample holder. The sample holder was then placed in the instrument, and the samples were analysed. The setup used for these experiments is shown in **Fig. 3.4**.

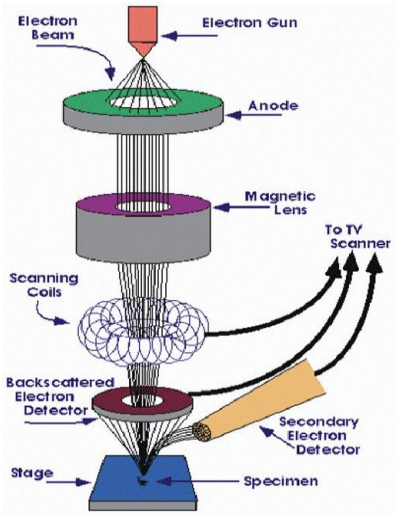

Fig. 3.4: SEM analysis schematic diagram (adapted from *ref* [2])

3.2.6 Energy-Dispersive X-Ray Analysis

The samples used to analyse the surface morphologies with SEM were used for elemental analysis on the surface of the as-prepared nanomaterials to acquire Energy-dispersive X-ray spectra (EDX) using a SEM-JOEL (Japan) equipped with Oxford (UK) EDS. Here, the SEM images are analysed using EDS to study the chemical compositions of the materials with the setup shown in Fig. **3.5**.

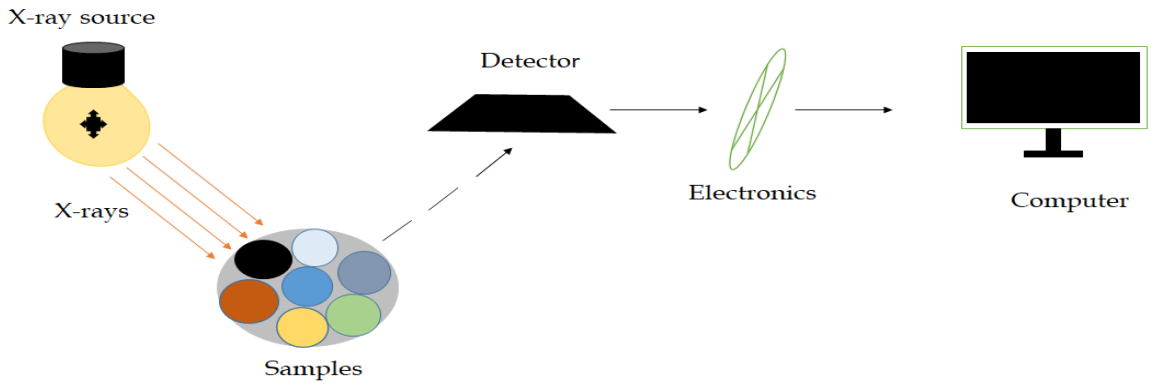

Fig. 3.5: EDX schematic diagram

3.2.7. Transmission electron microscope

The surface morphologies of the as-prepared materials were analysed using a transmission electron microscope (TEM). Portions of the materials were dissolved in DMF. The solutions were then dropped on a copper grid and left to dry for some time. The samples were then analysed after drying. The setup used for these experiments is shown in Fig. **3.6**.

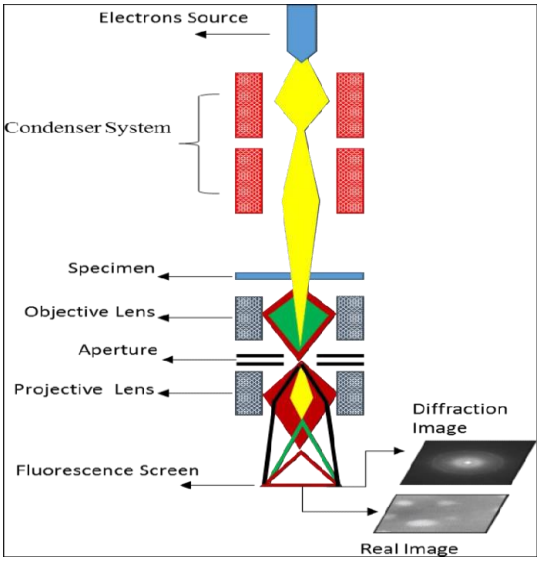

Fig. 3.6: TEM analysis schematic diagrams (adapted from *ref* [3])

3.2.8. Electrochemical equipment

Electrochemical methods are a class of analytical methods that detect analytes based on the current, potential, or resistance measurement in an electrochemical cell consisting of a reference electrode, a working electrode, and counter electrode. These methods are widely explored because they are fast, precise, and affordable detection methods. Furthermore, electrochemical methods can obtain a large number of experimental parameters that are useful in the quantification of target analytes[4]. In addition, electrochemical methods offer a variety of methods for the analysis of analytes. The methods include coulometry, amperometry, cyclic voltammetry (CV), linear sweep voltammetry (LSV), differential pulse voltammetry (DPV), anodic/cathodic stripping voltammetry (ASV/CSV), square wave voltammetry (SWV), chronoamperometry, and electrochemical impedance spectroscopy (EIS)[5,6]. Among the electrochemical methods, CV is a multipurpose technique used in the analysis of redox status in different industrial and research settings. The technique measures the current response to sweeping voltage potential applied to the sample through the working electrode. Besides being used in the determination of the analyte concentration, CV is widely used to characterize the electrochemical processes[7,8]. In addition, SWV is the most widely used electrochemical method along with SWV because they the most sensitive among all the voltammetric techniques. SWV is performed by pulsing the potential of the working electrode between two selected values instead of sweeping the potentials as is the case of CV[4]. In this study CV was

chosen because it is good for characterization of electrochemical processes and that it gives two processes (reduction and oxidation) on one scan. SWV was chosen because of its properties such as current sampling, significant time evolution between potential reversal as well as high sensitivity screening. These properties make SW advantageous over other techniques because they enable it to work at nanomolar analyte concentrations[9].

The voltammetric measurements were performed using PalmSens EmStat4M potentiostat using PSTrace software for windows. A conventional three-electrode system employing a glassy carbon electrode (GCE) (unmodified and modified) as a working electrode, platinum plate as a counter electrode and Ag|AgCl (saturated KCL) as a reference electrode was used. The setup used for these experiments is shown in Fig. **3.7**.

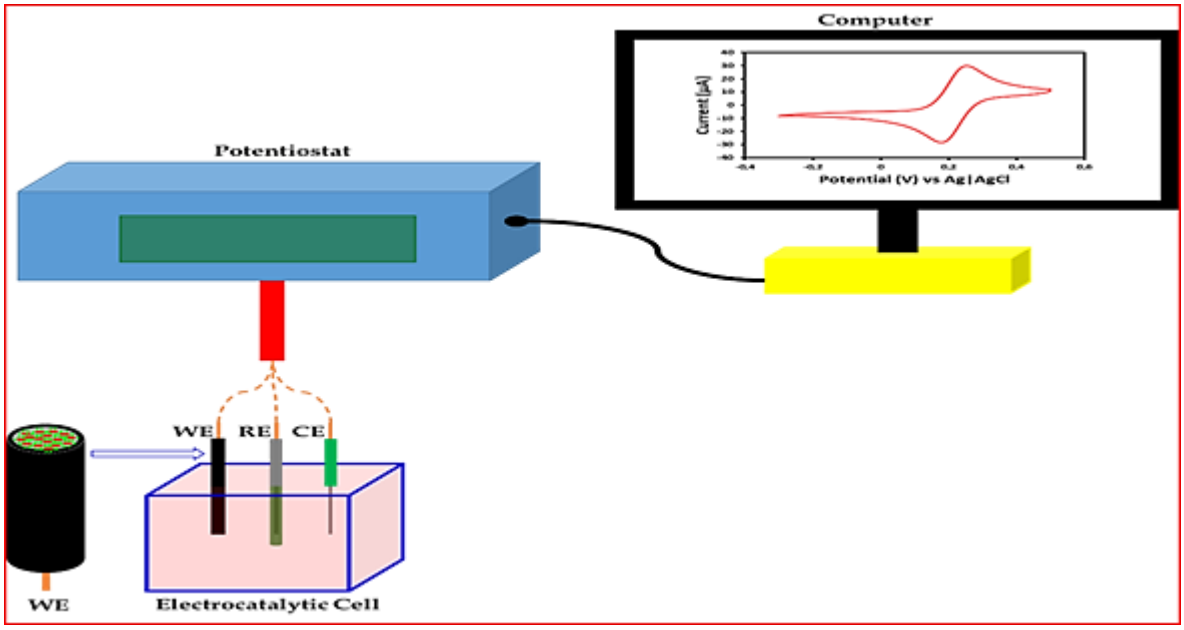

Fig. 3.7: Typical employment of nanostructure-decorated nanorods for GCE surface modification followed by drying to achieve an electrochemically active and stable platform

3.3. Synthesis of nanostructures and nanorods

3.3.1. Cobalt oxide nanostructures (CoONSs)

CoONSs were synthesised according to literature[10] with some modifications. Cobaltous chloride anhydrous (1 g; 7.70 mmol) was dissolved in milli-Q water (30 ml). Drops of sodium hydroxide solution (2M) were added to the solution to adjust the pH

to 9. The mixture was then sonicated, transferred to a stainless-steel autoclave (50 ml), and heated in an oven at 160 ˚C for 18 hours. The reaction mixture was then cooled to room temperature, centrifuged, and washed with methanol twice. The obtained product was dried in an oven at 60 ˚C and stored until further analysis. IR: [ν_{max}/cm^{-1}]: 650, 750, 840 (M-O).

3.3.2. Manganese oxide nanostructures (MnONSs)

MnONSs were prepared according to literature[10] with some modifications. Briefly, Manganese (II) chloride (1 g, 8.0 mmol) was dissolved in milli-Q water (30 ml) and ultra-sonicated for 20 min. To adjust the pH, drops of sodium hydroxide (2M) were added to the solution until the pH value was 9. The mixture was ultra-sonicated, transferred to a stainless-steel autoclave (50 ml), and placed in an oven at 160 ˚C for 18 hours. The reaction mixture was cooled to room temperature before being centrifuged and washed two times with methanol. The product was dried in an oven at 60 ˚C and stored until further analysis. IR: [ν_{max}/cm^{-1}]: 1099, 1160 (M-O).

3.3.3. Ytterbium nanorods (YbNRs)

YbNRs were synthesised using a literature method[11] with some modifications. Ytterbium(III) nitrate hydrate (300 mg, 0.80 mmol) and 6-aminocaproic acid (104.36 mg, 0.80 mmol) were dissolved in MilliQ water (10 ml). Aluminium dihydrogen phosphate solution (10 ml) was then added to the solution under magnetic stirring for 3 hours. Then, the resulting white precipitates were centrifuged and washed in methanol twice. After washing, the product was dried at 60 ˚C and stored for further analysis. IR: [ν_{max}/cm^{-1}]: 1090, 1000 (M-O).

3.4. Nanostructure-decorated ytterbium nanorods (YbNRs/MONSs)

3.4.1. Yttebium nanorods decorated with manganese oxide nanostructures (YbNRs/MnONSs)

Briefly, to obtain YbNRs decorated with MnONSs**,** manganese (II) chloride (1 g, 8.0 mmol) was dissolved in milli-Q water (30 ml) and sonicated for 20 minutes. Drops of sodium hydroxide (2M) were added to the solution to adjust the pH to 9. Powders of the as-prepared NRs (50 mg) were added to the mixture and ultra-sonicated for 20 min. The solution was then transferred to a stainless-steel autoclave (50 ml) and placed in an oven at 160 ˚C for 18 hours. The reaction mixture was cooled to room temperature before being centrifuged and washed two times with methanol. The

product was dried in an oven at 60 ˚C and stored until further analysis. IR: [ν_{max}/cm^{-1}]: 560, 650 (M-O).

3.4.2. Yttebium nanorods decorated with cobalt oxide nanostructures YbNRs/CoONSs

Here, cobaltous chloride anhydrous (1 g, 7.70 mmol) was dissolved in milli-Q water (30 ml). Drops of sodium hydroxide solution (2M) were added to the solution to adjust the pH to 9. Powders of the as-prepared nanorods (50 mg) were then added to the solution. The mixture was then sonicated, transferred to a stainless-steel autoclave (50 ml), and heated in an oven at 160 ˚C for 18 hours. The reaction mixture was then cooled to room temperature, centrifuged, and washed with methanol two times. Lastly, the product was dried in an oven at 60 ˚C and stored until further analysis. IR: [ν_{max}/cm^{-1}]: 600, 1000 (M-O).

3.5. Development of nanomaterial-modified glassy carbon electrode

3.5.1 Fabrication of metal oxide nanostructure-modified GCE

The metal oxide (MnO and CoO) nanostructure-based electrochemical sensors were developed according to the following steps. Firstly, GCE was cleaned using alumina slurry (0.3 µM) and subjected to sonication (10 min) in ethanol. The polished GCE surface was then dried at room temperature. Thereafter, the as-prepared metal oxide nanostructures (2 mg) were dissolved in dimethylformamide (DMF) (1000 µL) and sonicated for 20 min to get homogeneous MONSs solutions. MONSs solutions (10 µL) were then drop cast on the GCE surface and allowed to dry in an air oven at 60 ˚C. The obtained MONSs modified GCE surfaces were gently rinsed with DI water to remove loosely attached molecules on the GCE surface. The obtained MnO/GCE and CoO/GCE were employed for further electrochemical experiments.

3.5.2 Fabrication of ytterbium nanorod-modified GCE

To fabricate the NR-based electrochemical sensor, a few steps were used. First, a GCE was cleaned using alumina slurry (0.3 µM), followed by ethanol sonication (10 min). The polished GCE surface was then dried at room temperature. Subsequently, the as-prepared YbNRs (2 mg) was dissolved in DMF (1000 µL) and subjected to sonication (20 min). YbNRs solutions (10 µL) were then drop casted on the GCE surface and allowed to dry in an air oven at 60 ˚C. The obtained YBNRs-modified GCE surface was gently rinsed with milli-Q water to remove loosely attached molecules on

the GCE surface. The obtained YbNR/GCE was used for further electrochemical experiments.

3.5.3 Fabrication of ytterbium nanorod decorated with metal oxide nanostructures modified GCE

The MO nanocomposite (NC)-based electrochemical sensors were acquired in the following steps. Initially, a GCE was cleaned with alumina slurry (0.3 µM) and subjected to sonication (10 min) in ethanol. The cleaned GCE surface was then dried at room temperature. Afterwards, the as-prepared metal oxide NCs (2 mg) was dissolved in DMF (1000 µL) and sonicated (20 min) to get homogeneous MO NC solutions. Then, MO NC solutions (10 µL) were drop cast on the GCE surfaces and allowed to dry in an air oven at 60 ˚C. The obtained MO NC-modified GCE surfaces were gently rinsed with DI water to remove loosely attached molecules on the GCE surface. The obtained YbNRs/MnONSs and YbNRs/CoONSs were then employed for further electrochemical experiments. **Fig. 3.1** is an example of NSs-decorated NRs deposited onto the GCE surface and drying at regulated temperatures.

3.6. Preparation of electrolyte solutions

3.6.1. Ferricyanide

Ferricyanide solution was prepared by dissolving $K_3Fe_3(CN)_6$ (32.9 mg, 0.075 mmol), $K_4Fe(CN)_6$ (42.2 mg, 0.115 mmol) and potassium KCl (740 mg, 9.926 mmol) in a 100 mL volumetric flask and filling to the mark. After filling to the mark, the mixture was sonicated for 10 min.

3.6.2. Phosphorus buffer solution

To prepare phosphate buffer solution (PBS), two phosphate solutions (0.1 M were first prepared. The monobasic solution was prepared by dissolving sodium phosphate monobasic (NaH_2PO_4)(1.56 g, 0.013 mol) in milliQ water (100 mL). The dibasic solution was prepared by dissolving sodium phosphate dibasic (Na_2HPO_4) (1.78 g, 0.013) in a 100 mL flask with milliQ water. The two solutions were mixed, and the pH was adjusted using sodium hydroxide and hydrochloric acid solutions under constant stirring

3.7 Detection and quantification procedure

Once the surface modification of **GCE** (referred to as a working electrode (**WE**) below) has been achieved, a typical electrochemical cell consisting of a nitrogen-saturated electrolyte will be inserted with the additional counter electrode (**CE**) that will complete the cycle and balance the current and reference electrode (**RE**) that will serve as a benchmark for determining the potential of the working electrode and connected to a potentiostat system to manipulated readable data (cyclic voltammogram (CV) (used as an example in **Fig. 2.3**)). A suitable sensing potential in the restrictive current region between -0.2 and -1.2 V was determined by applying square wave voltammetry (SWV) at a scan rate of 0.1 mV/s in 1 mM PBS solution and in the same solution containing 1 mM FLU, BIC and OHF. The peak currents in the concentration range between 32.01 and 50.00 µM were collected and the calibration curves for FLU, BIC and OHF were constructed.

3.8 Equations used on calculations

1. Randles-Sevcik relationship for reversible systems

Eqn. 3.1 which reflects the Randles-Sevcik relationship for reversible systems was applied on $K_3Fe_3(CN)_6/K_4Fe(CN)_6$ redox system to determine the surface roughness factors of modified electrodes.

$$I_p = 2.69 \times 10^5 n^{\frac{3}{2}} A C D^{\frac{1}{2}} v^{\frac{1}{2}} \quad (3.1)$$

Where n is the number of electrons involved in the redox reaction, A is the surface area of the electrode (cm^2), D is the diffusion coefficient of the molecule in the bulk solution ($cm^2\ s^{-1}$), C is the concentration of the molecule in the bulk solution (M), and v is the scan rate (V.s). The D value for $K_3Fe_3(CN)_6/K_4Fe(CN)_6$ system has been reported as $7.6 \times 10^{-6}\ cm^2\ s^{-1}$ [12].

2. Surface roughness factors

The surface roughness factors were calculated from the theoretical current acquired from the Randles-Sevcik relationship for reversible systems using the Eqn 3.2.

$$\text{surface roughness} = \frac{\text{Experimental } I_p}{\text{Theoretical } I_p} \quad (3.2)$$

3. Real electrode areas

The real electrode areas were then calculated using Eqn 3.3

$$\text{Real electrode area} = \text{surface roughness} \times \text{theoretical surface area} \quad (3.3)$$

4. Surface coverage Γ for each modified GCE

$$\Gamma = \frac{Q}{nFA} \quad (3.4)$$

Where Q is the charge, n is the number of electrons involved, F is the Faraday constant (96 485 C mol^{-1}), Γ is the surface coverage ($M.cm^{-2}$), A is the surface area of the electrode [13].

5. Limit of detection (LOD)

$$LOD = 3\frac{SD}{B} \quad (3.5)$$

Where SD is the standard deviation and B is the slope.

6. Limit of quantification (LOQ)

$$LOQ = 10\frac{SD}{B} \quad (3.6)$$

Where SD is the standard deviation and B is the slope

7. The Scherrer equation

$$D = \frac{K\lambda}{\beta\cos\theta} \quad (3.7)$$

Where K is the geometry dependent constant of the unit cell 0.9 for a specific structure, λ being the wavelength of the X–ray source (λ = 0.154 nm), β implies the full width at half maximum (FWHM), θ refers to its diffraction angle[14].

References

1. Makhdoom, A. Low Temperature Processing Route of Silicon Nanoparticle Layers for Solar Cell Application. *Friedrich-Alexander-Universität Erlangen-Nürnberg (FAU)*, 45–46 (2018).

2. Joshi, M., Bhattacharyya, A. and Ali, S. W. Characterization techniques for nanotechnology applications in textiles. *Indian J. Fibre Text. Res.* **33**, 304–317 (2008).

3. Flemban, T. High Quality Zinc Oxide Thin Films and Nanostructures prepeated by Pulsed Laser Deposition for Photodetectors High Quality Zinc Oxide Thin films and Nanostructures Prepared by Pulsed Laser Deposition for Photodetectors Dissertation By Tahani Hassan Flemba. PhD diss. 39 (2018).

4. Ahmadi, M., Ghoorchian, A., Dashtian, K., Kamalabadi, M., Madrakian, T. and Afkhami, A. Application of magnetic nanomaterials in electroanalytical methods: A review. *Talanta.* **225**, 121974 (2021).

5. Han, H. and Pan, D. Voltammetric methods for speciation analysis of trace metals in natural waters. *Trends Environ. Anal. Chem.* **29**, e00119 (2021).

6. Safaei, M. & Shishehbore, M. R. A review on analytical methods with special reference to electroanalytical methods for the determination of some anticancer drugs in pharmaceutical and biological samples. *Talanta.* **229**, 122247 (2021).

7. Wang, H.W., Bringans, C., Hickey, A.J., Windsor, J.A., Kilmartin, P.A. and Phillips, A.R. Cyclic Voltammetry in Biological Samples: A Systematic Review of Methods and Techniques Applicable to Clinical Settings. *Signals.* **2**, 138–158 (2021).

8. Liu, J., Xu, Y., Liu, S., Yu, S., Yu, Z. and Low, S.S. Application and progress of chemometrics in voltammetric biosensing. *Biosensors.* **12**, 1–19 (2022).

9. Gill, A. A. S., Singh, S., Thapliyal, N. and Karpoormath, R. Nanomaterial-based optical and electrochemical techniques for detection of methicillin-resistant Staphylococcus aureus: a review. *Microchim. Acta.* **186**, 1-19 (2019).

10. Baruwati, B., Kumar, D. K. and Manorama, S. V. Hydrothermal synthesis of

highly crystalline ZnO nanoparticles: A competitive sensor for LPG and EtOH. *Sensors Actuators, B Chem.* **119**, 676–682 (2006).

11. Wang, J., Luo, N., Peng, S., Yang, L. & Zhao, M. BiPO4:Ln3+ (Ln = Eu, Tb, Eu/Tb) nanorods: Room-temperature synthesis, reaction mechanism, and color-tunable emission. *J. Alloys Compd.* **893**, 162314 (2022).

12. Ardila, J. A., Oliveira, G. G., Medeiros, R. A. and Fatibello-Filho, O. Square-wave adsorptive stripping voltammetric determination of nanomolar levels of bezafibrate using a glassy carbon electrode modified with multi-walled carbon nanotubes within a dihexadecyl hydrogen phosphate film. *Analyst.* **139**, 1762–1768 (2014).

13. Sekhosana, K. E., Shumba, M. and Nyokong, T. Electrochemical Detection of 4-Chlorophenol Using Glassy Carbon Electrodes Modified with Thulium Double-Decker Phthalocyanine Salts. *ChemistrySelect.* **4**, 8434–8443 (2019).

14. Kesavan, G. and Chen, S. M. Highly sensitive manganese oxide/hexagonal boron nitride nanocomposite: An efficient electrocatalyst for the detection of anti-cancer drug flutamide. *Microchem. J.* **163**, 105906 (2021).

CHAPTER 4

SYNTHESIS AND CHARACTERISATION

4.1 Introduction

This chapter discusses the mechanisms for the formation of the as-prepared materials. Furthermore, the characterisation of the as-prepared nanomaterials were also discussed in this chapter.

4.2 Nanomaterial mechanism of formation

4.2.1 Manganese Oxide (MnO) and Cobalt Oxide (CoO) nanostructures (NSs)

The mechanism that is fundamental in the formation of MONSs was derived and is shown in **Fig. 4.1.** In this mechanism, a base releases hydroxyl ions that react with metal ions to form the $M(OH)_4^{2-}$ intermediate. The intermediate leads to the formation of many MO nuclei. Due to the driving forces of high surface energy and electrostatic forces, the MO nuclei aggregate and merge, leading to the formation of MO crystals. The crystals then form MONSs due to low energy [9].

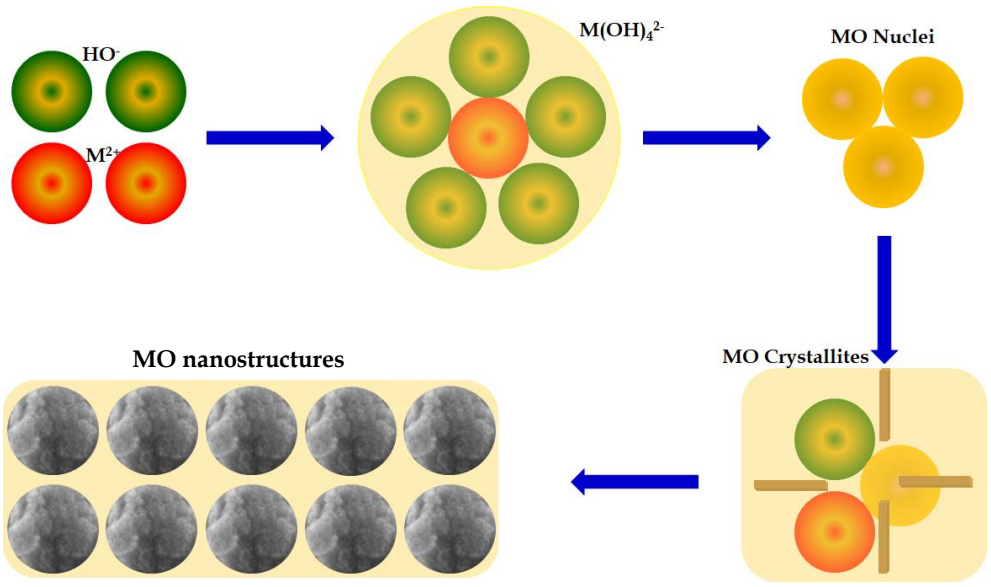

Fig. 4.1: Mechanism for formation of MONSs

4.2.2 Ytterbium (Yb) nanorods (NRs)

The mechanism principal in the formation of YbNRs was derived and is depicted in **Fig. 4.2**. The mechanism starts with the acid solution release of hydronium ions from the acid solution, which then reacts with metal ions to form the $M(HMO_4)^{3-}$ intermediate. The intermediate result in the formation of numerous MO nuclei that aggregate under electrostatic forces and forces of high surface energy. The MO nuclei then merge to produce MO crystallites. The MO crystallites then form YbNRs due to the lower surface energy [9].

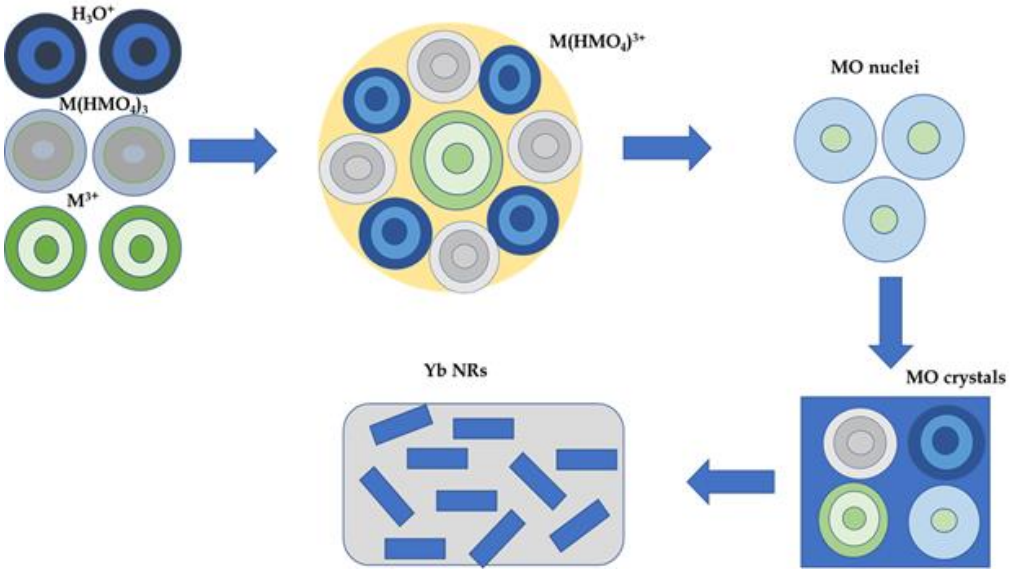

Fig. 4.2: Mechanism for formation of YbNRs

4.3 Nanocomposite synthesis and their mechanism of formation

4.3.1 YbNRs@MONSs nanocomposite (NC)

The mechanism of decorating NRs with MONSs involves the development of MO NSs in the presence of YbNRs, as shown in **Fig. 4.3.** The mechanism involves a base, metal salt and YbNRs as starting materials. Here, a base releases the hydroxyl ions that react with metal ions to form the $M(OH)_4^{2-}$ intermediate. YbNRs do not react in this instance but are dispersed around the intermediate solution. The intermediate leads to the formation of many MO nuclei, which form with YbNRs present in the solution. Due to the driving forces of high surface energy and electrostatic interactions,

the MO nuclei aggregate and merge, forming MO crystals. The crystals then form MONSs around YbNRs, leading to the decoration of YbNRs due to low energy [9].

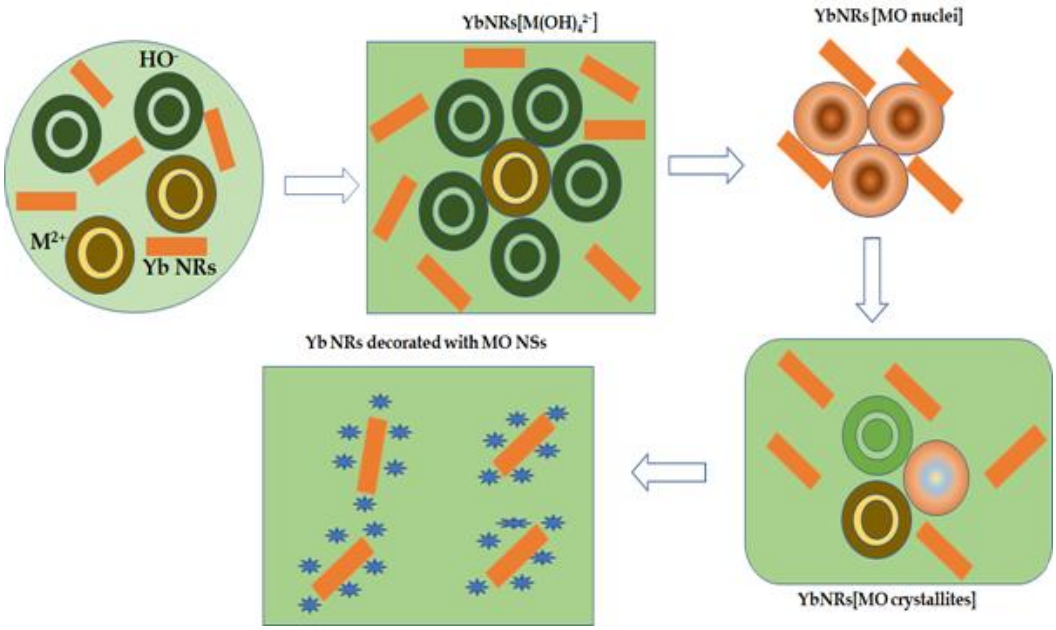

Fig. 4.3: Mechanism illustrating the decoration of YbNRs with MONSs to form YbNRs@MONSs NC.

4.4 Characterisation

4.4.1 Functional group analysis of the as-prepared materials

The vibrational and transitional energies of bonding entities on MnONSs, CoONSs, YbNRs, YbNRs/MnONSs NC and YbNRs/CoONSs NC were studied using FTIR analysis. The FTIR spectra were acquired between 500–1500 cm^{-1}. The spectrum shown in **Fig. 4.4A** indicates the fingerprints for MnONSs with bands around 1160 and 1099 $cm^{-1,}$ which can be assigned to the surface O-Mn–O and Mn stretching, respectfully. The vibration bands of MnONPs were found to be occurring in the same region as other MnONPs reported in the literature [14]. The vibrations in the spectrum prove the presence of a Metal Oxide (MO) in the material. **Fig. 4.4B** represents the FTIR spectrum of CoONSs and shows bands at 650, 750 and 840 $cm^{-1,}$ which can be attributed to Co-O, Co-O-Co and O-Co-O stretching, respectively[15]. These wavelengths are closer to the wavelengths of CoONPs reported in literature[16]. The functional groups acquired in the spectra prove the presence of Metal Oxide (MO) NSs in the as-prepared materials. **Fig. 4.4C** describes the FTIR spectrum of YbNRs and shows the vibrational stretches at 600, 1000 and 1090 $cm^{-1,}$ which can be assigned to

the Yb, Yb-O and O-Yb-O stretching, respectively [17]. Thus, the FTIR spectrum confirms the expected vibrational and transitional behaviour of MnONSs, CoONSs and YbNRs. The FTIR spectrum of YbNRs/MnONSs NC is shown in **Fig. 4.4D**. A vibration band at 600 cm^{-1} was observed and can be attributed to Yb-O stretching [17]. Another vibration band was observed at 1000 cm^{-1} and could be ascribed to the Mn-O stretching, as discussed in **Fig. 4.4A**. Similarly, the FTIR spectrum of YbNRs/CoONSs NC is shown in **Fig. 4.4E.** A vibrational stretch at 560 cm^{-1} was observed from the spectrum and can be assigned to the Yb-O stretch. However, the vibration has shifted a bit, as it was observed at 600 cm^{-1} on the YbNRs spectrum. Furthermore, the spectrum also reveals a vibrational band at 650 cm^{-1}, which can be attributed to Co-O stretch, similar to the observation in **Fig. 4.4B**. Therefore, these FTIR spectra confirm the formation of YbNRs decorated with MnONSs and CoONSs.

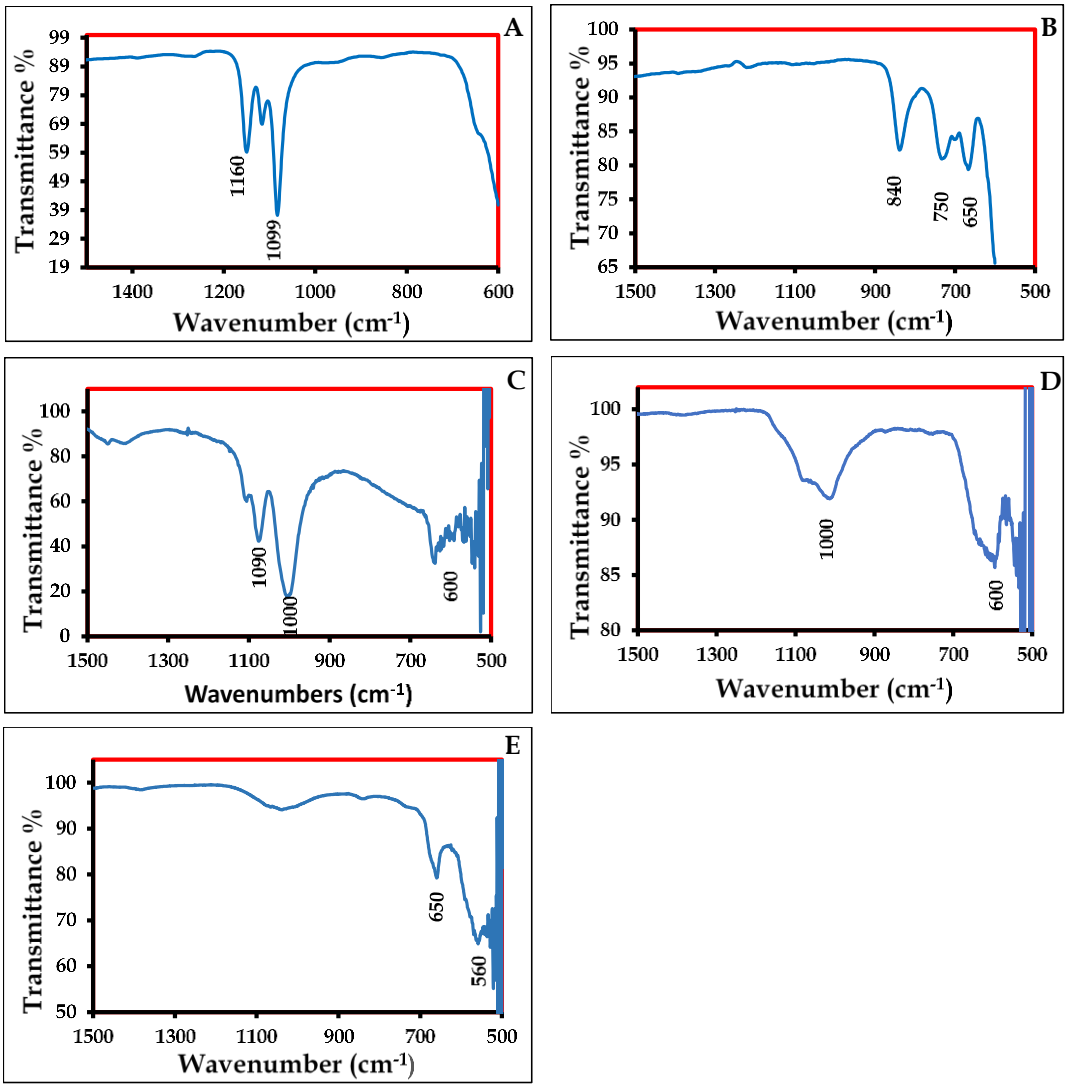

Fig. 4.4: FTIR spectra of (A) MnONSs, (B) CoONSs, (C) YbNRs, (D) YbNRs/MnONSsNC and (E) YbNRs/CoONSs NC.

4.4.2 UV-Vis analysis of the as-prepared materials

The UV-Vis technique was employed to study the ground state electronic absorption behaviour of MnONSs, CoONSs, YbNRs, YbNRs/MnONSs NC and YbNRs/CoONSs NC. **Fig. 4.5A** shows the UV-Vis spectrum of MnONSs. A broad absorption band was observed between 314–620 nm, with the absorption maximum at 400 nm. The observed ground state electronic absorption behaviour of MnONSs corresponds with those reported elsewhere [18,19]. The UV-Vis spectrum of CoONSs illustrated in **Fig. 4.4B** was recorded between 250-800 nm. From the CoONSs spectrum, an absorption band between 360-600 nm was observed, with the absorption maximum at 450 nm. Furthermore, it was also observed in the CoONSs spectrum that there was another small absorption shoulder at 265 nm, which could be due to Co^{2+} ions of different absorption energy. The absorption of CoONSs was in agreement with those reported in literature [20].

Similarly, the ground state electronic absorption behaviour of YbNRs was studied between 250-800 nm, as depicted in **Fig. 4.5C**. The YbNRs UV-Vis spectrum shows a broad absorption band between 580-800 nm with an absorption band at 700 and 770 nm. The YbNRs spectrum shows another absorption peak at 520 nm. These absorption bands can all be assigned to Yb absorption since lanthanide chemistry differs from transition elements. Thus, the ground-state electronic absorption behaviour is completely different. With lanthanides, many absorption bands are normally observed [21–23]. **Fig. 4.5D** shows the UV-Vis spectrum of YbNRs/MnONSs NC at the wavelength range from 250-800 nm. The YbNRs/MnONSs spectrum shows a broad absorption band between 500-650 nm with an absorption maximum observed at 560 nm. This absorption band can be assigned to that of MnO. However, due to the presence of the rare-earth metal, ytterbium, the absorption shifted from 400 nm to 560 nm with reference to the UV-Vis spectrum in **Fig. 4.5A**.

Additionally, two more absorption peaks at 745 and 770 nm were also observed in the YbNRs/MnONSs spectrum and can be ascribed to the absorption of Yb. One absorption peak moved from 700 – 745 nm due to the presence of Mn in the sample

compared to the UV-Vis spectrum in **Fig. 4.5C. Fig. 4.5E** shows the UV-Vis spectrum of YbNRs/CoONSs NC recorded between 250-800 nm. This spectrum shows a broad absorption band between 250-500 nm, with the absorption maximum observed at 330 nm. This absorption band moved from 450 – 330 nm and can be attributed to CoO absorbance with reference to **Fig. 4.5B**. The YbNRs/CoONSs UV-Vis spectrum also reveals the absorption peaks at 520 and 700 nm, which can be assigned to the absorption of Yb, as previously discussed in **Fig. 4.5C**. The maximum absorption in the spectra confirms the optical characteristics of the as-prepared materials.

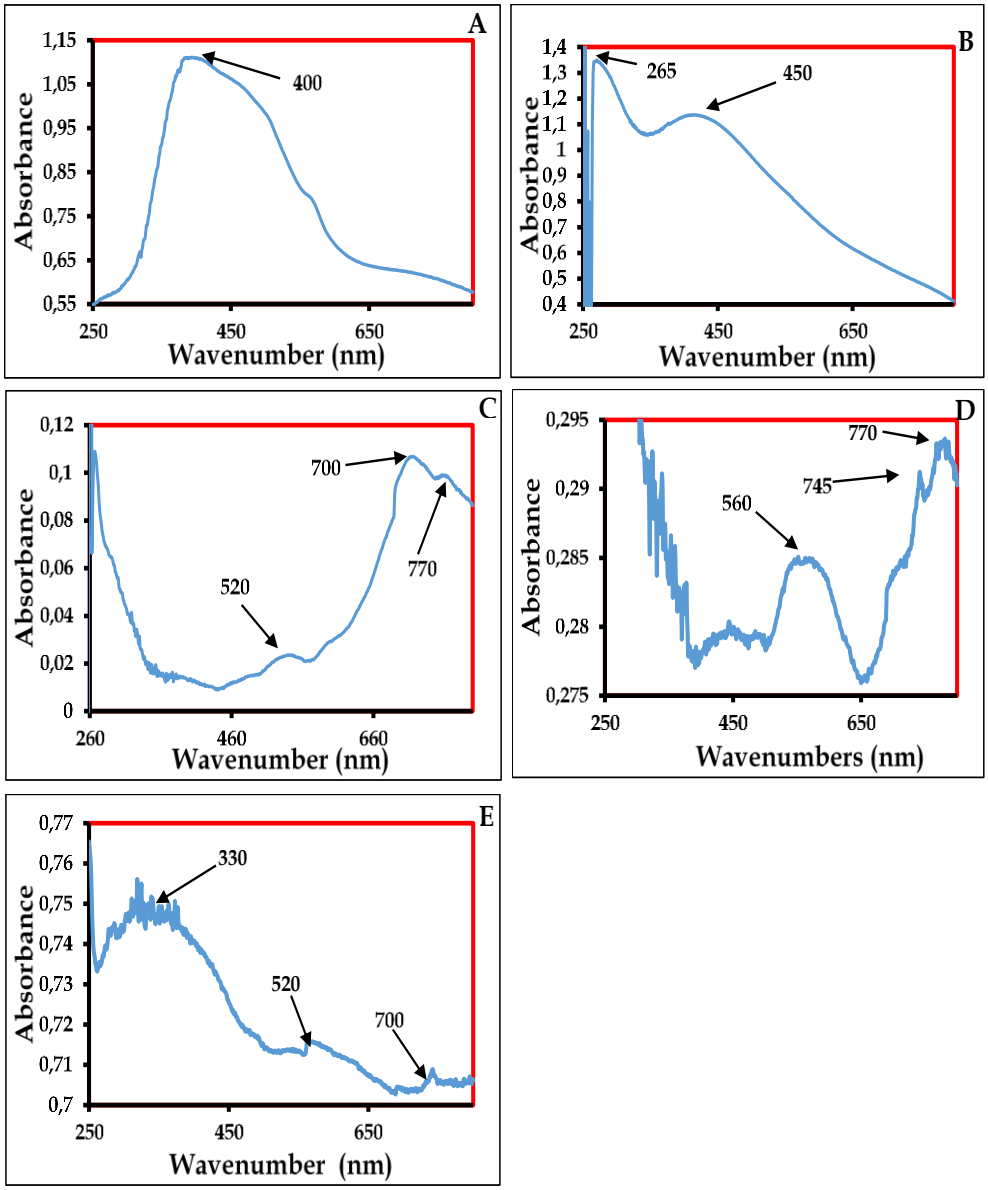

Fig. 4.5: UV-Vis spectra of (A) MnONSs; (B) CoONSs; (C) YbNRs; (D) YbNRs/MnONSs NC; (E) YbNRs/CoONSs NC.

4.4.3 Morphological analysis

The surface morphologies of MnONSs, CoONSs, YbNRs YbNRs/MnONSs NC and YbNRs/CoONSs NC were examined using SEM. **Fig. 4.6A** shows the SEM image of MnONSs. The image shows a big nest-like nanostructure which seem to exhibit a porous structure. Furthermore, the formation of the nest-like morphology was comprised of small rod-like petals of uniform particle size distribution. This material in the SEM image has a similar morphology as those of MnONSs reported in the literature [24–26]. **Fig. 4.6B** shows an SEM image of CoONSs. From the Figure, small-clustered structures were observed, with some coming together to form a bigger cluster. The nanostructures had uniform particle size distribution with one agglomerate. The observed SEM images are similar to those reported elsewhere for other CoONSs [27–29]. **Fig. 4.6C** depicts the SEM image of YbNRs and shows needle-like morphologies of uniform particle size distribution. NRs of a similar morphology have been reported in literature [30,31].

SEM analysis was also employed to examine the surface morphologies of the as-prepared NRs decorated with MnONSs and CoONSs. The SEM image of YbNRs/MnONSs NSs is shown in **Fig. 4.6D.** The formation of MnONSs around the needle-like rod morphologies were observed. The decoration was a bit uniform as one small MnONSs cluster was forming at the surface of each YBNR as depicted on the insert picture. This image confirms the formation of YbNRs decorated with MnONSs. **Fig. 4.6E** shows an SEM image of YbNRs/CoONSs NC. It was established from this image that CoONSs have formed around the needle-like NRs confirming the decoration of YbNRs with CoONSs. The decoration was not uniform as other YBNRs had a lot of CoONSs clusters around them while some had just a few to one cluster around them. From **Fig. 4.6D** and **E**, it can be concluded that the decoration of YbNRs with MnONSs and CoONSs was successful.

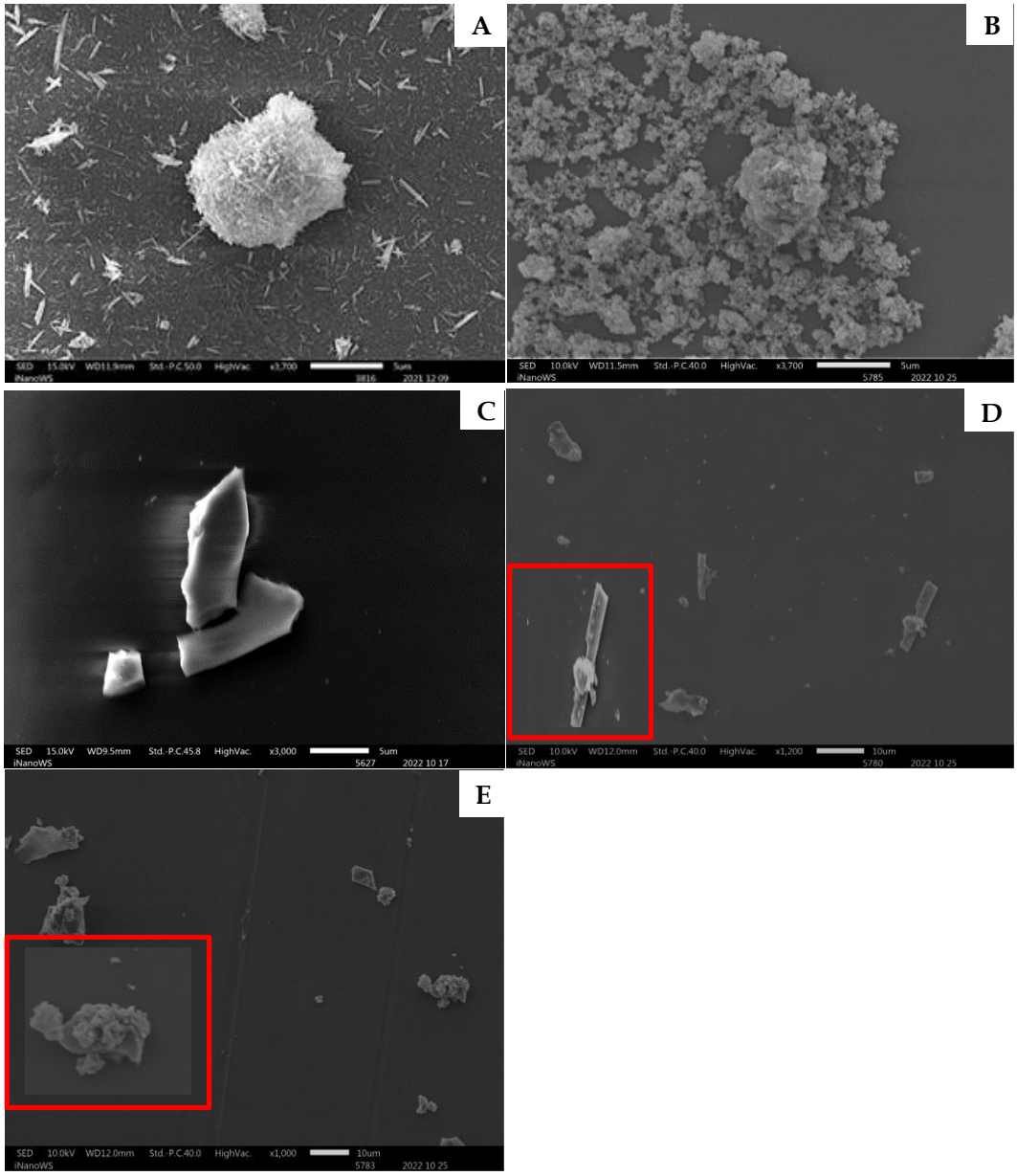

Fig. 4.6: SEM images of (A) MnONSs; (B) CoONSs; (C) YbNRs; (D) YbNRs/MnONSs NC; (E) YbNRs/CoONSs NC.

4.4.4 Elemental distribution mapping of the as-prepared materials

4.4.4.1. Manganese Oxide NSs

The elemental mapping of MnONSs was also employed in this study using EDX. **Fig. 4.7A** displays the elemental mapping of the mixture of elements at the surface of MnONSs. The mapping images further reveal the presence of manganese, oxygen and carbon elements in their respective elemental mapping portrayed in **Fig. 4.7B**, **C**

and **D**, respectively. The carbon observed is due to the carbon tape used during analysis.

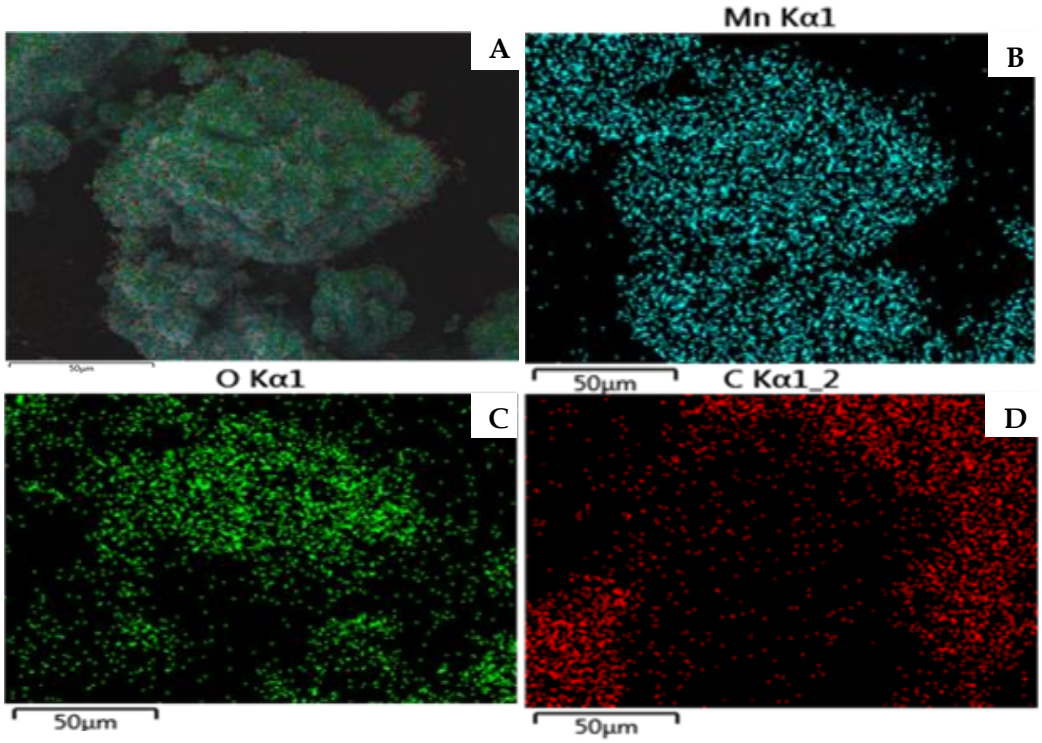

Fig. 4.7: EDX mapping of (A) mixture of elements; (B) Manganese; (C) Oxygen; (D) Carbon.

4.4.4.2 Cobalt Oxide NSs

The elemental mapping of CoONSs was also employed in this study and is shown in **Fig. 4.8.** The mapping first displays the mixture of elements on the surface of CoONSs, as displayed in **Fig. 4.8A**. The mapping images further reveal the presence of cobalt, oxygen and carbon, which can be attributed to the carbon tape and chlorine, resulting from the cobalt chloride precursor used as depicted in their respective elemental mapping denoted by **Fig. 4.8B**, **C**, **D** and **E** respectively. The presence of these elements proves the formation of CoONSs.

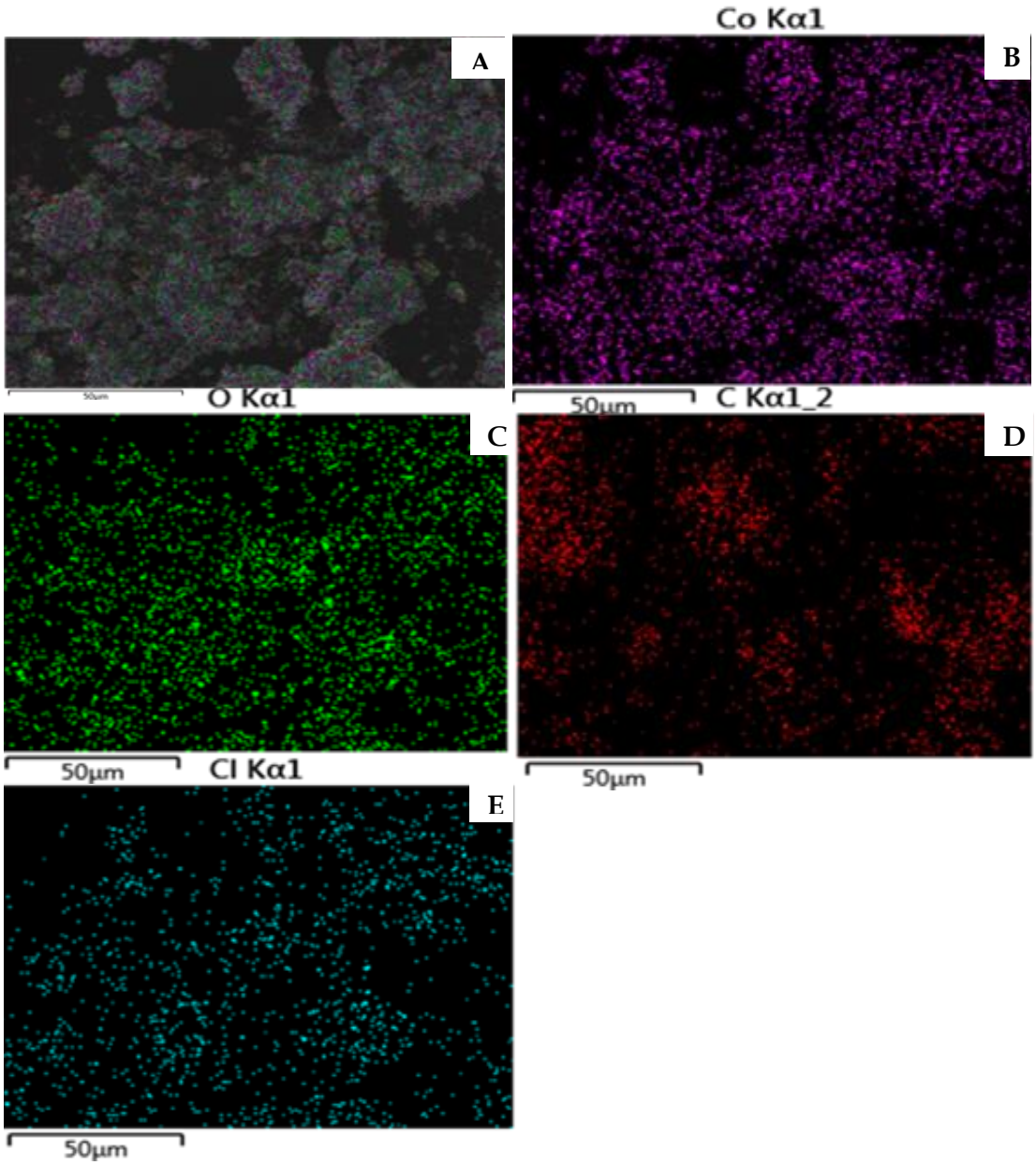

Fig. 4.8: EDX mapping of (A) mixture of elements; (B) cobalt; (C) oxygen; (D) carbon; (E) chlorine.

4.4.4.3 Ytterbium NRs

The elemental mapping of YbNRs has been studied and is presented in **Fig. 4.9**. The elemental mapping of the mixture of elements at the surface of YbNRs is shown in **Fig. 4.9A.** The mapping images also reveal the presence of carbon, oxygen, phosphorous and ytterbium, as depicted in their respective mapping in **Fig. 4.9B**, **C**, **D** and **E**. The phosphorous element can be attributed to the precursor used in the synthesis, and the carbon can be ascribed to the carbon tape.

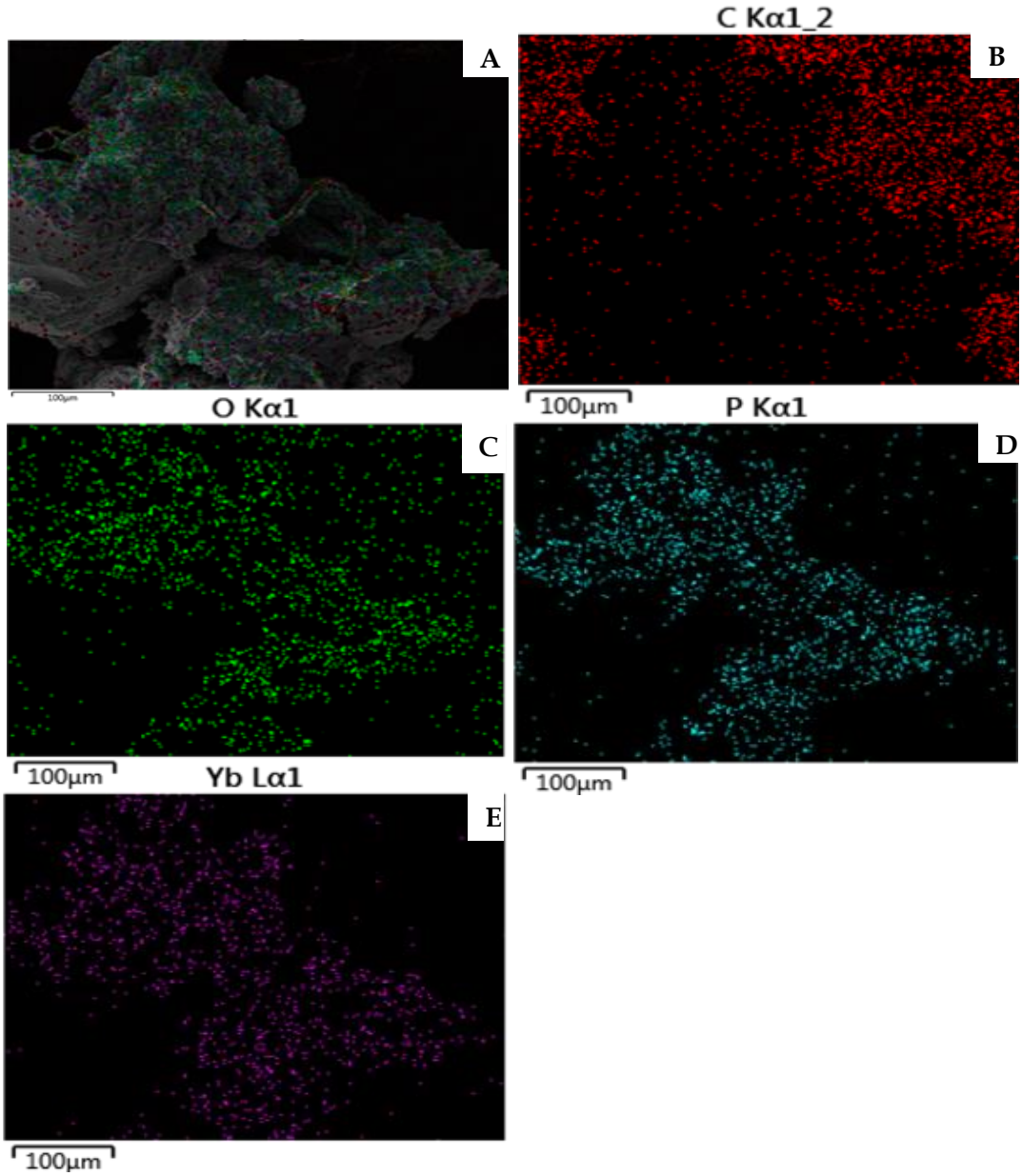

Fig. 4.9: EDX mapping of (A) mixture of elements, (B) carbon, (C) oxygen, (D) phosphorous and (E) ytterbium on YbNRs sample.

4.4.4.4 YbNRs/MnONSs NC

Elemental mapping of the prepared YbNRs/MnONSs nanocomposite was also studied and is depicted in **Fig. 4.10.** The elemental mapping of the mixture of elements is shown in **4.10A**. The mapping images further denote the presence of manganese, ytterbium and oxygen as shown in their respective elemental mapping as depicted in **Fig. 4.10B**, **C**, and **D**, respectively. The elemental mapping confirms the attachment of MnONSs to the surface of YbNRs.

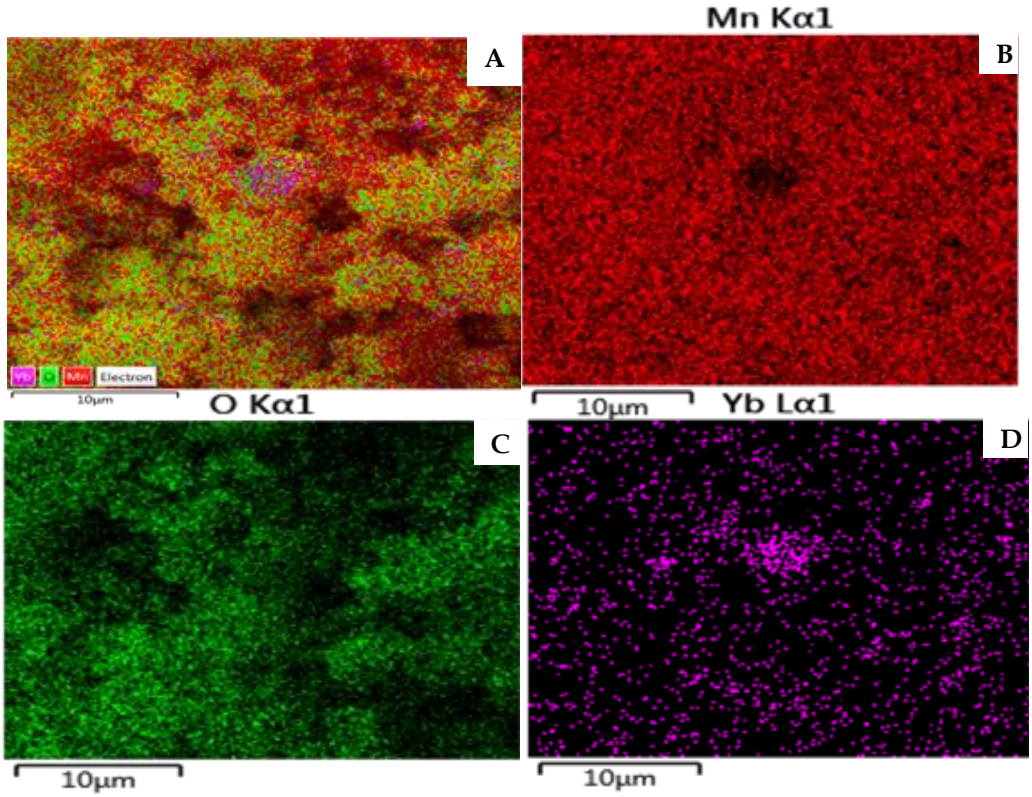

Fig. 4.10: EDX mapping of (A) mixture of elements; (B) manganese; (C) oxygen; (D) ytterbium.

4.4.4.5 YbNRs/CoONSs NC

Elemental mapping of the as-prepared YbNRs/CoONSs nanocomposite was also studied in this study and is depicted in **Fig. 4.11**. The elemental mapping of the mixture of elements at the surface of YbNRs/CoONSs is displayed in **Fig. 4.11A**. The mapping images reveal the presence of cobalt, sodium, carbon, phosphorous, ytterbium and oxygen as depicted in their elemental maps in **Fig. 4.11 B**, **C**, **D**, **E**, **F**, and **G**, respectively. The phosphorous and sodium might be impurities since they were not observed on the surface of YbNRs/MnONSs. These metals' presence confirms the presence of CoONSs at the surface of YbNRs.

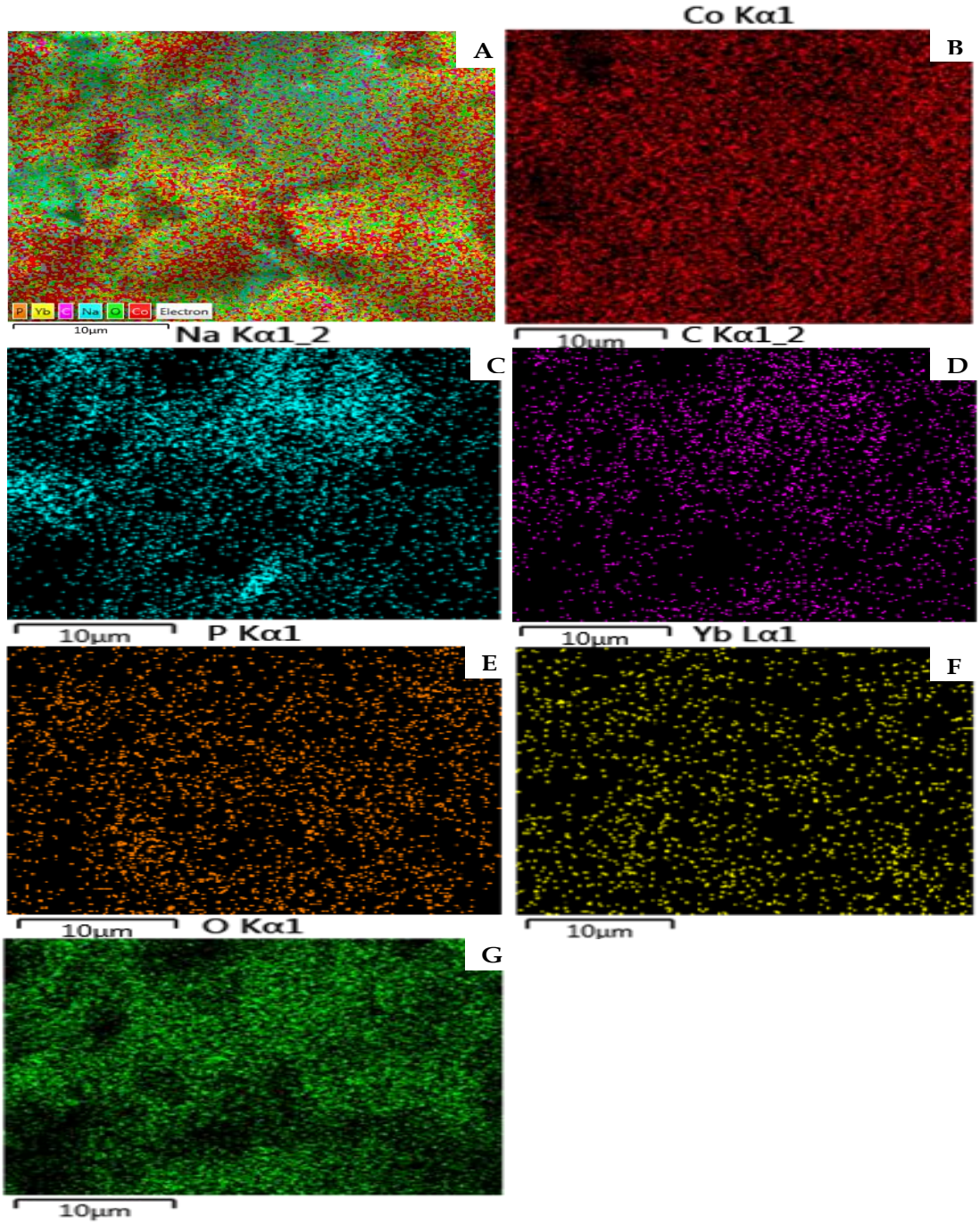

Fig. 4.11: EDX mapping of (A) mixture of elements, (B) cobalt, (C) sodium, (D) carbon, (E) phosphorous, (F) ytterbium, (G) oxygen.

4.4.5 EDX spectra of the as-prepared materials

EDX spectra were also acquired by studying the surface of the as-prepared materials. **Fig. 4.12A** displays the EDX spectrum MnONSs. The spectrum only confirms the presence of carbon, oxygen and manganese elements, thereby confirming the purity of MO (MnO) NSs. The spectrum emitted prominent peak in the manganese region

which strongly indicates the presence of manganese, corresponding to 73.3 mass% of manganese. Another peak was that of oxygen which corresponded to 36.2 mass% of oxygen. The mass percentages are in correspondence to the synthetic content of MnONSs as there was more manganese used than the source of oxygen where only drops were used in the synthesis. As shown **in Fig. 4.12B**, the presence of cobalt, oxygen and carbon was established, as well as traces of chlorine element, which are a result of the cobalt chloride precursor used in the hydrothermal synthesis of CoONSs. The spectrum shows a prominent peak in the cobalt region which corresponds to 67 mass% of cobalt. The other peaks observed are those of oxygen and chlorine corresponding to 24.6 mass% and 8.4 mass%, respectively. The mass percentages correspond to the synthesis method used as cobalt was in the precursor dissolved and the only source of oxygen was the drops added to the solution with chlorine being an impurity from the precursor.

Fig. 4.12C shows the EDX analysis spectrum of YbNRs.The spectrum confirms the presence of carbon, oxygen, ytterbium and a phosphorous element from the precursor used. The content of ytterbium in surface layer was 29.2 mass% which is relatively lower than what was expected from the synthesis. From the spectrum, oxygen is the one with a prominent peak corresponding to 36.2 mass% of oxygen which is corresponding to the synthesis as there are two precursors which are a source of oxygen. However, oxygen was expected to be lower than ytterbium when it comes to mass percentage. The other mass percentages are those of the carbon tape and phosphorous from the precursor which are fair.

The EDX analysis spectrum of YbNRs/MnONSs NC is shown in **Fig. 4.12D** and confirms the presence of carbon, oxygen and manganese, ytterbium, sodium and phosphorous elements only. The phosphorous and sodium elements might be impurities as they are not observed on elemental mapping. The spectrum shows a very prominent peak of manganese corresponding to 70.5 mass% and very small peaks of ytterbium corresponding to 4.2 mass% of ytterbium. This means that there is way too much manganese than ytterbium in the as-prepared nanocomposite. The mass percentage of oxygen in the as-prepared material is 22.2 mass% and is okay in relation to the decoration process. The remaining percentages are from the impurities from the precursors, phosphorous and sodium. However, this information still confirms the presence of both YbNRs and MnONSs in the YbNRs/MnONSs NC.

Fig. 4.12E illustrates the EDX spectrum of YbNRs/CoONSs NC, revealing the presence of cobalt, oxygen, ytterbium, sodium, sulfur, phosphorous and carbon. Sodium and sulfur are impurities. These elements prove the presence of both YbNRs and CoONSs in the YbNRs/CoONSs NC. The phosphorous, sulfur and sodium are from the precursors used in the hydrothermal synthesis of YbNRs/CoONSs NC. From the spectrum it can be observed that the mass percentages of cobalt and ytterbium are 39.2 mass% and 2.9 mass%, respectively. The mass percentage of ytterbium is also very small, however, in this case the mass percentage of cobalt is also not that high. This shows that there is more cobalt than ytterbium in the as-prepared material. The spectrum also shows a lot of impurities on the surface of the material which also have big mass percentages. Nonetheless, this information proves the successful decoration of YBNRs with CoONSs. Based on the observations above, it can be concluded that MnONSs, CoONSs, YbNRs YbNRs/MnONSs NC and YbNRs/CoONSs NC were successfully formed as their surfaces have all the necessary elements.

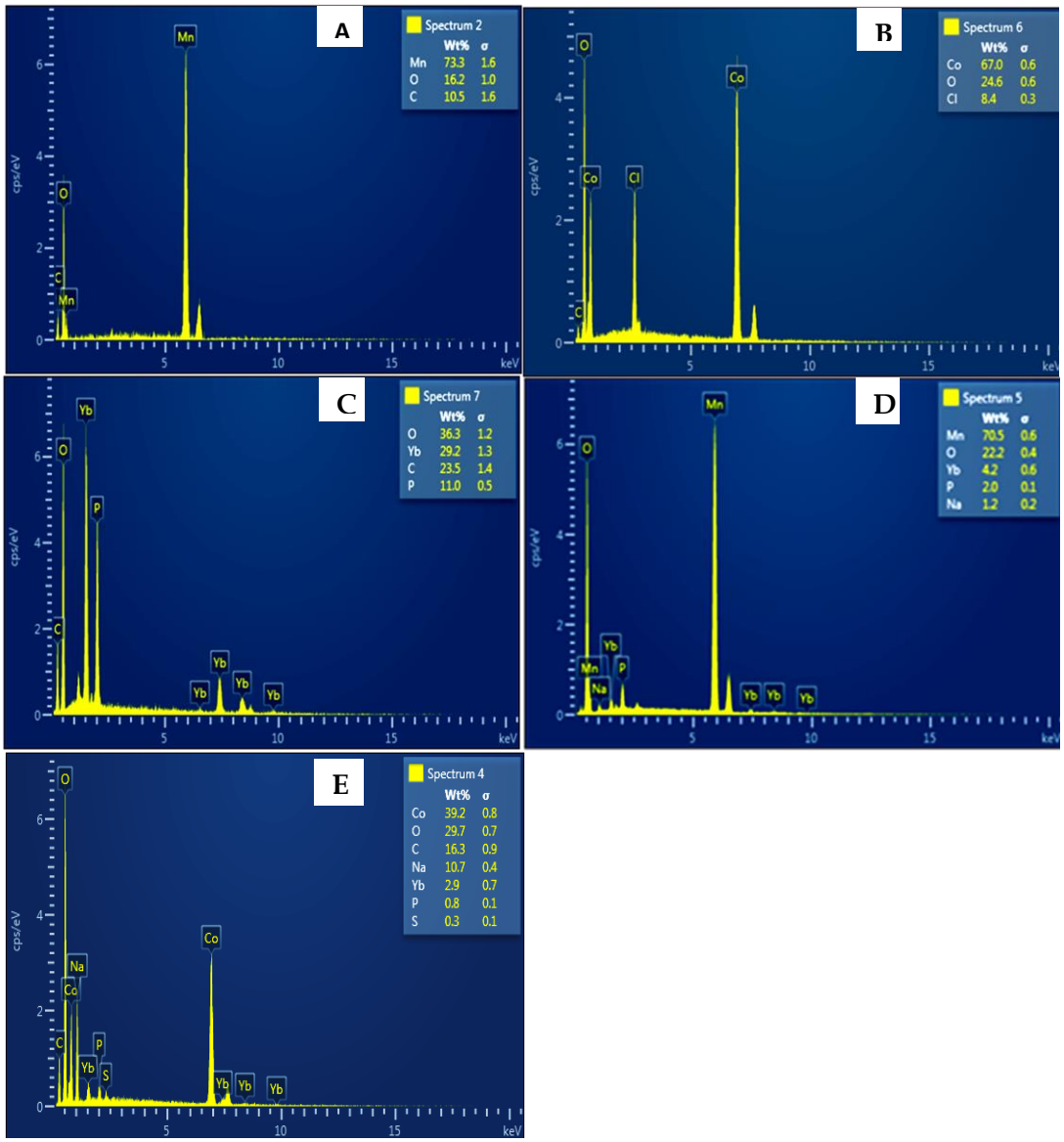

Fig. 4.12: EDX spectra of (A) MnONSs and (B) CoONSs, (C) YbNRs, (D) YbNRs/MnONSs NC, (E) YbNRs/CoONSs NC NC.

4.4.6 TEM analysis of the as-prepared materials

The surface morphologies of MnONSs, CoONSs, YbNRs YbNRs/MnONSs NC and YbNRs/CoONSs NC materials were further examined using TEM analysis. The TEM image of MnONSs is displayed in **Fig. 4.13A** and shows uniform size particles with morphologies of rods coming together to form clusters with some nearly spherical particles on the side. NSs of such morphologies are not new and have been reported in literature [32,33]. **Fig. 4.13B** shows the TEM image of the as-prepared CoONSs. The image shows small rod-like clusters of non-uniform particle size distribution. The TEM images of the CoONSs are similar to those of CoONSs reported in literature [34]. The

surface morphology of YbNRs was also analysed, and the image is presented in **Fig. 4.13C**. The image shows unclear and uneven morphologies that do not have a uniform morphology; in some areas, they look like thick rods, and in some, they look like circles. These unclear morphologies might result from sample preparation of the as-prepared YbNRs. **Fig. 4.13D** shows the TEM image of YbNRs/MnONSs NC. As shown in the image, there are uniform size rod-like structures surrounded by small uniform size clusters. This proves the successful decoration of YbNRs with MnONSs. The TEM image of YbNRs/CoONSs NC is shown in **Fig. 4.13E**. The image also shows non-uniform size rod-like structures surrounded by non-uniform size clusters. This confirms the formation of YbNRs decorated with CoONSs.

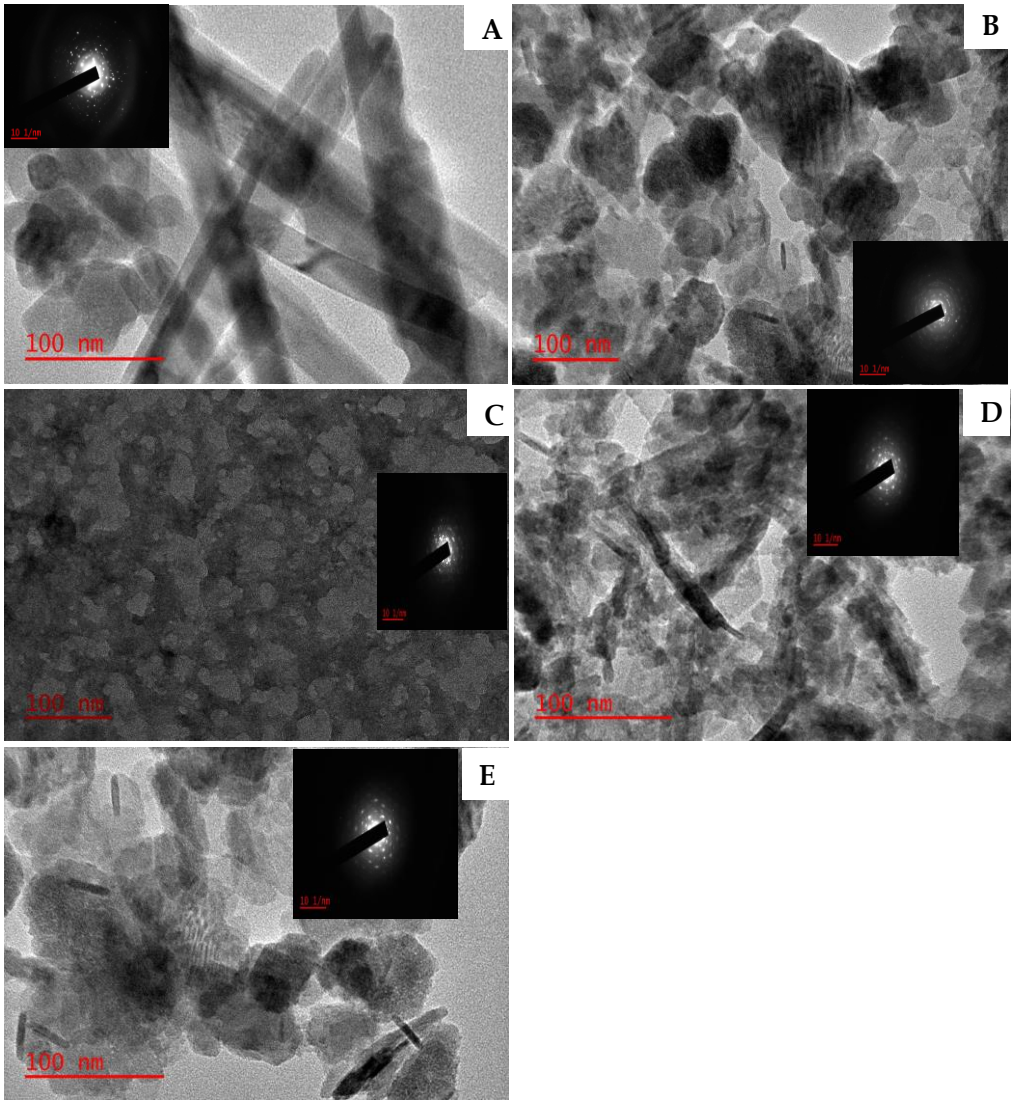

Fig. 4.13: TEM images of (A) MnONSs; (B) CoONSs; (C) YbNRs; (D) YbNRs/MnONSs NC; (E) YbNRs/CoONSs NC.

4.4.7 XRD analysis of the as-prepared materials

The phases present in the crystalline composition of MnONSs, CoONSs, YbNRs YbNRs/MnONSs NC and YbNRs/CoONSs NC materials were established by the XRD technique as shown in **Fig. 4.14**. The X-ray diffractogram of MnONSs evaluated using XRD and its miller indices are shown in **Fig. 4.14A**. The XRD spectrum reveals the pure phase of MnONSs, and all the diffraction peaks could be indexed to (JCPDS No. 88-0649), determining γ-MnOOH[34,35]. The observed miller indices of MnONSs are (111), (020), (111), (002), (121), (210), (220), (222), (113), (131), (131), (202) and (131). The prominent diffraction peak at 2θ= 26.1 demonstrates the excellent

crystalline structure of MnONSs of the tetragonal symmetry. **Fig. 4.14B** depicts the X-ray diffractogram of CoO NSs evaluated by XRD. The diffraction peaks in the spectrum depict a pure phase of CoONSs and could be indexed to (JCPDS No. 43-1003) of the cubic symmetry[36]. The observed miller indices of CoONSs are (111), (220), (311), (222), (400), (422), (511), and (440). The prominent diffraction peak at 2θ = 36.8 demonstrates the excellent crystalline phase of CoONSs. **Fig. 4.14C** shows the X-ray diffractogram of the YbNRs, with miller indices as (211), (222), (400), (431), (440) and (622) that are in congruence with a cubic Yb_2O_3 phase, based on comparisons with the JCPDS 00-041-1106 [37]. The miller indices show a crystalline structure of YbNRs. **Fig. 4.14D** depicts the XRD structure of YbNRs/MnONSs NC and has miller indices as (200), (220), (310), (400), (411), (521), (002) and (402), which resembles the JCPDS 44-0141 of the tetragonal symmetry[38]. This XRD pattern shows that MnONS can affect the crystalline phase of YbNRs but maintain the crystalline structure. The XRD pattern of YbNRs/CoONSs NC is represented in **Fig. 4.14E** and shows miller indices as (111), (220), (222), (400), (422), (511) and (440) which are consistent with the JCPDS 01-073-1701 of the cubic symmetry [39]. CoONSs can affect the crystalline phase of YbNRs but maintain the crystalline structure. The prominent diffraction peak at 2θ = 19.1 demonstrates the excellent crystalline phase of YbNRs/CoONSs NC. The average crystallite sizes (D) of the as-prepared materials were calculated using the Scherrer equation provided in chapter 3 (eqn 3.7). The average crystalline sizes were calculated to be 4.30 nm for MnONSs, 3.90 nm for CoONSs, 1.29 nm for YbNRs, 3.88 nm for YbNRs/MnONSs NC and 3.23 nm for YbNRs/CoONSs NC.

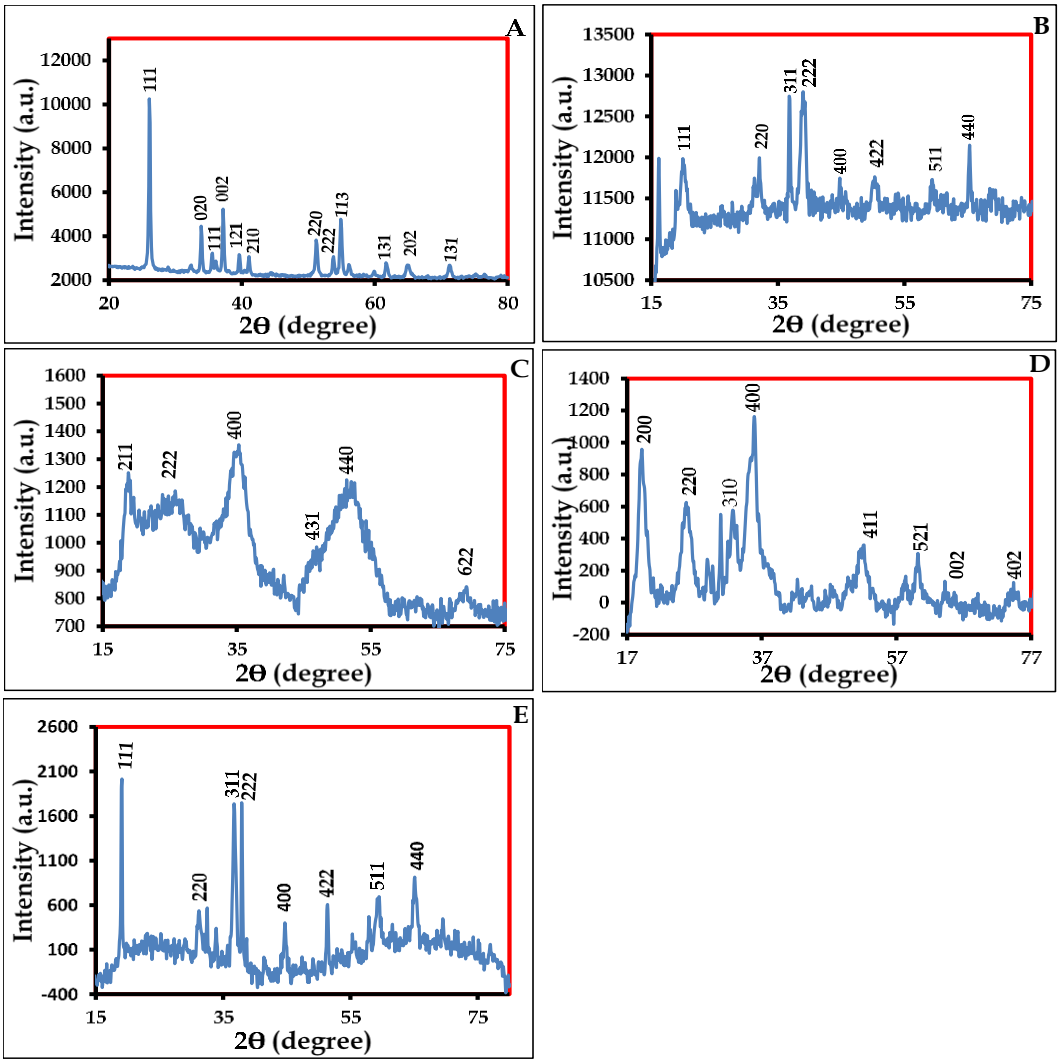

Fig. 4.14: X-ray diffractograms of (A) MnONSs; (B) CoONSs; (C) YbNRs; (D) YbNRs/MnONSs NC; (E) YbNRs/CoONSs NC.

Conclusion

The characterisation techniques employed in this study prove the successful synthesis of MnONSs, CoONSs, YbNRs YbNRs/MnONSs NC and YbNRs/CoONSs NC. The FTIR stretches of the as-prepared materials corresponded with those of the materials with the same elemental compositions reported in the literature. For the as-prepared NCs, the stretches confirmed the presence of both YbNRs and MONSs. UV-Vis absorptions of the as-prepared materials suggest their successful formation and further prove the decoration of YbNRs with MONSs. EDX mapping and spectra confirmed the elements that suggest the successful synthesis of the as-prepared materials. TEM and XRD further confirmed the successful formation and symmetry of the materials. SEM showed the shapes of the as-prepared materials.

References

1. Dixini, P. V. M., Carvalho, B. B., Gonçalves, G. R., Pegoretti, V. C. B. and Freitas, M. B. J. G. Sol–gel synthesis of manganese oxide supercapacitor from manganese recycled from spent Zn–MnO2 batteries using organic acid as a leaching agent. *Ionics (Kiel).* **25**, 4381–4392 (2019).

2. Duraia, E. S. M., Fahami, A. and Beall, G. W. Microwave-Assisted Synthesis of N-Doped Graphene-Wrapped MnO2 Nanoflowers. *J. Electron. Mater.* **47**, 7288–7295 (2018).

3. Qing, X., Liu, S., Huang, K., Lv, K., Yang, Y., Lu, Z., Fang, D. and Liang, X. Electrochimica Acta Facile synthesis of Co 3 O 4 nanoflowers grown on Ni foam with superior electrochemical performance. *Electrochim. Acta* **56**, 4985–4991 (2011).

4. Shen, Z. G., Chen, J. F. and Yun, J. Preparation and characterizations of uniform nanosized BaTiO3 crystallites by the high-gravity reactive precipitation method. *J. Cryst. Growth* **267**, 325–335 (2004).

5. Jamkhande, P. G., Ghule, N. W., Bamer, A. H. and Kalaskar, M. G. Metal nanoparticles synthesis: An overview on methods of preparation, advantages and disadvantages, and applications. *J. Drug Deliv. Sci. Technol.* **53**, 101174 (2019).

6. Gan, Y. X., Jayatissa, A. H., Yu, Z., Chen, X. and Li, M. Hydrothermal Synthesis of Nanomaterials. *J. Nanomater.* **2020**, 1-3 (2020).

7. Yoshimura, M. and Byrappa, K. Hydrothermal processing of materials : past , present and future. *J. Mater. Sci.* **43**, 2085–2103 (2008).

8. Adschiri, T., Hakuta, Y. and Arai, K. Hydrothermal synthesis of metal oxide fine particles at supercritical conditions. *Ind. Eng. Chem. Res.* **39**, 4901–4907 (2000).

9. Tang, J. F., Su, H. H., Lu, Y. M. and Chu, S. Y. Controlled growth of ZnO nanoflowers on nanowall and nanorod networks via a hydrothermal method. *CrystEngComm.* **17**, 592–597 (2015).

10. Sohn, Y. Yb 2 O 3 nanowires , nanorods and nano-square plates. *Ceram. Int.*

44, 3341–3347 (2018).

11. Wang, H., Lu, W., Zeng, T., Yi, Z. and Rao, L. Multi-functional NaErF 4 : Yb nanorods : enhanced imaging. *Nanoscale*. **6***,* 2855–2860 (2014).

12. Ramadoss, A., Krishnamoorthy, K. and Kim, S. J. Novel synthesis of hafnium oxide nanoparticles by precipitation method and its characterization. *Mater. Res. Bull.* **47**, 2680–2684 (2012).

13. Yang, G. and Park, S. J. Conventional and microwave hydrothermal synthesis and application of functional materials: A review. *Materials (Basel).* **12**, 1177 (2019).

14. Moon, S. A., Salunke, B. K., Alkotaini, B. and Sathiyamoorthi, E. plant extract Biological synthesis of manganese dioxide nanoparticles by Kalopanax pictus plant extract. *IET nanobiotechnology*. **9**, 220-225 (2015).

15. Seshan, V. On the preparation , structural and magnetic properties of ZnO : Co nanoparticles On the preparation , structural and magnetic properties of ZnO : Co nanoparticles. *Eur. Phys. J. Appl. Phys.* **66**, 10602 (2014).

16. Naveen, N. Investigation on physiochemical properties of Mn substituted spinel cobalt oxide for supercapacitor applications. *Electrochimica Acta.* **125**, 404-414 (2019).

17. Lenz Leite, M., Viard, A., Galusek, D. and Motz, G. In Situ Generated β-Yb2Si2O7 Containing Coatings for Steel Protection in Extreme Combustion Environments. *Adv. Mater. Interfaces* **8**, 2100384 (2021).

18. Yadegari, H. and Wang, H. Three-dimensional MnO 2 ultrathin nanosheet aerogels for high- performance Li–O 2 batteries. *J. Mater. Chem. A.* **3**, 2559-2563 (2015).

19. Moon, S. A., Salunke, B. K., Saha, P., Deshmukh, A. R. and Kim, B. S. Comparison of dye degradation potential of biosynthesized copper oxide , manganese dioxide , and silver nanoparticles using Kalopanax pictus plant extract Comparison of dye degradation potential of biosynthesized copper oxide , manganese dioxide , and sil. *Korean J. Chem. Eng.* **35**, 702-708. (2018).

20. Alrehaily, L.M., Joseph, J.M., Biesinger, M.C., Guzonas, D.A. and Wren, J.C.

Gamma-radiolysis-assisted cobalt oxide nanoparticle formation. *Phys. Chem. Chem. Phys*. **15**, 1014-1024 (2013).

21. Wang, Q., Tan, M. C., Zhuo, R., Kumar, G. A. and Riman, R. E. A solvothermal route to size-and phase-controlled highly luminescent NaYF 4:Yb,Er Up-conversion nanocrystals. *J. Nanosci. Nanotechnol.* **10**, 1685–1692 (2010).

22. Sallam, O. I. and Elalaily, N. A. Physical and structural properties of gamma irradiated ytterbium phosphate glasses as a nominated lasing material. *J. Mater. Sci. Mater. Electron.* **33**, 1078–1090 (2022).

23. Peretti, R., Jurdyc, A.M., Jacquier, B., Gonnet, C., Pastouret, A., Burov, E. and Cavani, O. How do traces of thulium can explain photodarkening in Yb doped fibers? *Opt. Express* **18**, 20455 (2010).

24. Xu, N., Liu, Z.H., Ma, X., Qiao, S. and Yuan, J. Controlled synthesis and characterization of layered manganese oxide nanostructures with different morphologies Controlled synthesis and characterization of layered manganese oxide nanostructures with different morphologies. *J. Nanopart. Res.* **11**, 1107-1115 (2014).

25. Yu, L.L., Zhu, J.J. and Zhao, J.T. Beta-manganese dioxide nanoflowers self-assembled by ultrathin nanoplates with enhanced supercapacitive performance. *J. Mater. Chem. A*. **2**, 9353-9360 (2014).

26. Khan, Y., Durrani, S. K., Mehmood, M., Khan, M. R. and Introduction, I. Mild hydrothermal synthesis of c -MnO 2 nanostructures and their phase transformation to a -MnO 2 nanowires. *J. Mater. Res.* **26**, 2268-2275 (2011).

27. Barthwal, S. and Lim, S. Fabrication of long-term stable superoleophobic surface based on copper oxide / cobalt oxide with micro-nanoscale hierarchical roughness Applied Surface Science Fabrication of long-term stable superoleophobic surface based on copper oxide / cobalt oxide w. *Appl. Surf. Sci.* **328**, 296–305 (2019).

28. Mansouri, B., Maleki, A. and Johari, S. A. Effects of cobalt oxide nanoparticles and cobalt ions on gill histopathology of zebrafish (Danio rerio). *Aquacult. Aquarium Conserv. Legis.* **8**, 438-444 (2015).

29. Saeed, S., Rafiq, M., Baloach, Q.U.A., Naqvi, S.H.A., Tahira, A., Khain, H., Hullio, A.A., Mallah, A.B., Willander, M., Akhtar, M. and Ibupoto, Z.H. Vanillin Assisted Synthesis of Co3O4 Nanostructures for the Development of Sensitive and Selective Peptone Biosensor. *Sensor Letters*. **15**, 536-544 (2017).

30. Ou, T., Yan, J., Xiao, C., Shen, W., Liu, C., Liu, X., Han, Y., Ma, Y. and Gao, C. Visible light response, electrical transport, and amorphization in compressed organolead iodine perovskites. *Nanoscale.* **8**, 11426–11431 (2016).

31. Schwartz, J., Perez, J. and Mo, Y. Growth and Characterization of Wide Band Gap Semiconductors (Zinc Oxide , Zinc Sulfide). *Thin Solid Films.* **2007**, B6-008 (2007).

32. Xing, L. and Xue, X. High gas sensing performance of one-step-synthesized Pd-ZnO nanoflowers due to surface reactions and modifications reactions and modifications. *Nanotechnology.* **22**, 215501 (2015)

33. Thakur, S. and Mandal, S. K. Morphology engineering of ZnO nanorod arrays to hierarchical nanoflowers for enhanced photocatalytic activity and antibacterial action against Escherichia coli. *New J. Chem*. **44**, 11796-11807 (2020).

34. Mi, Y., Zhang, X., Yang, Z., Li, Y., Zhou, S., Zhang, H., Zhu, W., He, D., Wang, J. and Van Tendeloo, G. Shape selective growth of single crystalline MnOOH multipods and 1D nanowires by a reductive hydrothermal method. *Mater. Lett.* **61**, 1781–1784 (2007).

35. Shao, L., Zhao, Q. and Chen, J. MnOOH nanorods as high-performance anodes for sodium ion batteries. *Chem. Commun.* **53**, 2435–2438 (2017).

36. Mugheri, A.Q., Tahira, A., Sherazi, S.T.H., Abro, M.I., Willander, M. and Ibupoto, Z.H. An amperometric indirect determination of heavy metal ions through inhibition of glucose oxidase immobilized on cobalt oxide nanostructures. *Sens. Lett.* **14**, 1178–1186 (2016).

37. Munawar, T., Mukhtar, F., Nadeem, M.S., Riaz, M., ur Rahman, M.N., Mahmood, K., Hasan, M., Arshad, M.I., Hussain, F., Hussain, A. and Iqbal, F. Novel photocatalyst and antibacterial agent; direct dual Z-scheme ZnO–CeO2-Yb2O3 heterostructured nanocomposite. *Solid State Sci.* **109**, 106446 (2020).

38. Luo, X.F., Wang, J., Liang, Z.S., Chen, S.Z., Liu, Z.L. and Xu, C.W. Manganese oxide with different morphology as efficient electrocatalyst for oxygen evolution reaction. *Int. J. Hydrogen Energy.* **42**, 7151–7157 (2017).

39. Santos, R. S., Suresh Babu, R., Devendiran, M., Haddad, D. B. and de Barros, A. L. F. Facile synthesis of transition metal (M = Cu, Co) oxide grafted graphitic carbon nitride nanosheets for high performance asymmetric supercapacitors. *Mater. Lett.* **308**, 131156 (2022).

CHAPTER 5

Part I

NANOSTRUCTURES AS ELECTROCATALYSTS FOR THE ELECTROCHEMICAL DETECTION OF FLUTAMIDE, BICALUTAMIDE AND HYDOXYFLUTAMIDE

5.1 Introduction

This chapter is based on the electrochemical detection of flutamide (FLU), bicalutamide (BIC) and hydroxyflutamide (OHF) using manganese and cobalt oxide nanostructures (MnONSs and CoONSs) and ytterbium nanorods (YbNRs) as electrocatalysts. The pH of the phosphate buffer solution (PBS) was optimised in this chapter because the Metal Oxide (MO). NSs were exposed to the solution after forming the nanocomposite as they decorated the nanorods (NRs). In this chapter, solutions of MnONSs, YbNRs and CoONSs were drop casted on the surface of glassy carbon electrodes (GCE) to modify them to MnO/GCE, YbNRs/GCE and CoO/GCE sensors. The fabricated sensors were then characterised in ferricyanide solutions to determine the molecule film on the surfaces of the modified electrodes. It was discovered that both MnONSs, YbNRs and CoONSs form a multilayer molecule film on the surface of the electrode. The processes on the MnO/GCE, YbNRs/GCE and CoO/GCE electrodes were diffusion-controlled, as discovered through scan rate studies. The MnO/GCE, YbNRs/GCE and CoO/GCE sensors showed ability to detect FLU, BIC and OHF through concentration studies. Stability studies at MnO/GCE and CoO/GCE proved the stability of the sensors in solutions of FLU, BIC and OHF. Both MnO/GCE, YbNRs/GCE and CoO/GCE displayed good selectivity of MnO/GCE, YbNRs/GCE and CoO/GCE in the detection of FLU, BIC and OHF. Spiked sample analysis showed good recoveries at MnO/GCE, YbNRs/GCE and CoO/GCE.

5.2 Electrochemical properties of Nanostructures as electrocatalysts

5.2.1 Characterisation of the fabricated electrochemical sensors

Characterisation of the modified electrodes was achieved through CV in a system consisting of $K_3Fe_3(CN)_6$ (1 mM), $K_4Fe(CN)_6$ (1 mM) and KCl (0.1 M). The CVs of the unmodified GCE (Bare GCE) and the modified GCE (MnO/GCE, CoO/GCE and YbNRs/GCE) are shown in **Fig. 5.1A**, **B** and **C.** The resultant voltammograms were

used to monitor the electron transfer efficiency in terms of peak-to-peak separation (ΔE_p). The ΔE_p values for the modified electrodes were calculated and listed in **Table 5.1.** The lowest ΔE_p value indicates better electron transfer; thus, Bare GCE had a better electron transfer than MnO/GCE (0.22 V), CoO/GCE (0.25 V) and YbNRs/GCE (0.36 V). Lower electron transfer suggests hindrance on the electrode surface due to the adsorption of the electrocatalyst material [1]. Surface roughness of GCE before and after modification is among the most important factors contributing to the differences in ΔE_p values [2]. Consequently, Eqns. 3.1-3.4, which were discussed in Chapter 3, were applied on $K_3Fe_3(CN)_6/K_4Fe(CN)_6$ redox system to determine the surface roughness factors (Γ) of the modified electrodes. The Γ values for the modified electrodes less than 1 $\times 10^{-10}$ mol cm^{-2} are reported to imply a monolayer molecule film of the material on the electrode surface[3]. As can be seen in **Table 5.1**, the Γ values for the electrodes modified with metal oxide NSs are greater than 1 $\times 10^{-10}$ mol cm^{-2} and increase in the following order: CoO/GCE< MnO/GCE< YbNRs/GCE. These Γ values for MnO/GCE, CoO/GCE and YbNRs/GCE suggest a multilayer metal oxide molecule film on the electrode surface [4]. The surface area of the electrodes determined in **Table 5.1** was determined using equation 3.1 provided in chapter 3.

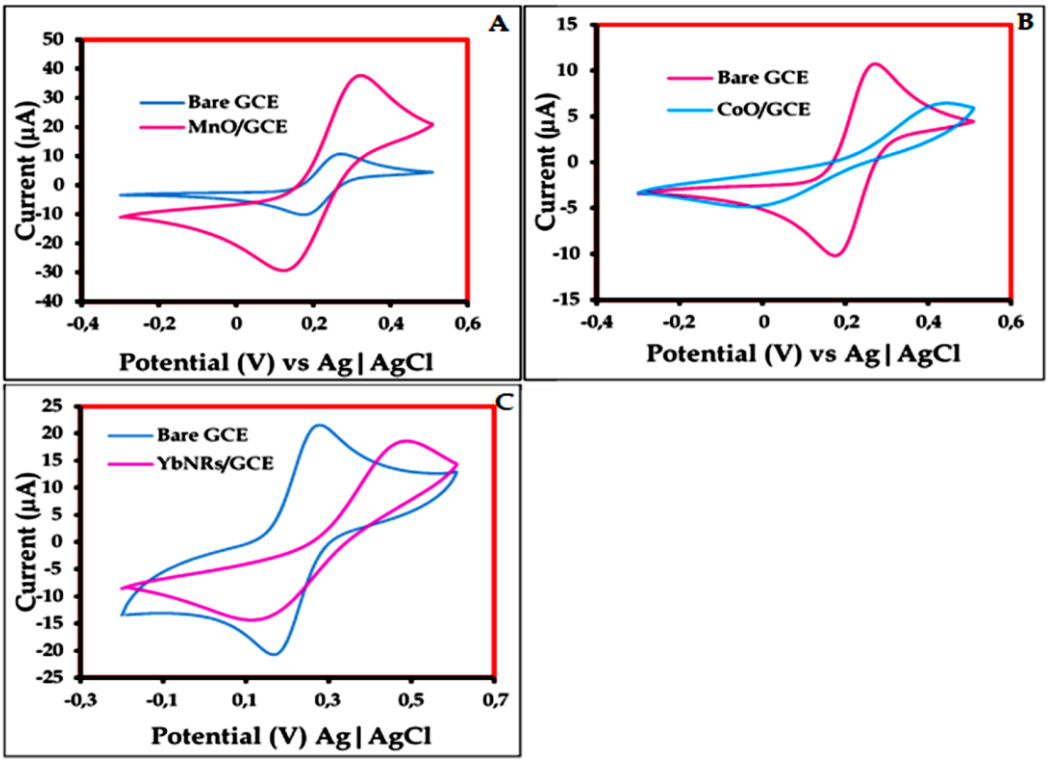

Fig. 5.1: Cyclic voltammograms (CVs) of (A) Bare GCE in comparison to MnO/GCE; (B) Bare GCE versus CoO/GCE; (C) Bare GCE versus YbNRs/GCE in ferricyanide solution.

Table 5.1. Electrochemical parameters of MnO/GCE and CoO/GCE based on both anodic (I_{pa}, E_{pa}) and cathodic (E_{pc}) signatures in PBS (pH 5)

Electrode	I_{pa} (μA)	ΔE_p (V vs Ag|AgCl)	Real electrode area (cm^2)	Γ (mol cm^{-2})
Bare GCE	12.50	0.09	-	-
MnO/GCE	37.10	0.22	1.60	1.46×10^{-9}
CoO/GCE	5.115	0.25	0.275	5.02×10^{-9}
YbNRs/GCE	18.2	0.36	0.296	5.50×10^{-9}

5.2.2 Optimisation of parameters

In order to determine the working conditions, square wave voltammetry (SWV) was employed to establish the optimal conditions for the fabricated electrochemical sensors in the electrolyte solutions of different pH values. This is because the electrolyte solution's pH significantly influences the electrochemical process of any electroactive molecule at the surface of the electrode[5]. The influence of pH was investigated in FLU(1 mM) electrolyte solutions (PBS) at pH 3, pH 5, pH 7, pH 9 and pH 12 to establish which pH was best suitable for studying the solutions of FLU, BIC and OHF. As shown in **Fig. 5.2**, the peak potential was shifted with the change in pH for both MnO/GCE and CoO/GCE electrode sensors. **Fig. 5.2A** shows a better response in terms of peak current for pH 5 and 7 at MnO/GCE compared to those observed at pH 3, pH 9 and pH 12. pH studies were then repeated for CoO/GCE to evaluate which pH between pH 5 and pH 7 would respond better, as shown in **Fig. 5.2 B**. CoO/GCE was behaving better at pH 5 than at pH 7. Thus, an electrolyte of pH 5 was employed for further studies. The calibration curves of pH against oxidation peak current at MnO/GCE and CoO/GCE are shown in **Fig. 5.2C** and **D**, respectively. These calibration curves show the direction shift of the peak potentials at different pH.

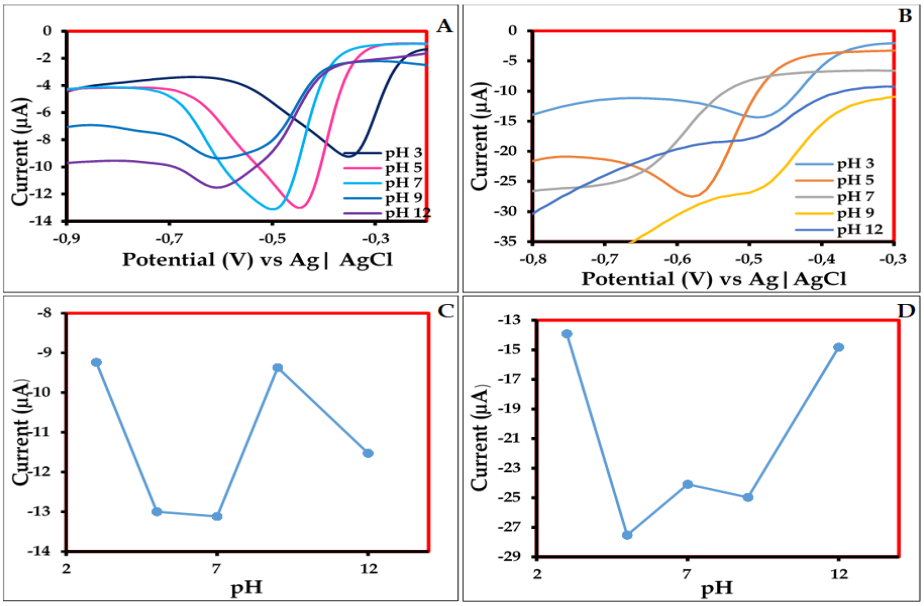

Fig. 5.2: SWVs for 1 mM FLU on (A) surface of MnO/GCE and (B) CoO/GCE in PBS at pH 3, pH 5, pH 7, pH 9 and pH 12 and Corresponding calibration plot of pH vs anodic peak current at (C) MnO/GCE and (D) CoO/GCE.

5.2.3 Influence of the scan rate

The influence of the scan rate on the electrochemical redox performances of FLU, BIC and OHF at MnO/GCE was studied using CV. This was performed at constant analyte concentration (1 mM) in PBS (pH 5) from 10 mV/s to 100 mV/s. **Fig. 5.3A, B and C** show the cathodic peak currents of FLU, BIC, and OHF at different scan rates, while their corresponding linear relationship plots are depicted in **Fig. 5.3D, E and F**, respectively. The linear relationships are expressed as the plots of peak currents vs the scan rates' square roots. As shown in **Fig. 5.3A, B and C**, the cathodic peak currents continuously increased as the scan rate increased for all analytes. It was observed during the FLU study that reduction processes are occurring at each scan around -0.67V vs Ag|AgCl, as illustrated in **Fig. 5.3A**. The cathodic peak currents represent the direct reduction of FLU to hydroxylamine and have no catalytic anodic peak current observed. Thus, this behaviour indicates that the reduction process is irreversible [5]. The same irreversible process was also observed for BIC and OHF at -0.73 V vs Ag|AgCl and -0.75 V vs Ag|AgCl, respectively, as indicated in **Fig. 5.3C** and **E**. The mechanisms of reduction of FLU, BIC and OHF are shown in **Fig. A1**. As can be observed in **Fig. 5.3D, E** and **F**, the peak currents are linearly proportional to the square roots of the scan rates. The correlation coefficients (R^2) were 0.9931, 0.9634

and 0.9976 for the reduction processes of FLU, BIC and OHF, respectively. These linear relationships denote the diffusion-controlled processes at the surfaces of modified electrodes[6]. The diffusion-controlled electrode processes occur if the spontaneous transfer of the electroactive species is from regions of higher concentrations to regions of lower concentrations[7]. This is seen by a directly proportional relationship between the scan rate's current and the square root.

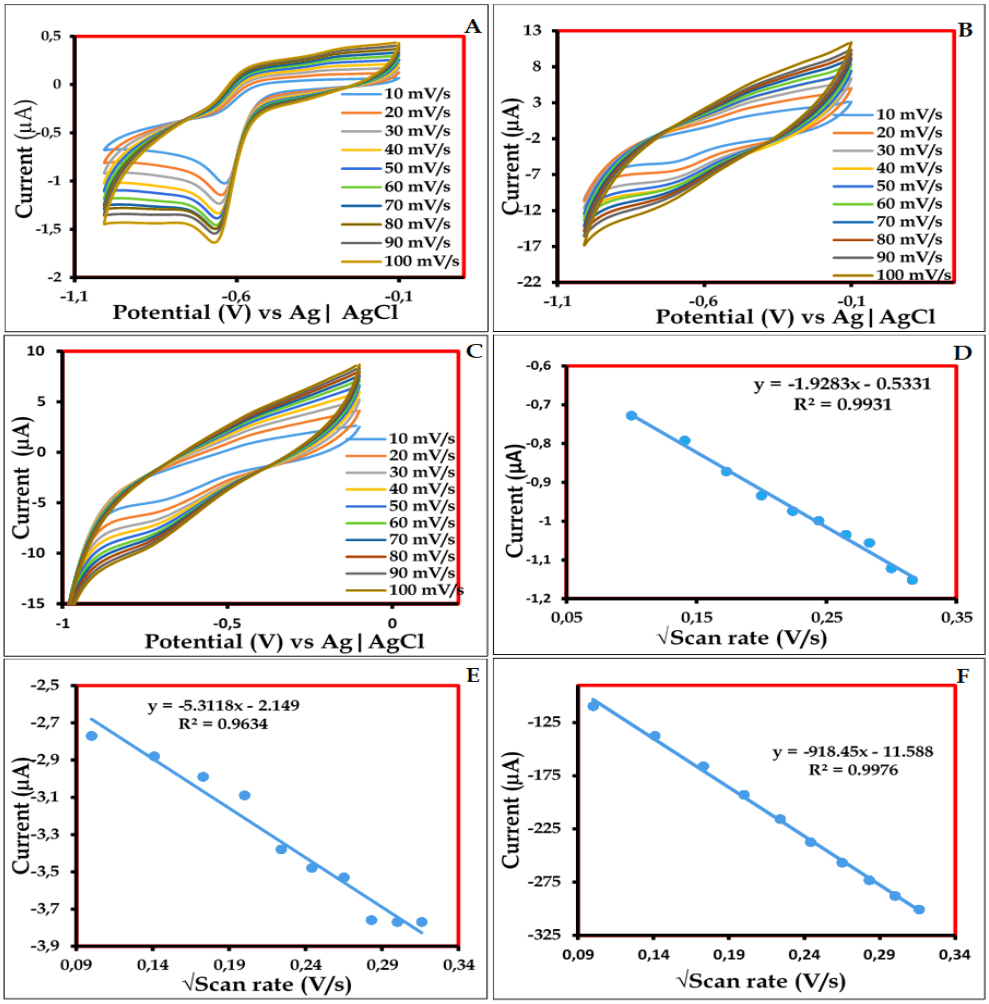

Fig. 5.3: CVs of scan rate variations of (A) FLU, (B) BIC, and (C) OHF for MnO/GCE recorded at different scan rates (10 – 100 mV/s) and the corresponding linear relationship plots (D, E and F respectively).

The effect of scan rate on the redox performances of FLU, BIC and OHF was also studied at CoO/GCE. **Fig. 5.4A**, **B** and **C** show reduction processes occurring at each scan for FLU, BIC and OHF. No oxidation process occurred at the surface of CoO/GCE for FLU, BIC and OHF. Therefore, this behaviour indicates that the reduction processes are irreversible. The mechanisms of reduction of FLU, BIC and OHF are

depicted in **Fig. A1**. **Fig. 5.4D, E** and **F** show that the peak currents are linearly proportional to the square roots of the scan rates. The R^2 values were 0.9899, 0.9914 and 0.9853 for the reduction processes of FLU, BIC and OHF (**Fig. 5.4 D, E** and **F**). These linear relationships denote diffusion-controlled processes at the surfaces of CoO/GCE.

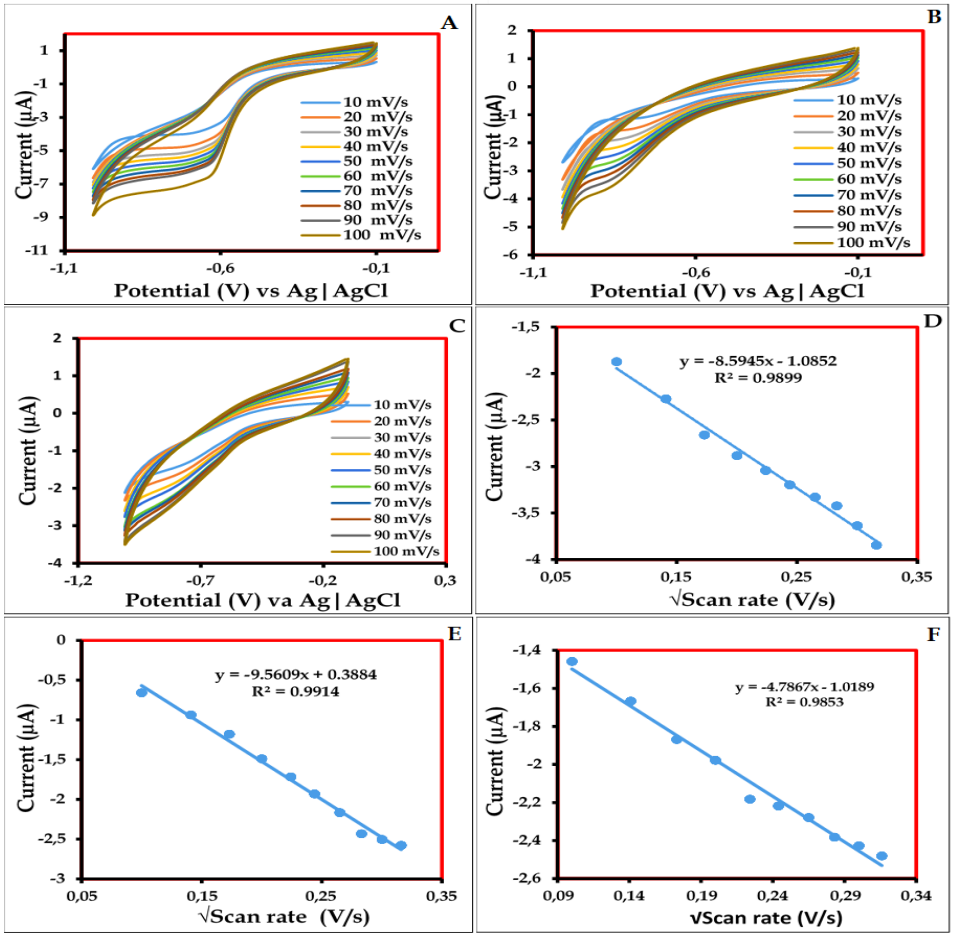

Fig. 5.4: CVs of scan rate variations of (A) FLU, (B) BIC, and (C) OHF for CoO/GCE recorded at different scan rates (10 – 100 mV/s) together with their corresponding linear relationship plots (D, E and F respectively).

The mechanical and kinetic electrocatalytic redox processes of FLU, BIC and OHF were investigated at the surface of YBNRs/GCE. This was done by varying the scan rates from 10 to 100 mV/s at constant analyte concentration (1 mM) in PBS (pH 5) using CV, as shown in **Fig. 5.5.** It was observed that the peak currents increased with an increase in scan rates (**Fig. 5.5A, B** and **C**). This means that the peak currents are dependent and proportional to scan rates. The corresponding linear relationship plots of the scan rate variations were plotted using peak currents vs the scan rates' square

roots. As shown in **Fig. 5.5D**, **E** and **F**, the anodic peak currents were linearly corresponding with the square roots of scan rates. This relationship denotes a diffusion-controlled process on the surface of the modified electrode[8]**.** Diffusion-controlled are denoted by a directly proportional relationship between the square roots of the scan rates and the peak currents.

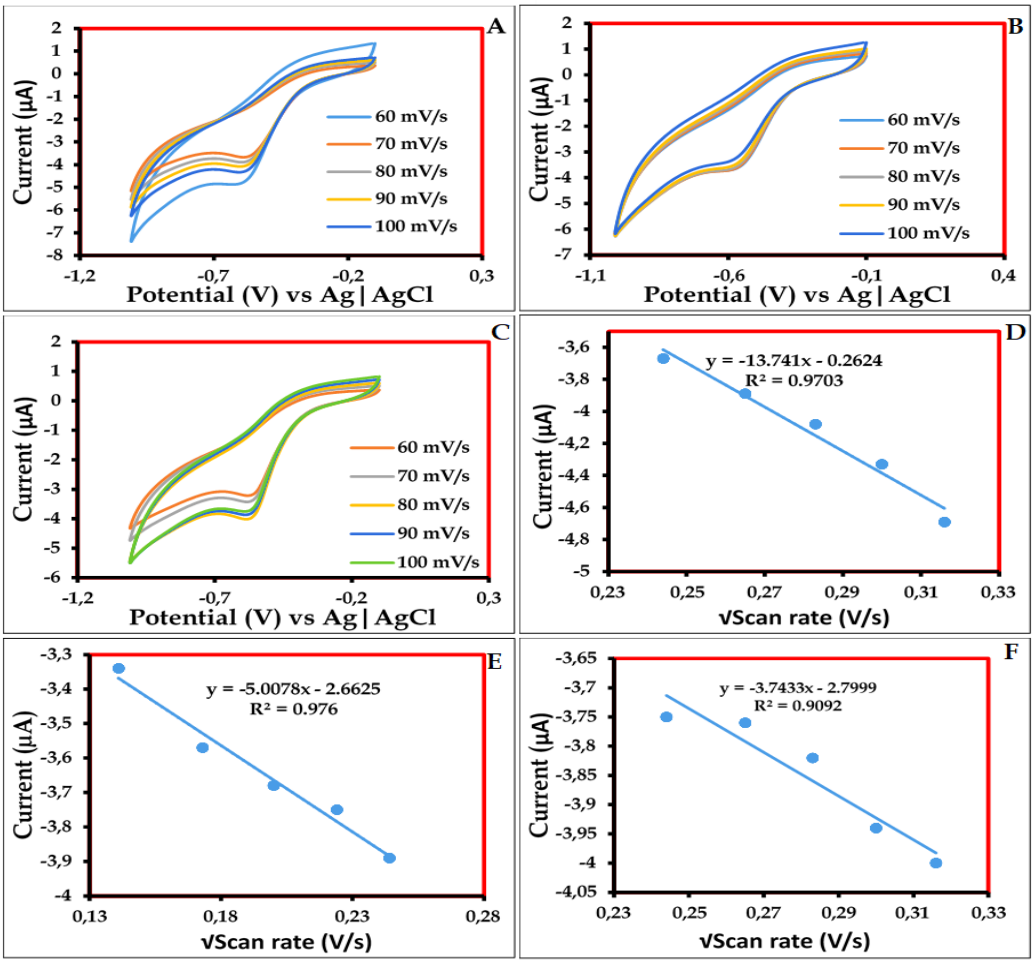

Fig. 5.5: CVs of scan rate variations (10 - 100 mV/s) of (A) FLU, (B) BIC, (C) OHF and their corresponding linear relationships (D, E and F) respectively at YbNR/GCE.

5.2.4 Concentration studies

Concentration studies were performed to investigate the electrochemical performance of MnO/GCE for the detection and quantification of FLU, BIC and OHF using square wave voltammetry (SWV), as shown in **Fig. 5.6**. Concentration variations of each analyte were analysed to establish the analytical parameters such as limit of detection (LOD) and limit of quantification (LOQ) as shown in **Fig. 5.6A, B** and **C**. The analysis was performed at concentration ranges between 32.01 and 50.00 µM in PBS at a scan

rate of 100 mV/s with serial dilution performed from 50 µM to 32.01 µM. As the concentration of FLU, BIC, and OHF decreased, the reduction peak current decreased. This indicates that MnO/GCE electrode sensor detected the analytes successfully. The resultant peak currents were plotted against concentration to obtain a linear plot and are shown in **Fig. 5.6D, E** and **F**. The linear relationship plots were then used to calculate the LODs and LOQs of the MnO/GCE electrode sensor. The obtained LOD values were 18.5 µM, 13.0 µM and 18.8 µM for FLU, BIC and OHF, respectively (estimated using **Eqn 3.5** discussed in Chapter 3). The LOD values in this study are comparable to those reported in the literature as provided in **Table 5.2**. The LODs are relatively poor than what is reported in literature and this may be due to matrix effects and interferences, electrocatalysts used or sensitivity of instrument and its noise level[9]. The LOQs for FLU, BIC and OHF are 81.8 µM, 43.2 and 25.8 µM, respectively (estimated from the **Eqn 3.6** discussed in Chapter 3).

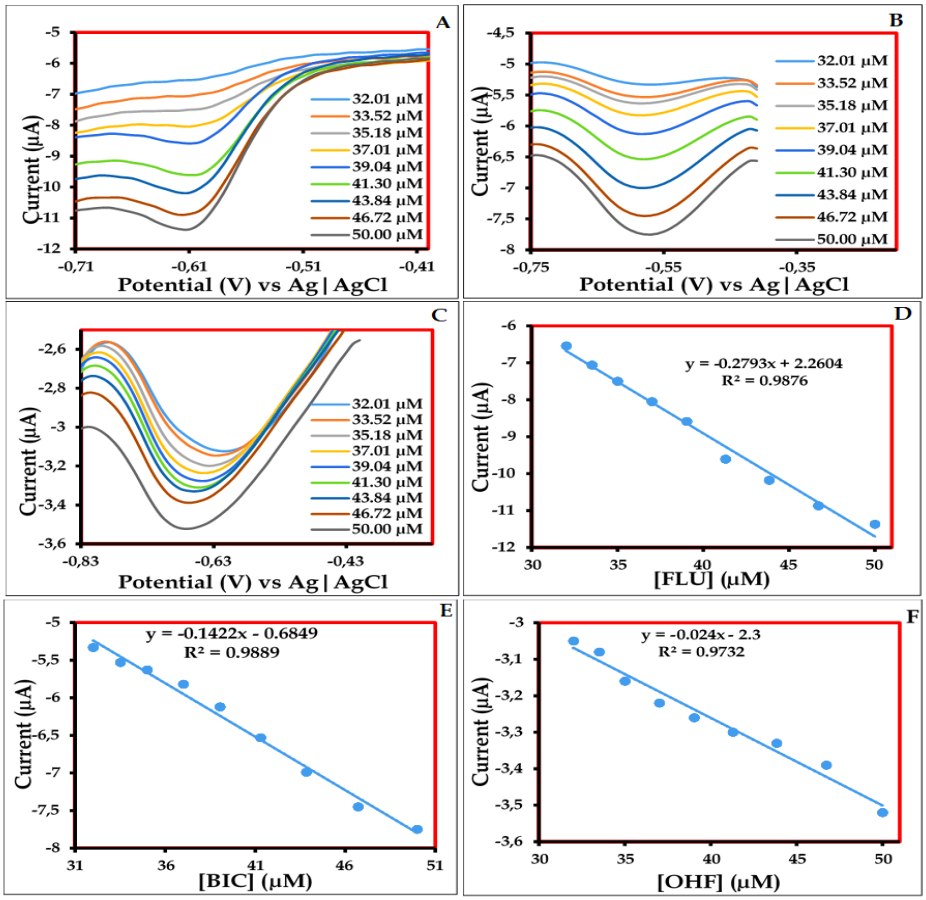

Fig. 5.6: SWVs of (A) FLU, (B) BIC, (C) OHF at different concentrations (32.01 – 50 µM) and their corresponding linear relationship plots (D, E and F) for MnO/GCE.

Table 5.2. Analytical parameters of FLU, BIC and OHF at MnO/GCE and CoO/GCE, respectively.

Analyte	Modified electrode	Limit of detection (µM)	Linearity range (µM)	Sample type	Electroanalytical techniques	Ref.
FLU	nano-Ag/MGCE	9.33	10 – 1000	Human urine	DPV	[10]
	AuE	1.8	6 - 60	-	DPV	[11]
	BDDE	0.42	0.99 - 42.9	Tablets, human urine, river, well and tap water	DPV and SWV	[12]
	MoS_2-CZO/GCE	0.005	0.019 - 668.5	River water and human urine	DPV	[13]
	SF-CTAB	0.007	0.016 - 658.51	human blood serum and tap water	DPV	[14]
	β-$Cu_2V_2O_7$/PC/RDGCE	0.62	30 - 240	Human Urine, human blood serum and River water	Amperometric (i-t)	[15]
	GC_{ox}	0.000016	0.00005 - 0.0006	-	CV	[16]
	ZMNS/GCE	0.033	0.1 - 73; 111 - 1026	-	DPV	[17]

	MnO/GCE	18.5	32.01 - 50.00	Tap water	SWV	This work
	CoO/GCE	18.8	32.01 - 50.00	Tap water	SWV	This work
	YbNRs/GCE	18.7	32.01 - 50.00	Tap water	SWV	This work
BIC	SWCNT/CPE	0.005	0.01 - 1	Human Urine, human blood serum	DPV	[18]
	SrMoO4-MRs/GCE	0.0012	0.01 - 304.8	Human blood serum and human urine	DPV	[19]
	MnO/GCE	13.0	32.01 - 50.00	Tap water	SWV	This work
	CoO/GCE	18.7	32.01 - 50.00	Tap water	SWV	This work
	YbNRs/GCE	18.5	32.01 - 50.00	Tap water	SWV	This work
OHF	MnO/GCE	78.8	32.01 - 50.00	Tap water	SWV	This work
	CoO/GCE	18.5	32.01 - 50.00	Tap water	SWV	This work
	YbNRs/GCE	19.3	32.01 - 50.00	Tap water	SWV	This work

The results on the dependence of the peak current on the concentration variations of FLU, BIC and OHF on CoO/GCE are shown in **Fig. 5.7A, B** and **C**. The peak current increased correspondingly with the increase in analyte concentrations due to the reduction of FLU, BIC, and OHF. This indicates that the CoO/GCE electrode sensor is responsive to various concentrations of your analytes. The sharp reduction peaks represent an effective nitro group reduction in FLU [20]. The linear plots were then determined from the peak currents and concentrations of analytes and used to determine LODs and LOQs, as shown in **Fig. 5.7D, E** and **F**. The concentration of FLU, BIC, and OHF was directly proportional. The LODs of FLU, BIC and OHF are 18.8 µM, 18.7 µM and 18.5 µM, respectively. The LODs being relatively poor may be a result of matrix effects and interferences, electrocatalysts used or sensitivity of instrument and its noise level[9]. In addition, the LOQs of FLU, BIC and OHF are 82.0 µM, 81.8 µM and 81.8 µM, respectively. The LODs in this study are comparable with those reported in the literature as produced in **Table 5.2**.

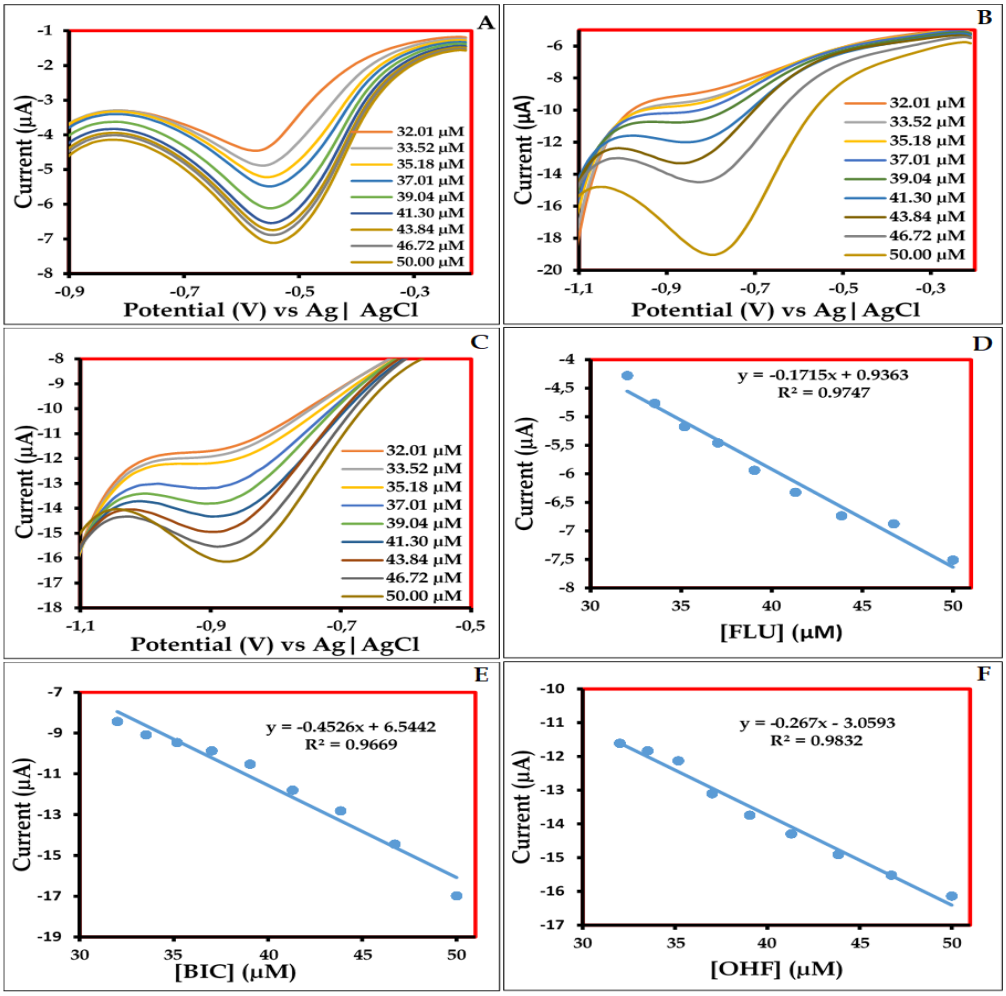

Fig. 5.7: SWVs of different concentrations of (A) FLU, (B) BIC, (C) OHF and their corresponding linear relationship plots (D, E and F) for CoO/GCE

The electrochemical performance of YBNRs/GCE towards detecting and quantifying FLU, BIC and OHF was also evaluated using SWV, as shown in **Fig. 5.8A**, **B** and **C**. As the concentration of the analytes increased, the reduction peak current also increased. This shows that YbNRs/GCE electrode sensor detected the analytes successfully[21]. The corresponding linear relationship plots for current vs analytes concentration were also determined as shown in **Fig. 5.8D, E** and **F**. It was observed that the concentration of analytes was directly proportional to the peak current. The LODs of FLU, BIC and OHF were calculated and found to be 18.7 µM, 18.5 µM and 19.3 µM, respectively. LOQs for FLU, BIC and OHF were calculated and obtained to be 62.5 µM, 61.7µM and 64.4 µM, respectively. The LODs at YbNRs/GCE are comparable to those in the literature, as provided in **Table 5.2**.

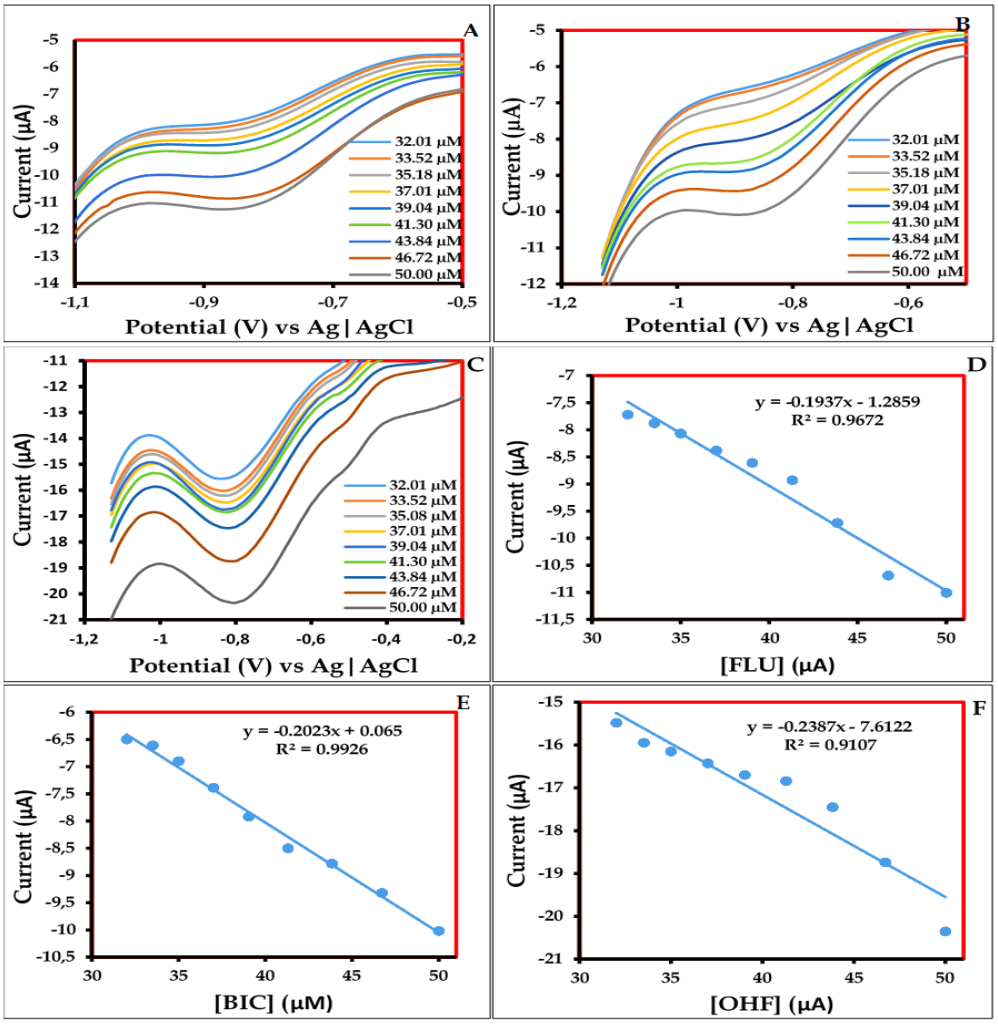

Fig. 5.8: SWVs of different concentrations (32.01 - 50.00 µM) of (A) FLU, (B) BIC, (C) OHF and their corresponding linear relationship plots of current vs analyte concentration (D, E and F respectively) at YbNRs/GCE.

5.2.5 Stability studies

The stability of both MnO/GCE, CoO/GCE, and YbNRs/GCE electrode sensors was studied in solutions of FLU (1 mM), BIC (1 mM), and OHF (1 mM) in PBS by running 9 scans at 100 mV/s. **Fig. 5.9A, B** and **C** show the CVs obtained from MnO/GCE for the FLU, BIC, and OHF, respectively. The cathodic peak currents for FLU were observed at -0.6V vs Ag|AgCl, while for BIC and OHF were -0.7 V vs Ag|AgCl at MnO/GCE, respectively. Similarly, the CVs for FLU, BIC, and OHF obtained from CoO/GCE are presented in **Fig. 5.9D, E** and **F**. The cathodic peak currents for FLU, BIC and OHF were observed at 0.57 V vs Ag|AgCl, 0.85 V vs Ag|AgCl and 0.8 V vs Ag|AgCl, respectively. As shown in **Fig. 5.9A**, **B** and **C**, the cathodic peak currents for FLU, BIC and OHF were observed at -0.54V vs Ag|AgCl. As can be observed from **Fig. 5.9**, both the cathodic peak currents and potentials remain almost unchanged. This electrocatalytic redox behaviour showed that MnO/GCE, CoO/GCE, and YbNRs/GCE have good stability. There is only negligible variation in peak current for both analytes at both electrode sensors. Thus, it can be concluded from these Figures that both MnO/GCE, CoO/GCE, and YbNRs/GCE were stable in all electrolyte solutions.

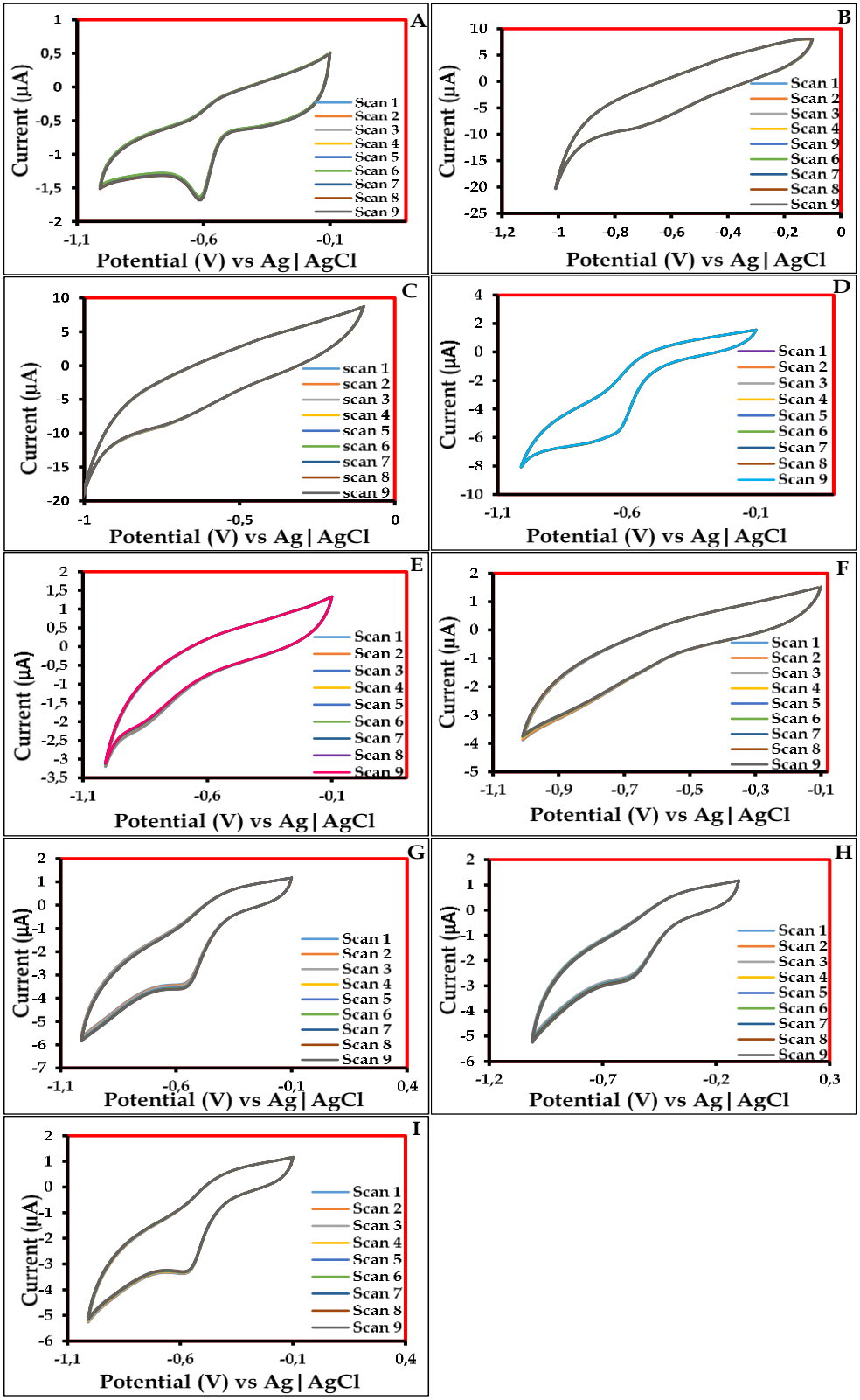

Fig. 5.9: Stability scans at MnO/GCE for (A) FLU, (B) BIC, (C) OHF; at CoO/GCE for (D) FLU, (E) BIC, (F) OHF; at YbNRs/GCE (G) FLU, (H) BIC, (I) OHF.

5.2.6 Interference studies

Square wave voltammetry was used to study the selectivity of MnO/GCE for FLU, BIC and OHF in the presence of different interferents. Interfering agents used in this study are Ca^{+}, Pb^{2+}, Mg^{2+}, K^{+}, and Na^{+}. The effects of these interferences were studied at solutions of FLU (1 mM), BIC (1 mM) and OHF (1 mM) and 1 mM of each interferent, respectively. As can be seen in **Fig. 5.10A, B and C**, the interfering species did not affect the potential of the peak currents at MnO/GCE. The interfering species also did not affect the peak current intensity as the peaks are almost of the same current. The bar graphs and error bars in **Fig. 5.8D, E and F** also show that the change in peak current is very minimal. Thus, the inferring species do not interfere with the electrochemical sensing of FLU, BIC and OHF at MnO/GCE. . The reproducibility of MnO/GCE was evaluated by repeatedly using the electrode for five times for each analyte. The resulting RSD values were calculated to be 1.81, 1.94 and 4.50% for FLU, BIC and OHF, respectively. These RSD values confirm that MnO/GCE has high reproducibility.

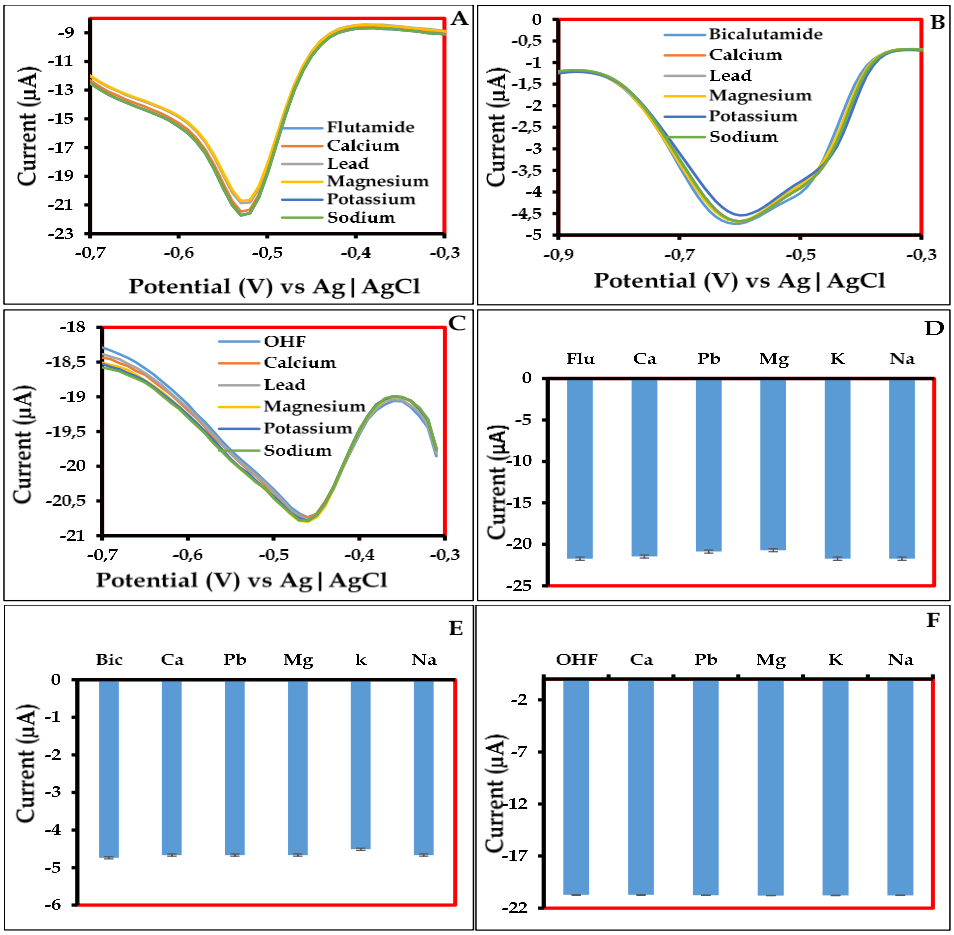

Fig. 5.10: SWVs of (A) FLU, (B) BIC and (C) OHF in the presence of interfering species and the corresponding bar graphs (D), (E) and (F), respectively, at MnO/GCE.

The selectivity of CoO/GCE for FLU, BIC and OHF was also studied in the presence of Ca^{+}, Pb^{2+}, Mg^{2+}, K^{+} and Na^{+}. As evident in **Fig. 5.11A, B and C**, the peak potential and the peak current intensity were not affected by the interfering species as the peaks are almost of the same current. The bar graphs and error bars in **Fig. 5.11D, E and F** also show that the change in peak current is very minimal. Thus, the inferring species do not interfere with the electrochemical sensing of FLU, BIC and OHF at CoO/GCE. Further, the reproducibility of CoO/GCE was evaluated by using the electrode 5 times repeatedly for FLU, BIC and OHF. The RSD values were then calculated to 3.64, 0.17 and 7.82% for FLU, BIC and OHF, respectively. These RSD values confirm that CoO/GCE has good reproducibility.

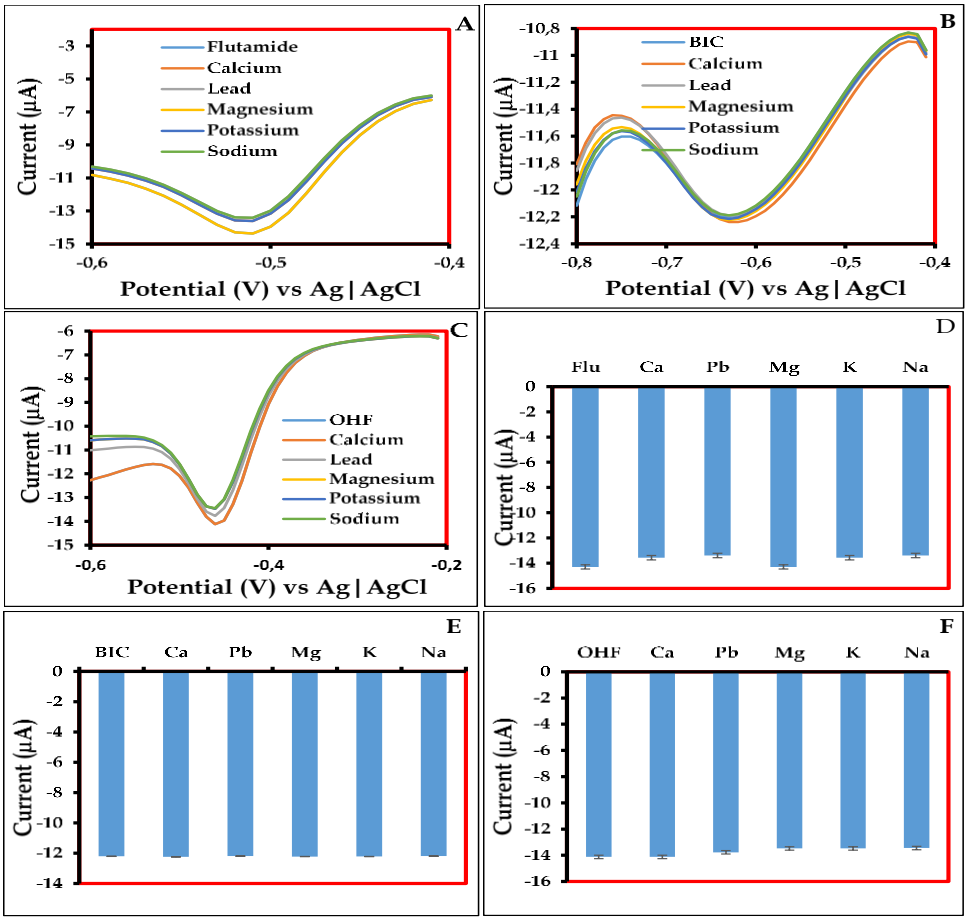

Fig. 5.11: SWVs of (A) FLU, (B) BIC, (C) OHF in the presence of interfering species and the corresponding bar graphs (D), (E) and (F), respectively, at CoO/GCE.

The selectivity of YbNRs/GCE was also studied in the presence of Ca^{+}, Pb^{2+}, Mg^{2+}, K^{+} and Na^{+}. From the results obtained in **Fig. 5.12A**, **B** and **C**, it is evident that no interferences were observed during the detection of FLU, BIC and OHF at YbNRs/GCE. The bar graphs and error bars in **Fig. 5.12D**, **E,** and **F** also show minimal changes. Thus, all the interfering compounds do not interfere with detecting FLU, BIC and OHF at YbNRs/GCE. Therefore, it can be concluded that YbNRs/GCE was not susceptive to the interference by all the interfering compounds used in this study; hence, the proposed electrode sensor was selective towards the detection of FLU, BIC and OHF. The reproducibility of YbNRs/GCE was also studied by using the electrode the electrode 5 times for the three analytes. The RSD values were calculated from the repetitions and found to be 0.17, 4.63 and 1.33% for FLU, BIC and OHF, respectively. These RSD values confirm that YbNRs/GCE has high reproducibility.

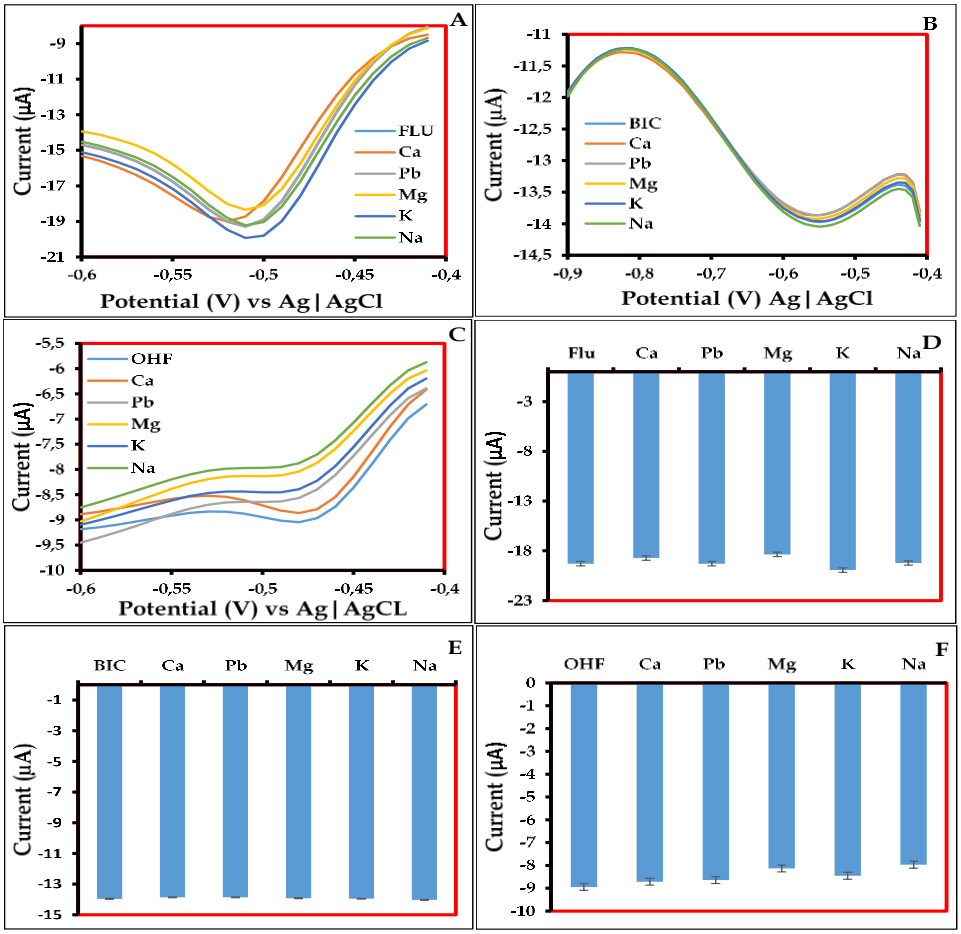

Fig. 5.12: SWVs of (A) FLU, (B) BIC, and (C) OHF in the presence of interfering species and the corresponding bar graphs (D), (E) and (F) respectively at YBNR/GCE.

5.2.7 Spiked sample analysis

Tap water obtained from synthesis laboratories at the University of South Africa was adjusted to pH 5 using NaH_2PO_4, Na_2HPO_4 and HCl. Furthermore, stock solutions of FLU (1 mM), BIC (1 mM) and OHF (1 mM) were prepared. The phosphate-treated tap water PBS solution was taken into a voltammetric cell, and its SWV was recorded. Known volumes of analyte solutions were added to the solution and recorded. **Fig. 5.13** shows the spiked sample analysis of the analytes of interest at a linear range of 1.40-9.82 µM, at pH 5 and a scan rate of 100 mV/s at MnO/GCE. **Fig. 5.13A**, **B** and **C** show the SWVs of the spiked sample analysis of FLU and BIC, respectively. As seen in the figures, the current increases with the concentration of each analyte. The potential in both **Fig. 5.13A**, **B** and **C** shifted slightly to the left, indicating dependence on concentrations. **Fig. 5.13E** displays SWVs showing the spiked sample analysis of OHF. As shown in the figure, the current increased with concentration. The obtained % recoveries were 95.1%, 99.29% and 100% for FLU, BIC and OHF, respectively. The RSD values ranged from 1.58 - 4.89%, as shown in **Table 5.3**. The recoveries show good accuracy of MnO/GCE in the detection of the analytes.

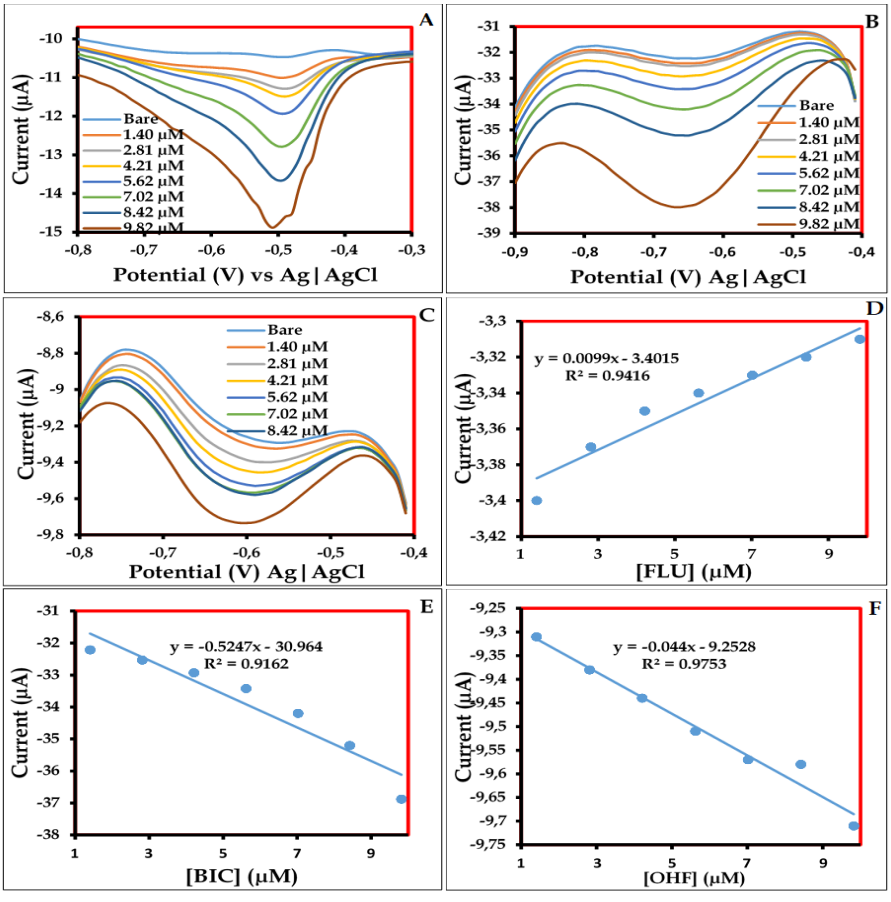

Fig. 5.13: SWVs of Spiked sample analysis of (A) FLU, (B) BIC, (C) OHF and their corresponding linear relationship plots D, E and F at MnO/GCE.

Spiked samples were also analysed at CoO/GCE for FLU, BIC and OHF. **Fig. 5.14** shows the spiked sample analysis of the analytes of interest at a linear range of 1.40-9.82 µM, at pH 5 and a scan rate of 100 mV/s at CoO/GCE. **Fig. 5.14 A**, **B** and **C** show the SWVs of the spiked sample analysis of FLU, BIC and OHF, respectively. From the figures, it can be seen that the peak current increased with an increase in the concentration of each analyte. The obtained % recoveries were 95.1%, 98.87% and 100% for FLU, BIC and OHF, respectively. The RSD values ranged from 5.69 - 23.00%, as provided in **Table 5.3**. The recoveries show good accuracy of CoO/GCE in the detection of the analytes.

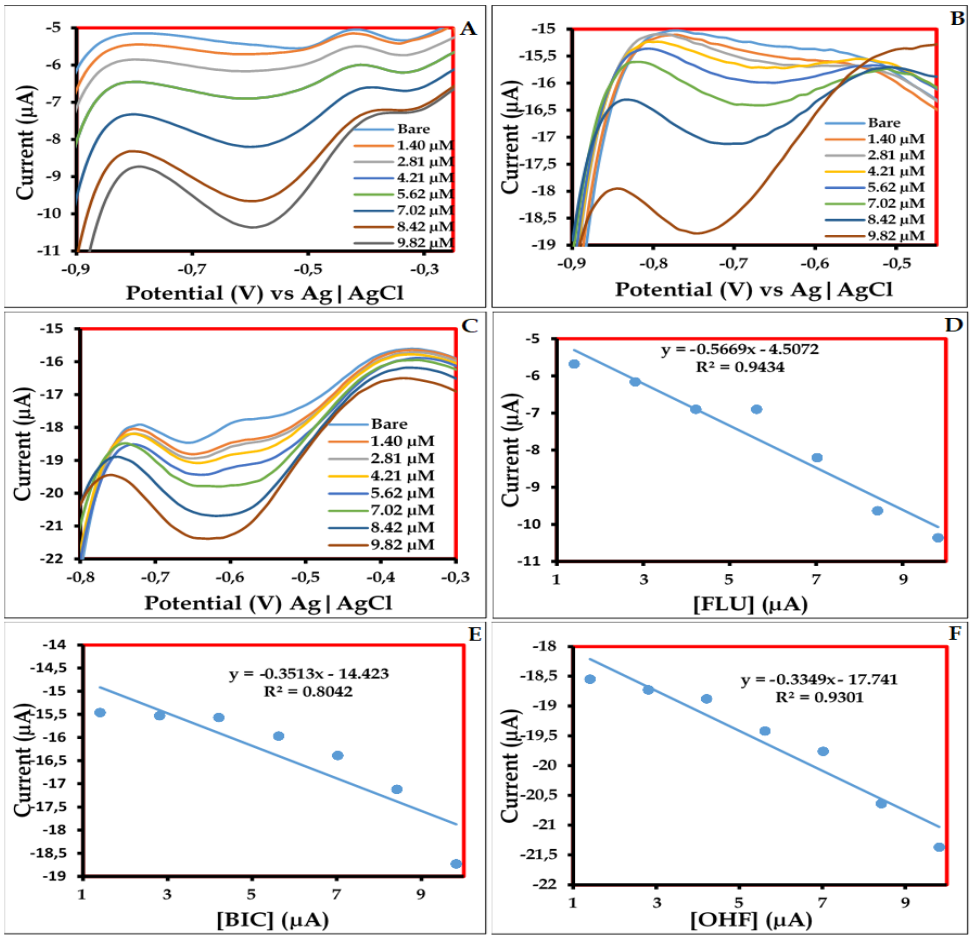

Fig. 5.14: SWVs of Spiked sample analysis of (A) FLU, (B) BIC, (C) OHF and their corresponding linear relationship plots D, E and F at CoO/GCE.

The Spiked sample analysis of FLU, BIC and OHF was also performed at YbNRs/GCE. **Fig. 5.15A**, **B** and **C** show the SWVs of the spiked sample analysis of FLU, BIC and OHF, respectively. As shown in the Figures, the current was increasing with the increase of concentration of each analyte. This shows that YbNRs/GCE is able to detect FLU, BIC and OHF even in spiked samples. The calibration method was also employed to quantify FLU, BIC and OHF in Spiked samples. **Fig. 5.15D, E** and **F** show the calibration of FLU, BIC and OHF, respectively. As can be seen in the Figures, the reduction peak currents are proportional to the concentrations. The obtained % recoveries were 90%, 99.28% and 94.71% for FLU, BIC and OHF, respectively. The RSD values ranged from 1.39 – 22.37%, as shown in **Table 5.3**. The recoveries show good accuracy of YbNRs/GCE in the detection of the analytes.

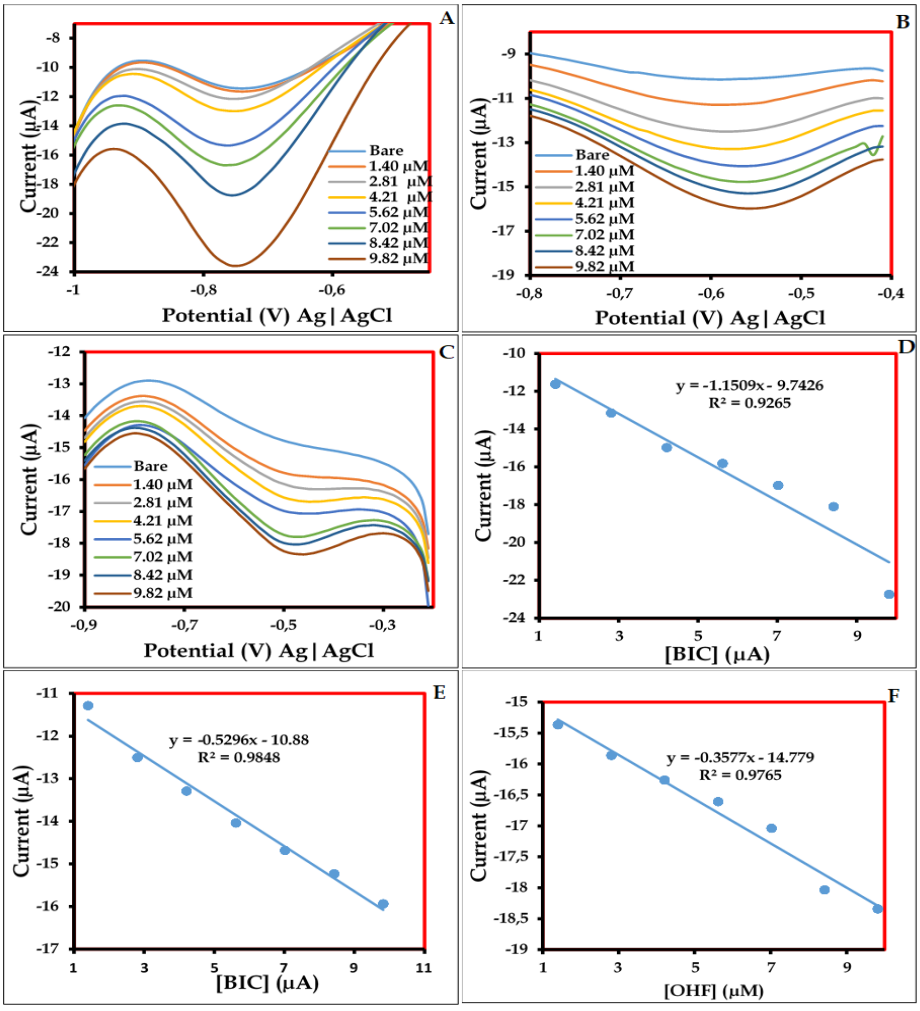

Fig. 5.15: SWVs of Spiked sample analysis of (A) FLU, (B) BIC, (C) OHF and their corresponding linear relationship plots D, E and F at YbNR/GCE.

Table 5.3. Comparison of % recoveries of FLU, BIC and OHF at MnO/GCE, CoO/GCE and YbNRs/GCE.

		MnO/GCE				CoO/GCE				YbNRs/GCE			
Analyte	Amount added (µL)	Expected conc. (µM)	Found conc. (µM)	Recovery (%)	RSD (%)	Expected conc. (µM)	Found conc. (µM)	Recovery (%)	RSD (%)	Expected conc. (µM)	Found conc. (µM)	Recovery (%)	RSD (%)
FLU	10	1.40	1.33 ± 0.03	95.1	2.40	1.40	1.33 ± 0.03	95.1	2.30	1.40	1.26 ± 0.03	90	2.23
BIC	10	1.40	1.39 ± 0.07	99.29	4.89	1.40	1.38 ± 0.10	98.87	7.22	1.40	1.39 ± 0.02	99.28	1.39
OHF	10	1.40	1.40 ± 0.02	100	1.58	1.40	1.40 ± 0.08	100	5.69	1.40	1.34 ± 0.09	94.71	6.54

Conclusion

Three simple sensors for detecting and quantifying FLU and its derivatives, BIC and OHF, were successfully developed. Both MnO/GCE, CoO/GCE and YbNRs/GCE showed excellent and efficient electrocatalytic activities through CV and SWV methods. The developed sensors also showed excellent practical feasibility through spiked sample analysis experiment which resulted in good recovery. Therefore, based on the relevant observations from this work, we can conclude that the MnO/GCE, CoO/GCE and YbNRs/GCE electrochemical sensors are reliable

References

1. Kar, P., Tatard, F., Lamblin, G., Banet, P., Aubert, P.H., Plesse, C. and Chevrot, C. Silver nanoparticles to improve electron transfer at interfaces of gold electrodes modified by biotin or avidin. *J. Electroanal. Chem.* **692**, 17–25 (2013).
2. Edward Sekhosana, K., Nkhahle, R. & Nyokong, T. Analytical Detection and Electrocatalysis of Paracetamol in Aqueous Media Using Rare-Earth Double-Decker Phthalocyaninato Chelates as Electrochemically Active Materials. *ChemistrySelect.* **5**, 9857–9865 (2020).
3. Sekhosana, K. E., Manyeruke, M. H. & Nyokong, T. Synthesis and optical limiting properties of new lanthanide bis- and tris-phthalocyanines. *J. Mol. Struct.* **1121**, 111–118 (2016).
4. Sekhosana, K. E., Shumba, M. & Nyokong, T. Electrochemical Detection of 4-Chlorophenol Using Glassy Carbon Electrodes Modified with Thulium Double-Decker Phthalocyanine Salts. *ChemistrySelect.* **4**, 8434–8443 (2019).
5. Karthik, R. *et al.* A facile graphene oxide based sensor for electrochemical detection of prostate anti-cancer (anti-testosterone) drug flutamide in biological samples. *RSC Adv.* **7**, 25702–25709 (2017).
6. Lin, W. J., Liao, C. S., Jhang, J. H. & Tsai, Y. C. Graphene modified basal and edge plane pyrolytic graphite electrodes for electrocatalytic oxidation of hydrogen peroxide and β-nicotinamide adenine dinucleotide. *Electrochem. commun.* **11**, 2153–2156 (2009).
7. Lin, C.S., Denton, E.B., Gaskill, H.S. and Putnam, G.L. Diffusion-controlled electrode reactions. *Ind. Eng. Chem.* **43**, 2136-2143 (1951).
8. Nkhahle, R., Sekhosana, K. E., Centane, S. & Nyokong, T. Electrocatalytic Activity of Asymmetrical Cobalt Phthalocyanines in the Presence of N Doped Graphene Quantum Dots: The Push-pull Effects of Substituents. *Electroanalysis* **31**, 891–904 (2019).
9. Chang, K.H. Limit of Detection and Its Establishment in Analytical Chemistry. *Health Env. J.* **2**, 38–43 (2011).
10. Ahmadi, F., Raoof, J.B., Ojani, R., Baghayeri, M., Lakouraj, M.M. and Tashakkorian, H. Synthesis of Ag nanoparticles for the electrochemical detection of anticancer drug flutamide. *Cuihua Xuebao/Chinese J. Catal.* **36**, 439–445 (2015).

11. Mehrabi, A., Rahimnejad, M., Mohammadi, M. & Pourali, M. Electrochemical detection of flutamide with gold electrode as an anticancer drug. *Biocatal. Agric. Biotechnol.* **22**, 101375 (2019).
12. Švorc, Ľ., Borovská, K., Cinková, K., Stanković, D. M. & Planková, A. Advanced electrochemical platform for determination of cytostatic drug flutamide in various matrices using a boron-doped diamond electrode. *Electrochim. Acta* **251**, 621–630 (2017).
13. Selvi, S.V., Nataraj, N., Chen, T.W., Chen, S.M., Nagarajan, S., Ko, C.S., Tseng, T.W. and Huang, C.C. In-situ formation of 2H phase MoS2/cerium-zirconium oxide nanohybrid for potential electrochemical detection of an anticancer drug flutamide. *Mater. Today Chem.* **23**, 100749 (2022).
14. Kesavan, G., Pichumani, M., Chen, S. M. & Ko, C. S. Surfactant-assisted (CTAB, PVA, PVP) thermal decomposition synthesis of strontium spinel ferrite nanocrystals for electrochemical sensing of cytostatic drug flutamide. *Mater. Today Chem.* **26**, 101045 (2022).
15. Musuvadhi Babulal, S., Anupriya, J. & Chen, S. M. Self assembled three dimensional β-Cu2V2O7 hierarchical flower decorated porous carbon: An efficient electrocatalyst for flutamide detection in biological and environmental samples. *Chemosphere* **303**, 135203 (2022).
16. Kassem, M. A., Al-zahrani, W. M., Althagafi, Z. T. & Mohammed, G. I. Electroanalysis of Flutamide as an Anticancer Drug at Electrochemically Activated Glassy Carbon Electrode. *Int. J. Electrochem. Sci.* **17**, 1–14 (2022).
17. Rajakumaran, R., Abinaya, M., Chen, S. M., Balamurugan, K. & Muthuraj, V. Ultrasonication and hydrothermal assisted synthesis of cloud-like zinc molybdate nanospheres for enhanced detection of flutamide. *Ultrason. Sonochem.* **61**, 104823 (2020).
18. Pandit, U. J., Khan, I., Wankar, S., Raj, K. K. & Limaye, S. N. Development of an electrochemical method for the determination of bicalutamide at the SWCNT/CPE in pharmaceutical preparations and human biological fluids. *Anal. Methods* **7**, 10192–10198 (2015).
19. Kogularasu, S., Akilarasan, M., Chen, S. M. & Sheu, J. K. Scalable and sustainable synthetic assessment between solid-state metathesis and sonochemically derived electrocatalysts (strontium molybdate) for the precise anti-androgen bicalutamide (Casodex^{TM}) detection. *Microchem. J.* **168**, 106465

(2021).

20. Manavalan, S., Rajaji, U., Chen, S.M., Selvin, S.S.P., Govindasamy, M., Chen, T.W., Ali, M.A., Al-Hemaid, F.M. and Elshikh, M.S. Determination of 8-hydroxy-2′-deoxyguanosine oxidative stress biomarker using dysprosium oxide nanoparticles@reduced graphene oxide. *Inorg. Chem. Front.* **5**, 2885–2892 (2018).

21. Mehrabi, A., Rahimnejad, M., Mohammadi, M. & Pourali, M. Electrochemical detection of Flutamide as an anticancer drug with gold nanoparticles modified glassy carbon electrode in the presence of prostate cancer cells. *J. Appl. Electrochem.* **51**, 597–606 (2021).

Part II

NANOCOMPOSITES AS ELECTROCATALYSTS FOR THE DETECTION OF FLUTAMIDE, BICALUTAMIDE AND HYDROXYFLUTAMIDE

5.3 Introduction

In Part II, the electrocatalysts used in Part I are combined to form two nanocomposites (NCs). The two NCs are ytterbium nanorods decorated with manganese and cobalt oxide nanostructures (YbNRs/MnONSs and YbNRs/CoONSs). Thes two NCs are employed as electrocatalysts for the electrochemical detection of flutamide (FLU), bicalutamide (BIC) and hydroxyflutamide (OHF). To conduct the studies, solutions of YbNRs/MnONSs and YbNRs/CoONSs were first drop casted on the surface of glassy carbon electrodes (GCE) to modify them to YbNRs/MnONSs/GCE and YbNRs/CoONSs/GCE sensors. The fabricated electrode sensors were then characterised in ferricyanide solutions to determine the molecule film on the surfaces of the modified electrodes. The observation was that both YbNRs/MnONSs and YbNRs/CoONSs form a multilayer molecule film on the surface of the electrode. The processes on both YbNRs/MnONSs/GCE and YbNRs/CoONSs/GCE electrodes were diffusion-controlled. The YbNRs/MnONSs/GCE and YbNRs/CoONSs/GCE electrode sensors showed the ability to detect FLU, BIC and OHF. Stability studies at YbNRs/MnONSs/GCE and YbNRs/CoONSs/GCE showed good stability of the sensors in solutions of FLU, BIC and OHF. YbNRs/MnONSs/GCE and YbNRs/CoONSs/GCE displayed good selectivity in the detection of FLU, BIC and OHF. Spiked sample analysis showed good recoveries at both YbNRs/MnONSs/GCE and YbNRs/CoONSs/GCE.

5.4 Electrochemical properties of NRs decorated with NSs as electrocatalysts

5.4.1 Characterisation of the fabricated electrochemical sensors by cyclic voltammetry

CVs of the unmodified GCE (Bare GCE) and the modified GCE (YbNRs/MnONSs/GCE and YbNRs/CoONSs/GCE) were recorded in an electrolyte system consisting of $K_3Fe_3(CN)_6$, $K_4Fe_3(CN)_6$ (1 mM each) and KCl (0.1 M) as shown in **Fig. 5.16A** and **B**. These CVs were used to monitor the electron transfer efficiency in terms of oxidation-reduction peak potential difference (ΔE_p), as shown in **Table 5.4**, with the lowest (ΔE_p) value indicating better electron transfer. It was discovered from the extrapolated ΔE_p values that YbNRs/MnONSs (0.30 V) had a better electron transfer than YbNRs/CoONSs/GCE (0.49 V). This indicates that YbNRs/MnONSs/GCE surpassed YbNRs/CoONSs/GCE in terms of conductivity.

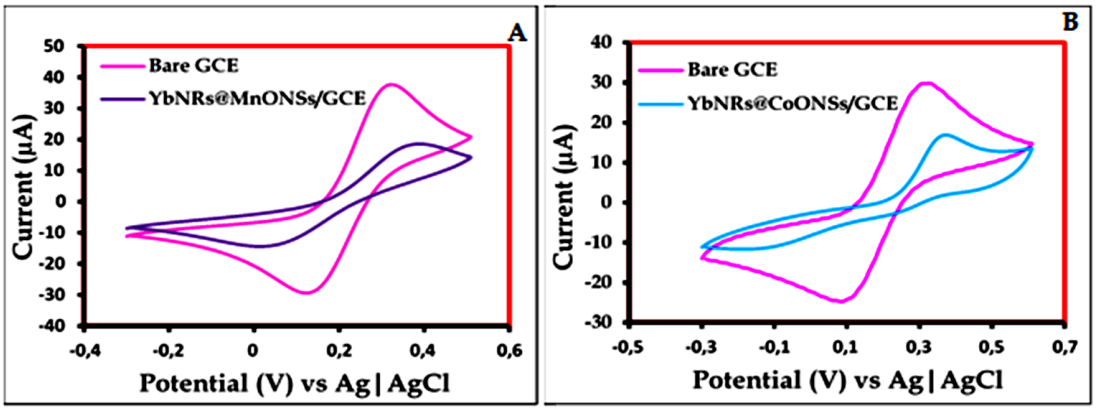

Fig. 5.16: Cyclic voltammograms of (A) bare GCE compared to YbNRs/MnONSs/GCE and (B) bare GCE versus YbNRs/CoONSs/GCE in ferricyanide solution.

One of the most important factors causing these differences in ΔE_p values is the surface roughness of GCE before and after modification. The lowest ΔEp value indicates better electron transfer; thus, Bare GCE (0.30 V) and YbNRs/MnONSs/GCE (0.30 V) had a better electron transfer YbNRs/CoONSs/GCE (0.49 V). The RandlesSevcik equation for reversible systems applied on $K_3Fe_3(CN)_6/K_4Fe_3(CN)_6$ redox system was used to determine the surface roughness factors of the modified electrodes, and the results were recorded in **Table 5.4**. Theoretical I_p was first calculated in order to determine the surface roughness factors of the modified electrodes. The obtained surface roughness factors were then used to calculate real

electrode areas. The corresponding real electrode areas were used to calculate surface coverage Γ for each modified GCE. The Γ values for modified electrodes less than 1 ×10^{-10} mol cm^{-2} imply a monolayer molecule film of the material on the electrode surface[1]. As reported in **Table 5.4**, the Γ values for the electrodes modified with NRs decorated with metal oxide NSs are greater than 1 ×10^{-10} mol cm^{-2} and increase in the following order: YbNRs/CoONSs/GCE < YbNRs/MnONSs/GCE. These Γ values suggest a multilayer of a nanocomposite (NC) molecule film on the electrode surface[2].

Table 5.4: Comparison of electrochemical sensing parameters of modified electrodes based on both anodic (I_{pa}, E_{pa}) and cathodic (E_{pc}) signatures in PBS (pH 5).

Electrode	I_{pa} (μA)	ΔE_p (V vs Ag|AgCl)	Real electrode area	Γ (mol cm^{-2})
Bare GCE	28.07	0.30	-	-
YbNRs/MnONSs/GCE	18.62	0.30	0.658	2.67 x 10^{-9}
YbNRs/CoONSs/GCE	16.94	0.49	0.594	3.23 x 10^{-9}

Response and behaviour comparison of **Table 5.1** and **Table 5.4:**

Among the modified electrodes, MnO/GCE the smallest ΔE_p which indicates better electron transfer between the electrode and the electrocatalyst material. The ΔE_p Values ranged from 0.22 V to 0.49 V which is not too much difference. The ascending order of ΔE_p values is YbNRs/CoONSs/GCE (0.49 V) < YbNRs/GCE (0.36 V) < YbNRs/MnONSs/GCE (0.30 V) < CoO/GCE (0.25 V) < MnO/GCE (0.22 V). the surface roughness factors of all the modified electrodes suggest a multilayer of a molecule film on the electrode surface. It can be concluded here that MnO/GCE showed better electrocatalytic ability than the rest of the electrode sensors.

5.4.2 Effects of scan rates at the surfaces of YbNRs/MnONSs/GCE and YbNRs/CoONSs/GCE

The mechanical and kinetic electrocatalytic redox processes of FLU, BIC and OHF were further investigated at the surfaces of YbNRs/MnONSs/GCE. This was performed by altering the scan rates from 10 to 100 mV/s at a fixed analyte concentration (1.00 mM) in PBS using CV. As can be observed in **Fig. 5.17A**, **B** and

C, the anodic peak currents increased with increased scan rates. This electrocatalytic behaviour based on reduction processes while varying scan rates established a linear relationship between the currents and scan rates of FLU, BIC and OHF at YbNRs/MnONSs/GCE. As apparent in **Fig. 5.17D**, **E** and **F**, the peak currents were linearly correlating with the square roots of scan rates. The correlative coefficients (R^2) for FLU, BIC, and OHF were 0.9831, 0.9967 and 0.9252, respectively. This relationship further connotes a diffusion-controlled process on the surfaces of modified electrodes. The mechanism of reduction of FLU, BIC and OHF is shown in **Fig. A1**.

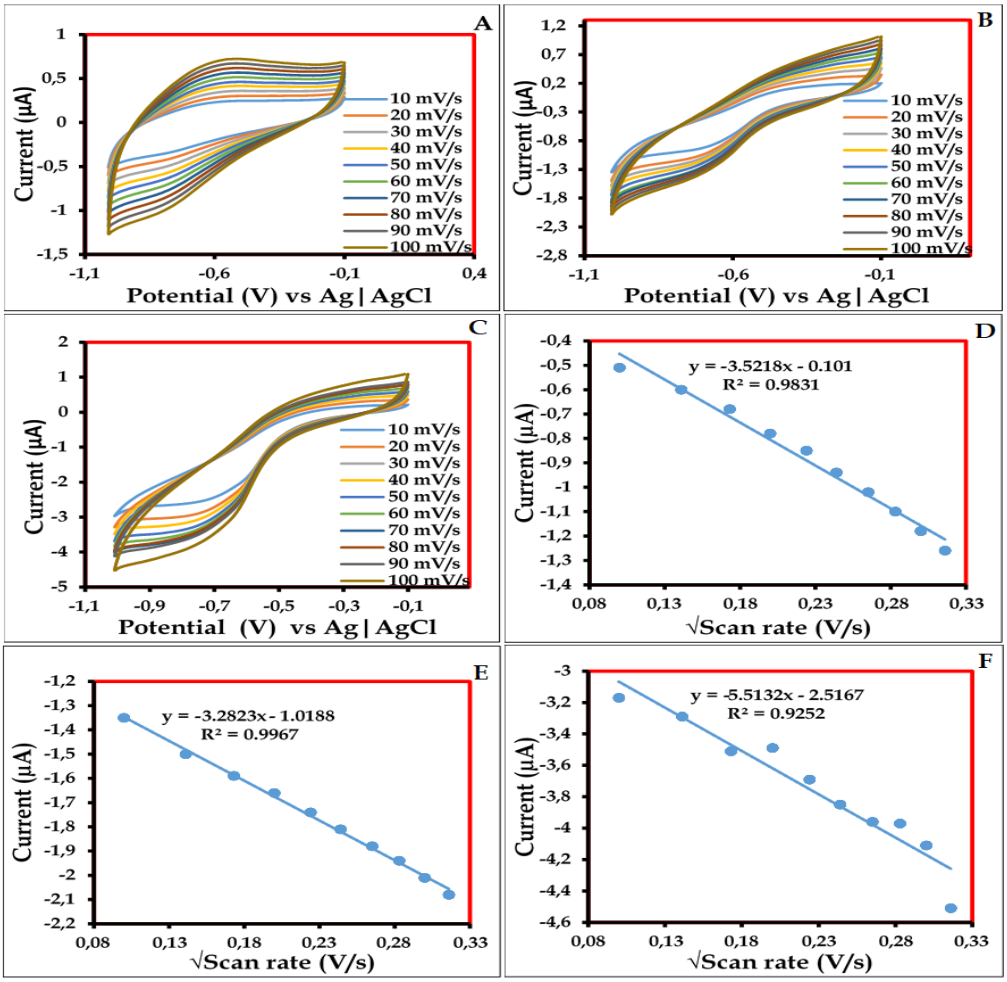

Fig. 5.17: CVs of scan rate variations of (A) FLU, (B) BIC and (C) OHF from 10-100 mV/s at YbNRs/MnONSs/GCE and the corresponding linear relationship plots (D, E and F, respectively).

The influence of scan rate on the electrochemical performance of YbNRs/CoONSs/GCE on FLU, BIC and OHF was also investigated using CV. The study was performed by varying the scan rates from 10 to 100 mV/s at a fixed analyte

concentration (1.00 mM) in PBS. As shown in **Fig. 5.18A**, **B** and **C**, the peak intensities were observed to increase with an increase in scan rate. For the detection of FLU (**Fig. 5.18A**), only the reduction process occurred upon altering scan rates at YbNRs/CoONSs/GCE. For BIC (**Fig. 5.18B**) and OHF (**Fig. 5.15C**), both reduction and oxidation processes occurred at the electrode surface at each scan rate at YbNRs/CoONSs/GCE. Only the mechanisms of reduction of FLU, BIC and OHF are depicted in **Fig. A1**.

The resultant peak currents were plotted against square roots of scan rates to determine linear relationships. As evident in **Fig. 5.18D**, **E** and **F**, the peak currents are linearly proportional to the square root of scan rates denoting diffusion-controlled processes at the surface of the electrode. The R^2 value for the reduction of FLU was 0.9883. For BIC and OHF, both reduction and oxidation processes occurred. The R^2 values for the reduction and oxidation of BIC were 0.9867 and 0.9814, while for OHF, they were 0.9035 and 0.9549, respectively.

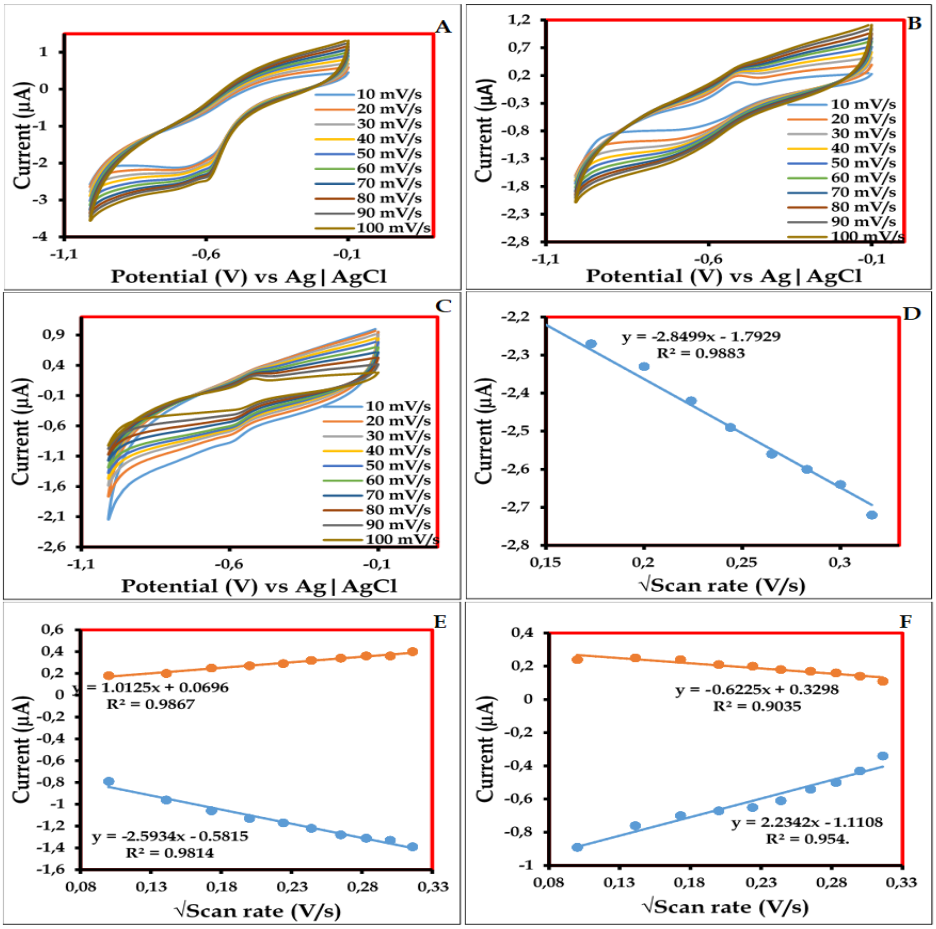

Fig. 5.18: CVs of scan rate variations of (A) FLU, (B) BIC and (C) OHF from 10-100 mV/s at YbNRs/CoONSs/GCE and their corresponding linear relationship plots (D, E and F, respectively).

5.4.3 Concentration studies

The electrochemical performance of YbNRs/MnONSs/GCE towards the detection and quantification of FLU, BIC and OHF was investigated using SWV at the linear range from 32.01 to 50.00 µM in PBS (pH 5) at a scan rate of 100 mV/s. **Fig. 5.19A**, **B** and **C** show the SWVs of FLU, BIC and OHF while varying concentration. As evident, the increase in the concentration of each analyte increased the reduction peak current. These results show that YbNRs/MnONSs/GCE was able to detect the analytes successfully **Fig. 5.19D**, **E,** and **F** represent the linear relationship plots obtained from the resultant peak currents and concentration of analyte. As can be seen in the Figure, the current is directly proportional to the concentration of the analyte, meaning that the current is dependent on concentration. The LODs and LOQs were calculated from these relationships. The LODs of FLU, BIC and OHF were 1.87 µM, 1.88 µM, and 1.92 µM, respectively. The LODs are relatively poor than what is reported in literature and this may be due to matrix effects and interferences, electrocatalysts used or sensitivity of instrument and its noise level. The LOQs of FLU, BIC and OHF were 6.25 µM, 6.26 µM, and 6.41 µM, respectively. These LODs and LOQs show that YbNRs/MnONSs/GCE is a promising electrocatalyst for detecting FLU, BIC and OHF because they are quite lower. The LODs are comparable to those in the literature, as in **Table 5.5**.

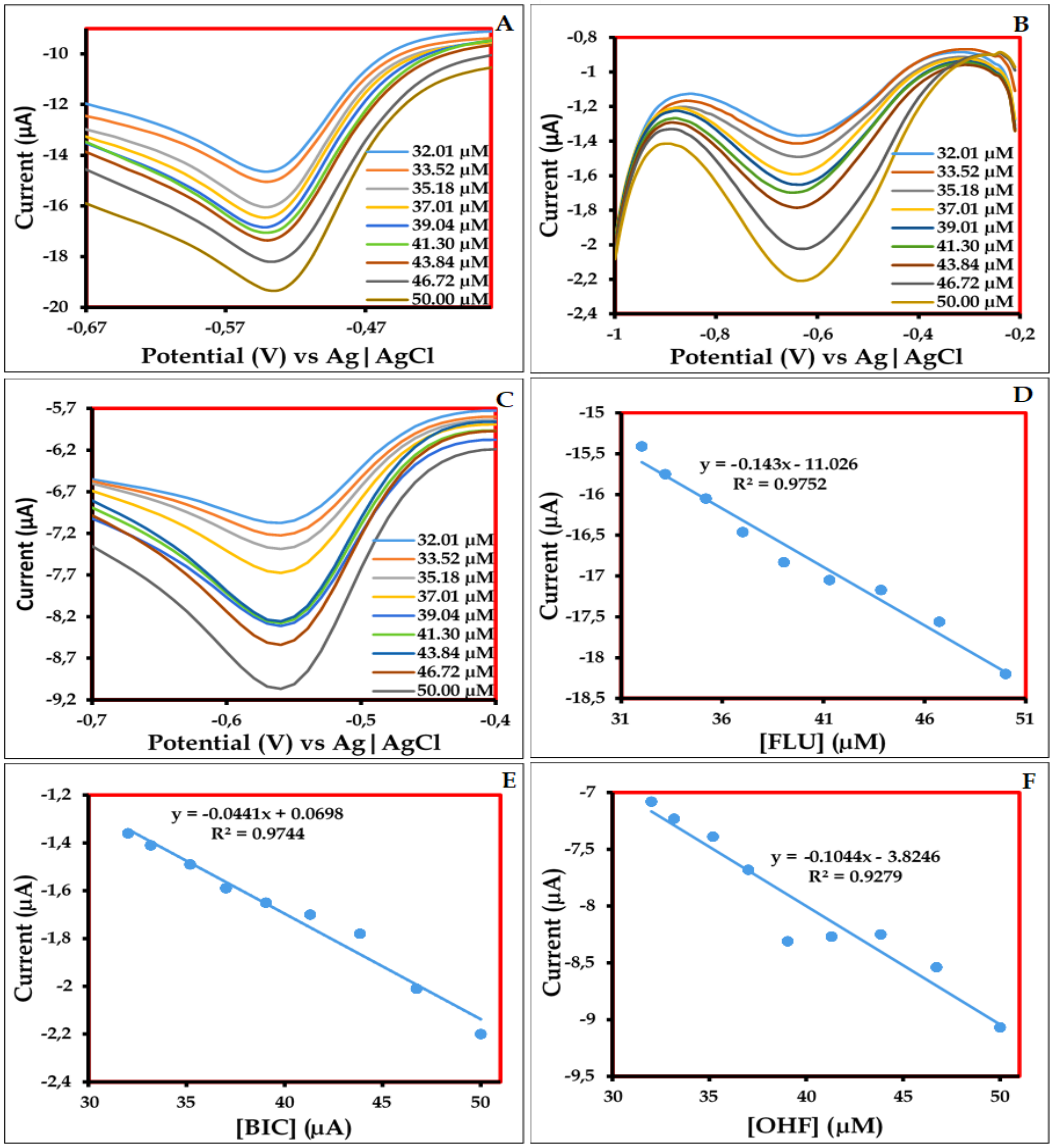

Fig. 5.19: SWVs on the variation of concentrations of (A) FLU, (B) BIC, (C) OHF from 32.01-50.00 µM and their corresponding linear relationship plots (D, E and F, respectively) at YbNRs/MnONSs/GCE.

Table 5.5. Comparison of detection limits for determining FLU, BIC and OHF at different electrodes.

Analyte	Modified electrode	Limit of detection (µM)	Linearity range (µM)	Sample type	Electroanalytical techniques	Ref.
FLU	$MWCNT_f$/GCE	0.03	0.1 - 1000	Drug and artificial urine	SWV	[3]
FLU	RGO/CuO/GCE	0.001	0.005 - 71.32	Human serum and human urine	CV	[4]
FLU	$NiFe_2O_4$/rGO–GCE	0.05	0.24 - 40.0	Urine and blood plasma	DPV	[5]
FLU	FC/MWCNTs/CPE	0.001	0.1 - 110	Human blood serum, plasma and urine	SWV	[6]
FLU	$BiVO_4$-rGO/CE-BN /GCE	0.011	0.04 - 102	Lake water	DPV	[7]
FLU	FCO/PPy/SPCE	0.086	0.4 - 376	Human serum and urine samples	DPV	[8]
FLU	Co_3O_4@NPC/GCE	0.012	0.1 - 590	Human urine	DPV	[9]
FLU	CFL-Ho^{3+}/NiO-NSs/GCE	0.0057	0.01 - 400.0	Flutanax tablets and urine	DPV	[10]
FLU	YbNRs/MnONSs/GCE	1.87	32.01 - 50.00	Tap water	SWV	This work
FLU	YbNRs/CoONSs/GCE	1.91	32.01 - 50.00	Tap water	SWV	This work

BIC	YbNRs/MnONSs/GCE	1.88	32.01 - 50.00	Tap water	SWV	This work
BIC	YbNRs/CoONSs/GCE	1.87	32.01 - 50.00	Tap water	SWV	This work
OHF	YbNRs/MnONSs/GCE	1.92	32.01 - 50.00	Tap water	SWV	This work
OHF	YbNRs/CoONSs/GCE	1.89	32.01 - 50.00	Tap water	SWV	This work

Similarly, the electrochemical performance of YbNRs/CoONSs/GCE towards the detection and quantification of FLU, BIC and OHF were also determined using SWV. The performance was studied by varying the concentration of the analyte from 32.01 to 50.00 µM in PBS at a scan rate of 100 mV/s. SWVs were recorded at each concentration and overlayed, as shown in **Fig. 5.20A**, **B** and **C**. As seen in the Figure, the reduction peak currents increased with increasing concentration. The resultant peak currents were then plotted against concentration to obtain linear relationship plots shown in **Fig. 5.20D**, **E** and **F**. From the linear relationship plots; the LODs were estimated to be 1.91 µM, 1.87 µM and 1.89 µM for FLU, BIC and OHF, respectively. LOQS were estimated to be 6.37 µM, 6.27 µM and 6.31 µM for FLU, BIC and OHF, respectively.

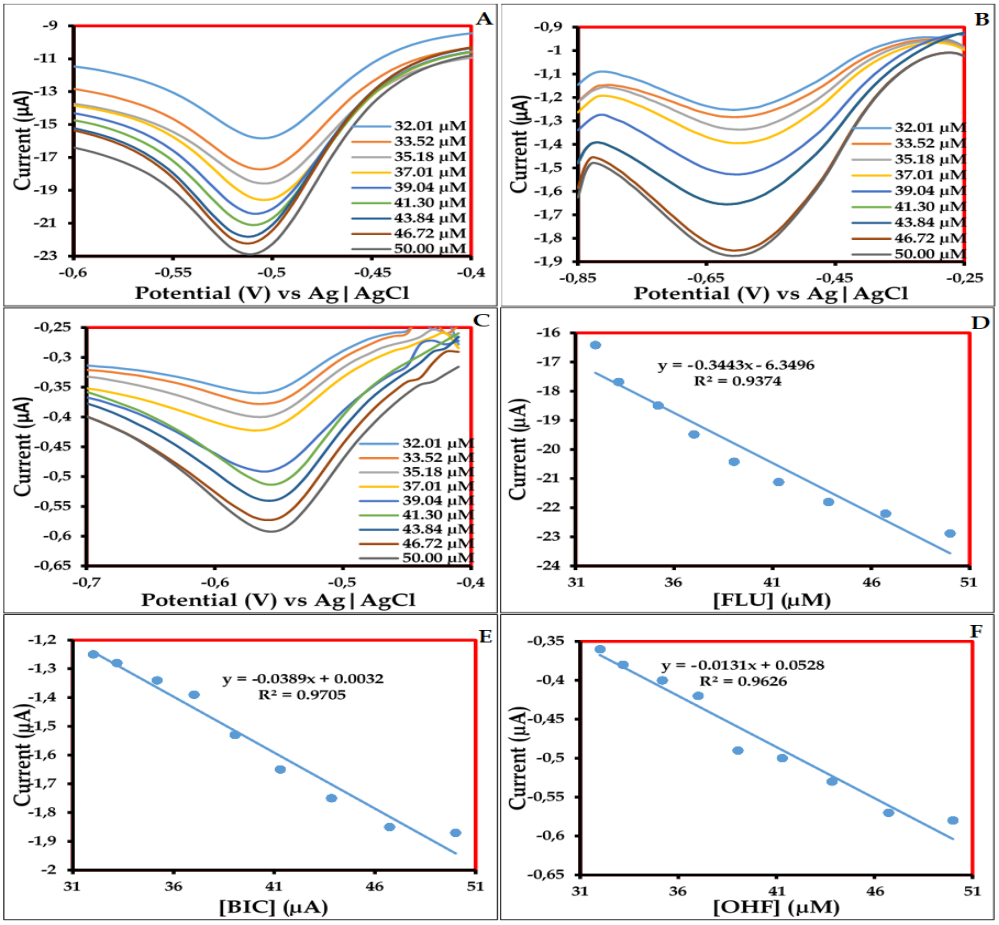

Fig. 5.20: SWVs of different concentrations of (A) FLU, (B) BIC, (C) OHF from 32.01-50.00 µM and their corresponding linear relationship plots (D, E and F, respectively) at YbNRs/CoONSs/GCE.

5.4.4 Stability studies

The stability of YbNRs/MnONSs/GCE and YbNRs/CoONSs/GCE for FLU, BIC and OHF was examined by running 9 scans at 100 mV/s in solutions (1 mM) of each analyte in PBS. The CVs shown in **Fig. 5.21A**, **B** and **C** are the stability scans at YbNRs/MnONSs/GCE for detecting FLU, BIC and OHF, respectively. The remaining CVs (**Fig. 5.21D**, **E** and **F**) are stability scans at YbNRs/CoONSs/GCE for detecting FLU, BIC and OHF, respectively. As can be observed in **Fig. 5.21**, the redox peak currents and potentials remained almost unchanged in all scans. Thus, both YbNRs/MnONSs/GCE and YbNRs/CoONSs/GCE show good stability towards detecting FLU, BIC and OHF.

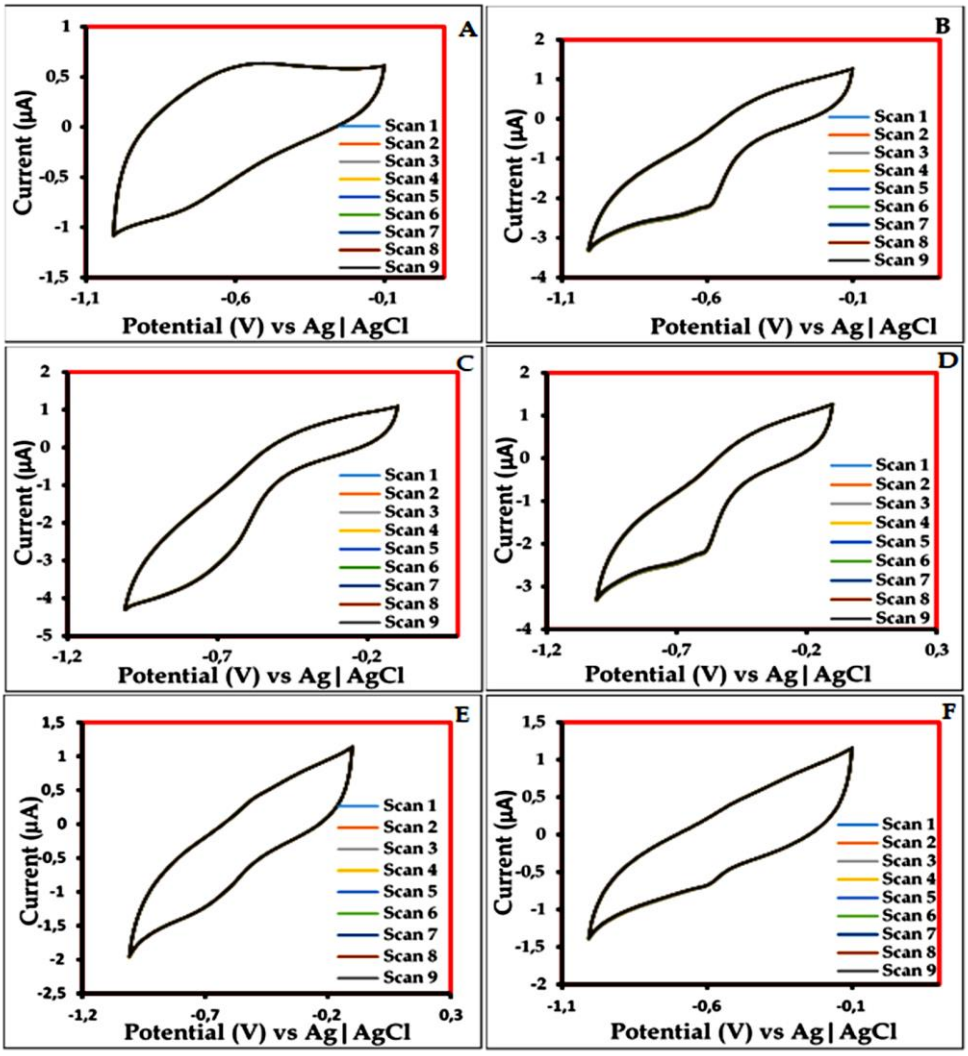

Fig. 5.21: Stability scans of (A) FLU, (B) BIC and (C) OHF at YbNRs/MnONSs/GCE and (D) FLU, (E) BIC and (F) OHF at YbNRs/MnONSs/GCE.

5.4.5 Interference studies

SWV was used to study the selectivity of YbNRs/MnONSs/GCE and YbNRs/CoONSs/GCE by detecting FLU, BIC and OHF in the presence of different interferents. Interfering species used in this study were Ca^{+}, Pb^{2+}, Mg^{2+}, K^{+} as well as Na^{+}. The study was performed using solutions (1 mM) of FLU, BIC and OHF with 1 mM of each interferent. From the results obtained, it was evident that all the interfering compounds do not interfere with the detection of both FLU, BIC and OHF, as shown in **Fig. 5.22A**, **B** and **C**; **Fig. 5.23A**, **B** and **C**. The bar graphs and error bars (**Fig. 5.22D**, **E** and **F**; **Fig. 5.23D**, **E** and **F)** also show minimal changes. Therefore, from the obtained results, the proposed electrode sensors were not susceptive to the interference by the compounds, indicating that YbNRs/MnONSs/GCE and YbNRs/CoONSs/GCE are suitable and selective towards the detection FLU, BIC and OHF. The reproducibility of YbNRs/MnONSs/GCE and YbNRs/CoONSs/GCE was also studied by using the electrode the electrodes repeatedly for 5 times for the three analytes. The RSD values were calculated from the repetitions and found to be 0.38, 2.21 and 1.17% at YbNRs/MnONSs/GCE and 0.14, 0.53 and 1.21% at YbNRs/CoONSs/GCE for FLU, BIC and OHF, respectively. These RSD values confirm has high reproducibility of YbNRs/MnONSs/GCE and YbNRs/CoONSs/GCE.

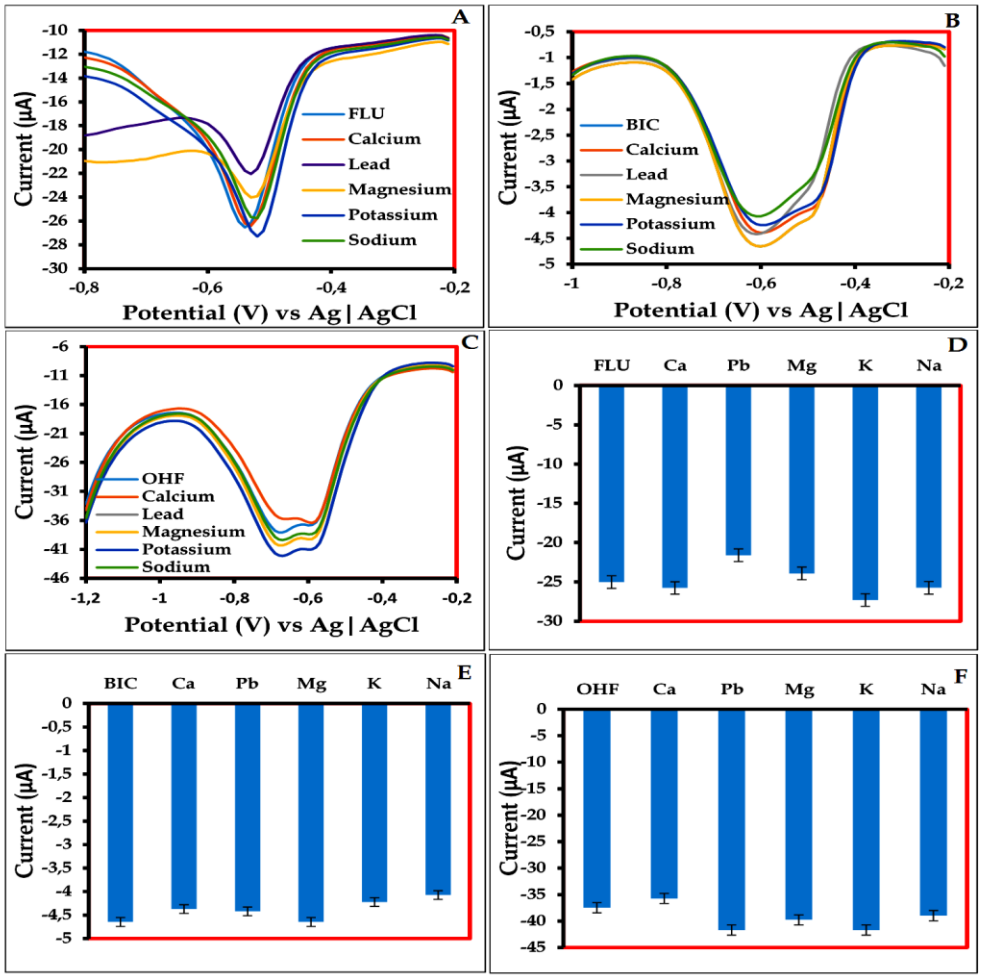

Fig. 5.22: SWVs of (A) FLU (B) BIC and (C) OHF in the presence of interfering species and the corresponding bar graphs (D), (E) and (F) respectively at YbNRs/MnONSs/GCE.

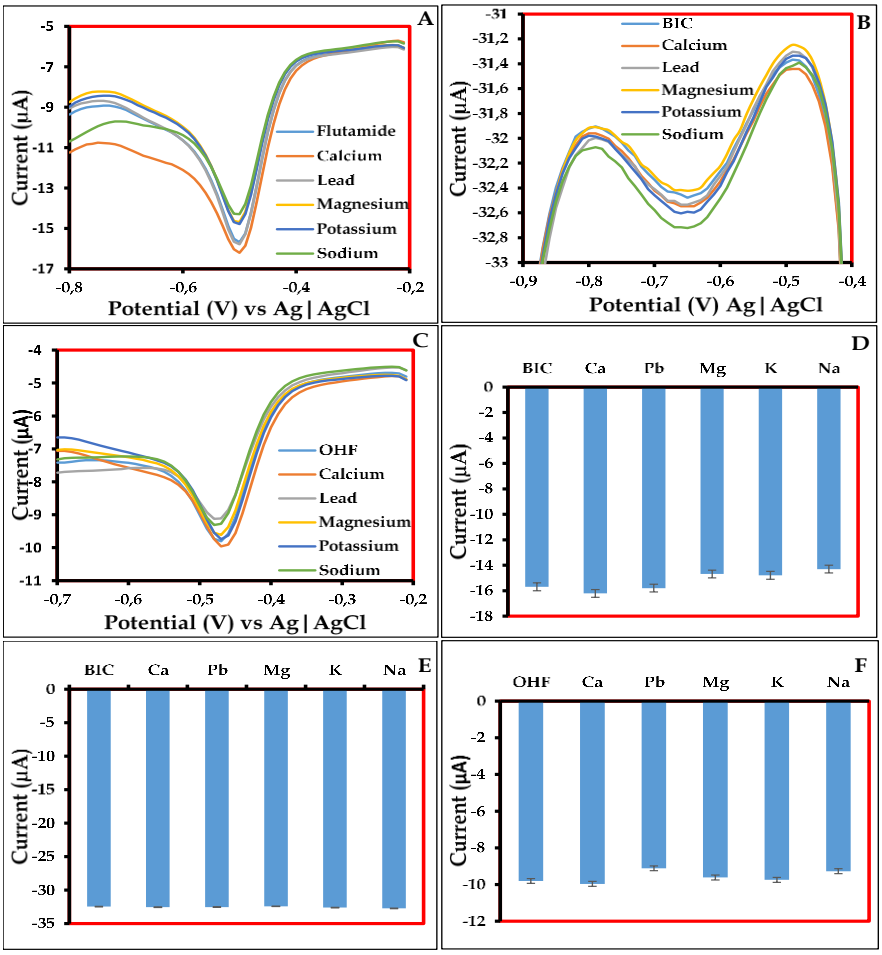

Fig. 5.23: SWVs of (A) FLU (B) BIC and (C) OHF in the presence of interfering species and the corresponding bar graphs (D), (E) and (F) respectively at YbNRs/CoONSs/GCE.

5.4.6 Spiked sample analysis

Tap water obtained from synthesis laboratories at the University of South Africa was adjusted to pH 5 using NaH_2PO_4, Na_2HPO_4 and HCl. Furthermore, stock solutions of FLU (1 mM), BIC (1 mM) and OHF (1 mM) were prepared. The phosphate-treated tap water PBS solution was taken into a voltammetric cell, and its SWV was recorded. **Fig. 5.24** shows the spiked sample analysis of the FLU, BIC and OHF at a linear range of 1.40-9.82 µM, at pH 5 and a scan rate of 100 mV/s at YbNRs/MnONSs/GCE. **Fig. 5.21A, B** and **C** show the SWVs of the spiked sample analysis of FLU and BIC, respectively. As seen in the Figures, the current increases with the concentration of each analyte. This shows that the electrode sensor could detect FLU, BIC and OHF even in Spiked samples. **Fig. 5.24D**, **E** and **F** shows the corresponding linear relationship plots and depicts a directly proportional relationship between current and

analyte concentration. This means that the current is dependent on the concentration. The obtained % recoveries ranged from 97.85 – 99.28 %, and the RSD values ranged from 1.82 – 3.40%, as provided in **Table 5.6**. The recoveries show good accuracy of YbNRs/MnONSs/GCE in the detection of the analytes.

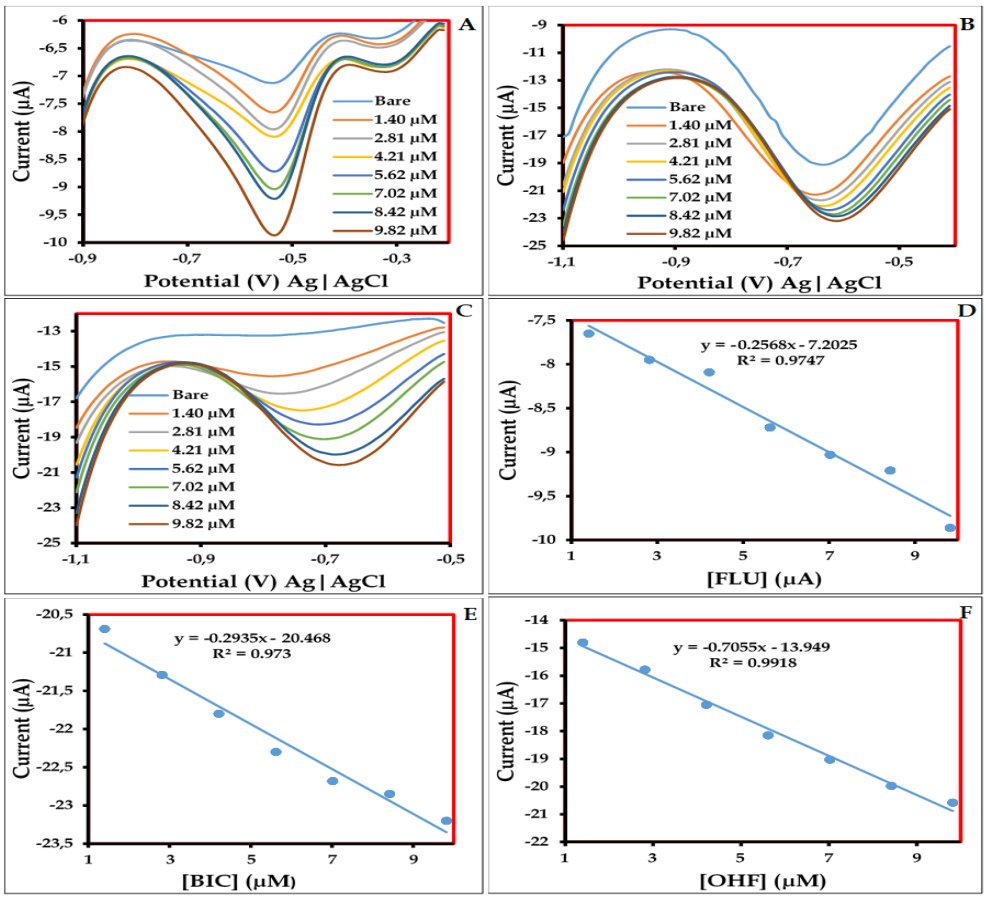

Fig. 5.24: SWVs of Spiked sample analysis of (A) FLU, (B) BIC, (C) OHF and their corresponding linear relationship plots D, E and F at YbNRs/MnONSs/GCE.

Spiked samples were also analysed at YbNRs/CoONSs/GCE for FLU, BIC and OHF. **Fig. 5.25** shows the spiked sample analysis of the analytes of interest at a linear range of 1.40-9.82 µM, at pH 5 and a scan rate of 100 mV/s at YbNRs/CoONSs/GCE. **Fig. 5.25A**, **B** and **C** show the SWVs of the spiked sample analysis of FLU, BIC and OHF, respectively. From the Figures, it can be seen that the peak current increased with an increase in the concentration of each analyte. The obtained % recoveries ranged from 96.42 - 99.28%, and the RSD values ranged from 1.98 - 3.72%. The recoveries show good accuracy of YbNRs/CoONSs/GCE in the detection of the analytes.

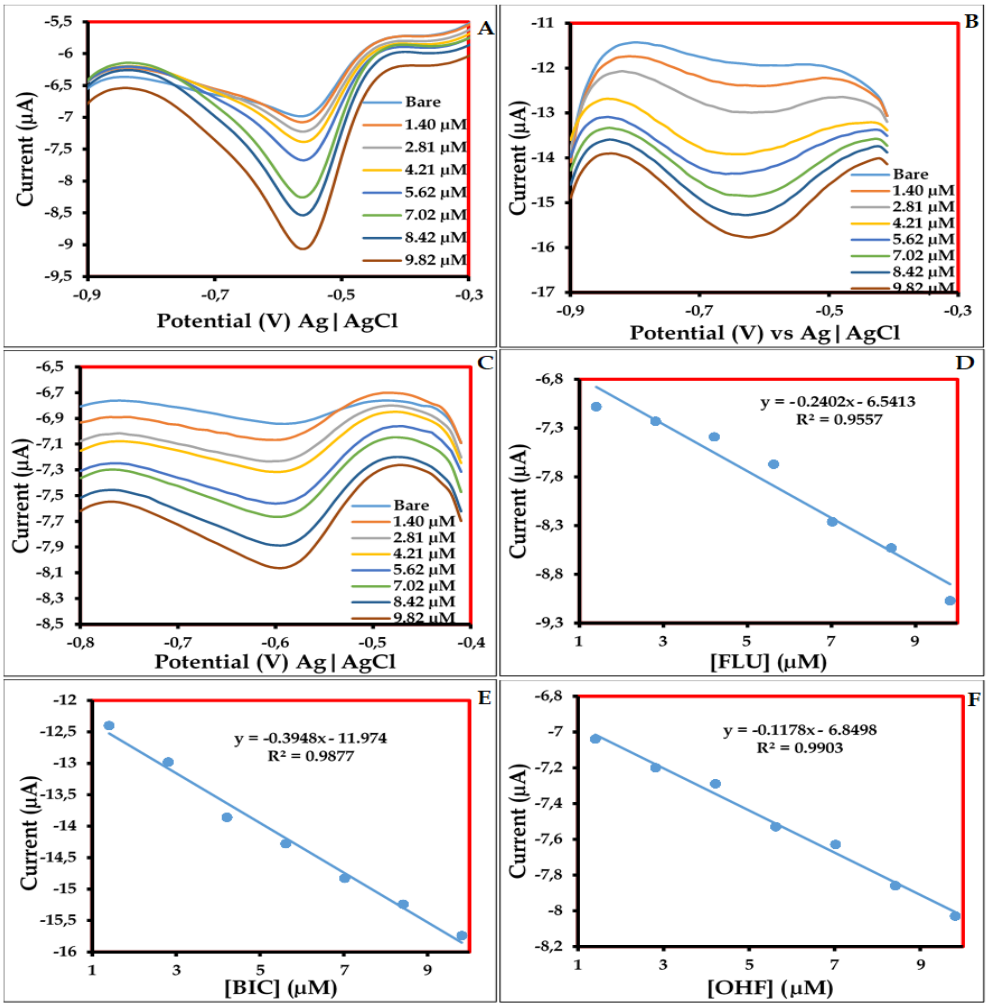

Fig. 5.25: SWVs of Spiked sample analysis of (A) FLU, (B) BIC, (C) OHF and their corresponding linear relationship plots D, E and F at YbNRs/CoONSs/GCE.

Table 5.6. Comparison of % recoveries of FLU, BIC and OHF at YbNRs/MnONSs/GCE and YbNRs/CoONSs/GCE.

YbNRs/MnONSs/GCE						YbNRs/CoONSs/GCE				
Analyte	Amount added (µL)	Expected conc. (µM)	Found conc. (µM)	Recoveries (%)	RSD (%)	Amount added (µL)	Expected conc. (µM)	Found conc. (µM)	Recoveries (%)	RSD (%)
FLU	10	1.40	1.38 ± 0.05	98.57	3.40	10	1.40	1.39 ± 0.04	99.28	2.98
BIC	10	1.40	1.37 ± 0.03	97.85	2.28	10	1.40	1.35 ± 0.05	96.42	3.72
OHF	10	1.40	1.39 ± 0.03	99.28	1.82	10	1.40	1.38 ± 0.03	98.57	1.98

Comparison of **Table 5.3** and **Table 5.6**

Both **Table 5.3** and **Table 5.6** have good % recoveries which ranged from 95.1 to 100% for MnO/GCE and CoO/GCE, 90 to 98.28% for YbNRs/GCE, 97.85 to 99.28% for YbNRs/MnONSs/GCE and 96.42 to 98.57% for YbNRs/CoONSs/GCE. However, the nanocomposites in **Table 5.6** are better than those of the metal oxides nanostructures and lanthanide nanorods in **Table 5.3** as the lowest recovery value was 96.42%. The RSD% values in **Table 5.3** are higher than those in **Table 5.6** and range from 1.82 to 8.57% while those in **Table 5.6** range from 1.82 to 3.72%. Therefore, it can be concluded that the nanocomposites performed better than the nanostructures and nanorod

Conclusion

Two novel and simple sensors for detecting and quantifying FLU and its derivatives, BIC and OHF, were successfully developed. The two sensors (YbNRs/MnONSs/GCE and YbNRs/CoONSs/GCE) showed efficient electrocatalytic activities through CV and SWV methods. Both YbNRs/MnONSs/GCE and YbNRs/CoONSs/GCE showed excellent practical feasibility through spiked sample analysis experiment which resulted in good recovery ranging from 1.82 to 3.72%. Therefore, based on the relevant observations from this work, we can conclude that the YbNRs/MnONSs/GCE and YbNRs/CoONSs/GCE electrochemical sensors are reliable.

References

1. Edward Sekhosana, K., Nkhahle, R. & Nyokong, T. Analytical Detection and Electrocatalysis of Paracetamol in Aqueous Media Using Rare-Earth Double-Decker Phthalocyaninato Chelates as Electrochemically Active Materials. *ChemistrySelect* **5**, 9857–9865 (2020).

2. Sekhosana, K. E., Shumba, M. & Nyokong, T. Electrochemical Detection of 4-Chlorophenol Using Glassy Carbon Electrodes Modified with Thulium Double-Decker Phthalocyanine Salts. *ChemistrySelect* **4**, 8434–8443 (2019).

3. Farias, J.S., Zanin, H., Caldas, A.S., Dos Santos, C.C., Damos, F.S. and de Cássia Silva Luz, R. Functionalized Multiwalled Carbon Nanotube Electrochemical Sensor for Determination of Anticancer Drug Flutamide. *J. Electron. Mater.* **46**, 5619–5628 (2017).

4. Sakthinathan, S., Kokulnathan, T., Chen, S.M., Karthik, R., Tamizhdurai, P., Chiu, T.W. and Shanthi, K. Simple Sonochemical Synthesis of Cupric Oxide Sphere Decorated Reduced Graphene Oxide Composite for the Electrochemical Detection of Flutamide Drug in Biological Samples. *J. Electrochem. Soc***. 166**, 68–75 (2019).

5. Ensafi, A. A., Talkhooncheh, B. M., Zandi-Atashbar, N. & Rezaei, B. Electrochemical Sensing of Flutamide Contained in Plasma and Urine Matrices Using $NiFe_2O_4$/rGO Nanocomposite, as an Efficient and Selective Electrocatalyst. *Electroanalysis* **32**, 1717–1724 (2020).

6. Brahman, P. K., Suresh, L., Reddy, K. R. & Bondili, J. S. An electrochemical sensing platform for trace recognition and detection of an anti-prostate cancer drug flutamide in biological samples. *RSC Adv.* **7**, 37898–37907 (2017).

7. Bhuvaneswari, C., Palpandi, K., Amritha, B., Paunkumar, P., Priya, R.L., Raman, N. and Babu, S.G. Conniving for the first time of BiVO4 - rGO/CE-BN and its Potential as enhanced electrochemical sensing of non-steroidal anti-androgen drug. *Microchem. J.* **184**, 108174 (2022).

8. Manjula, N., Vinothkumar, V. & Chen, S. Colloids and Surfaces A : Physicochemical and Engineering Aspects Synthesis and characterization of

iron-cobalt oxide / polypyrrole nanocomposite : An electrochemical sensing platform of anti-prostate cancer drug flutamide in human urine and serum samples. *Colloids Surfaces A Physicochem. Eng. Asp.* **628**, 127367 (2021).

9. Devi, R. K., Muthusankar, G., Chen, S. M. & Gopalakrishnan, G. In situ formation of Co3O4 nanoparticles embedded N-doped porous carbon nanocomposite: a robust material for electrocatalytic detection of anticancer drug flutamide and supercapacitor application. *Microchim. Acta* **188**, 196 (2021).

10. Fathi, Z., Jahani, S. & Foroughi, M. M. Electrode material fabricated by doping holmium in nickel oxide and its application in electrochemical sensor for flutamide determination as a prostate cancer drug. *Monatshefte fur Chemie* **152**, 757–766 (2021).

CHAPTER 6

CONCLUSIONS AND FUTURE PERSPECTIVES

The use of AAs is growing exponentially with the diagnosis of prostate cancer in men worldwide. This leads to the continuous excretion of these compounds into WWTPs to surface water. This study aimed to develop simple, electrocatalytically active, highly stable and reusable ytterbium-based NRs decorated with MnONSs and CoONSs to detect and quantify FLU, BIC and OHF in water samples. To achieve this aim, the following objectives were successfully implemented: synthesis of new YbNRs, synthesis MnONSs and CoONSs, coating YbNRs with MnONSs and CoONSs to form efficient electrocatalysts, extensive characterisation of the synthesised nanomaterials as electrocatalysts, applying the synthesised electrocatalysts as sensors in aqueous media to determine the amounts of FLU, BIC and OHF.

The following conclusions were drawn from this study:

- SEM, FTIR, UV-Vis, TEM, EDX, and XRD proved the successful synthesis of MnONSs, CoONSs, and YBNRs, as well as the coating of YbNRs with MONSs into YbNRs/MnONSs and YbNRs/CoONSs. XRD revealed the symmetries of the as-prepared materials as tetragonal, cubic, cubic, tetragonal, and cubic for MnONSs, CoONSs, YBNRs, YbNRs/MnONSs and YbNRs/CoONSs, respectively.
- MnONSs, CoONSs, YBNRs, YbNRs/MnONSs and YbNRs/CoONSs exhibited enhanced electroactivity towards the detection of FLU, BIC and OHF. Through their enhanced electroactivity, the resultant electrochemical sensors also showed good selectivity, stability, reliability, repeatability and reproducibility.
- The fabricated YbNRs showed good reusability, stability and selectivity through stability and interference studies.
- YbNRs without coating show low efficiency compared to other electrocatalysts used in detecting FLU, BIC and OHF; however, the coating enhanced the efficiency of YbNRs in electrocatalysis.

- The LODs of the sensors were comparable to the literature and ranged from 13 - 18.8 µM (MnO/GCE), 18.5 - 18.8 µM (CoO/GCE), 18.5 - 19.3 µM (YbNRs/GCE), 1.87 - 1.91 µM (YbNRs/MnONSs), and 1.87 - 1.91 µM (YbNRs/CoONSs). Thus, coating YBNRs with MONSs significantly influences the LOD of the sensors. Coating YbNRs with MONSs also enhanced the peak currents. When coated with CoONSs, YBNRs showed good electrocatalysis as both oxidation and reduction processes were observed during scan rate analysis which was not observed with YbNRs alone; thus, the coating enhanced the electrocatalytic ability of YbNRs.
- The application of MnONSs/GCE, CoONSs/GCE, YBNRs/GCE, YbNRs/MnONSs/GCE and YbNRs/CoONSs/GCE in Spiked samples showed good recoveries in the range of 90.94 - 100%, which shows that these electrochemical sensors can be used in real-time sample analysis.
- Two novel, simple, electrocatalytically active, highly stable and reusable electrochemical sensors based on the decoration of YbNRs with MnONSs and CoONSs for the detection and quantification of FLU, BIC and OHF in water samples were successfully fabricated.

Thus, the aim of the study has been successfully achieved. However, the following can solve the limitations of the sensors to improve their performances further:

- More electrocatalyst materials to decorate YbNRs should be explored to obtain better LODs and LOQs.
- Different electrolyte solutions should be explored to determine which works better for the fabricated electrochemical sensors.
- A better linear range should be used for the detection of analytes.
- The fabricated sensors can be used to detect other pharmaceutical compounds.
- WWTPs samples can be used as Spiked samples.
- Rigorous selectivity, stability, reliability, repeatability and reproducibility testing.
- In-depth interference, broader range and selectivity analysis.
- Spiked sample analysis.
- Sensor validation and rigorous testing.

- Electrocatalyst materials can be employed in energy storage applications, including water splitting, solar cells, oxygen evolution reactions, and hydrogen evolution reactions.

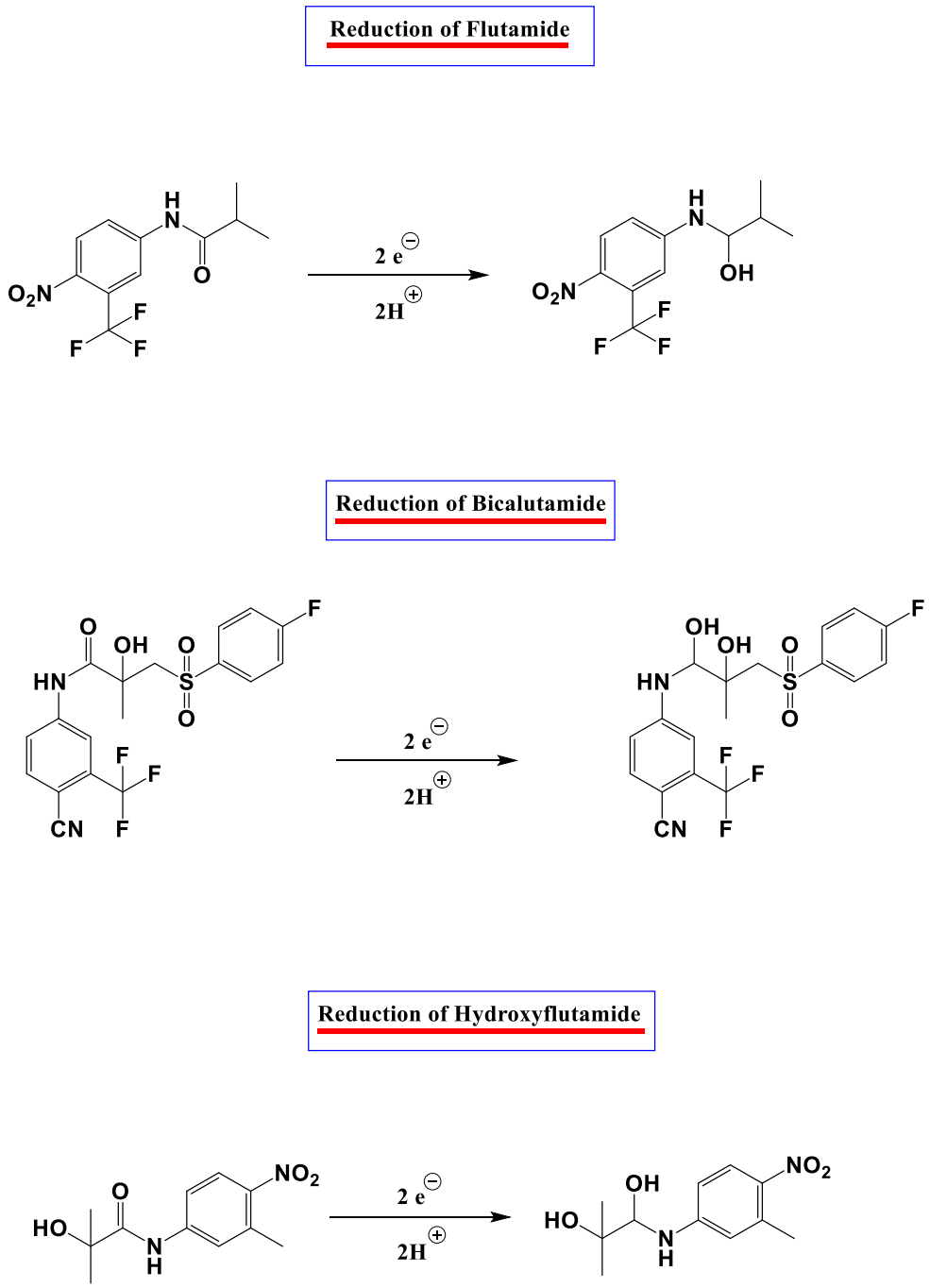

Fig. A1: Proposed mechanism of the electro-reduction of FLU, BIC and OHF.